Pergamon

Prog Solid St Chem. Vol. 28, pp 201-281, 2000

Printed in Great Britain
0079-6780/00/$ - see front matter

PII: S0079-6786(00)00006-6

The $M_{N+1}AX_N$ Phases: A New Class of Solids;
Thermodynamically Stable Nanolaminates

By
Michel W. Barsoum
Department of Materials Engineering
Drexel University, Philadelphia, PA 19104

1. INTRODUCTION

Thirty years ago, Nowotny published a review article in this journal[1] summarizing some of the work that he and his coworkers had carried out during the sixties on the syntheses of a large number of carbides and nitrides[1-18]. It was an impressive accomplishment; during that decade, his group discovered over 100 new carbides and nitrides. Amongst them were more than thirty, so-called H- or Hägg phases, that are of specific interest to this work. These H-phases have a M_2AX chemistry, where M is an early transition metal, A is an A-group element (mostly IIIA and IVA) and X is either C and/or N (Table I). They are layered and hexagonal with M_2X layers interleaved with layers of pure A (Fig. 1a). In 1967 they discovered Ti_3SiC_2[11] and Ti_3GeC_2[12], both of which are structurally related to the H-phases in that M_3X_2 layers separate the A-layers (Fig. 1b). It was not until the early 90's, however, that Pietzka and Schuster, the latter a coworker of Nowotny, added Ti_3AlC_2 to the list[19,20]

The history of the H-phases, henceforth referred to as the 211 phases, is quite short. Astonishingly enough from the time of their discovery until our first report, and apart from a series of Russian papers in the mid-seventies[21-24] in which it was claimed that 90-92% dense compacts of Ti_2AlC and Ti_2AlN were synthesized, they were totally ignored. The Russian results have to be interpreted with care, however, since their reported microhardness values of $\approx$ 21 to 24 GPa, are difficult to reconcile with the actual values that range from 3-4 GPa. Some magnetic permeability measurements on Ti_2AlC and Cr_2AlC had also been reported[10]. To date, the situation remains for the most part unchanged for a majority of the 211 phases; the only results available are the ones we reported.

The history of Ti_3SiC_2 is slightly more involved. The first hint that Ti_3SiC_2 was atypical came as early as 1972, when Nickl et al.[25], working on chemically vapor deposited, CVD, single

crystals, showed that Ti_3SiC_2 was anomalously soft for a carbide. The hardness was also quite anisotropic, with the hardness normal to the basal planes roughly 3 times that parallel to them. When the authors used a solid state reaction route, the resulting material was no longer "soft". In 1987, Goto and Hirai[26], confirmed the results of Nickl et al. Since then a number of other studies on CVD films or single crystals made by CVD have appeared[27-30].

The fabrication of single phase, bulk dense samples of Ti_3SiC_2 proved to be much more elusive, however. Attempts to synthesize it in bulk form always resulted in samples containing, in most cases, TiC, and sometimes SiC, as an ancillary unwanted phase[31-42]. Consequently, before our breakthrough in synthesis[43] little was known about Ti_3SiC_2, and much of what was known has since been shown to be incorrect. For example, despite a sentence buried in one of Nowotny's papers claiming Ti_3SiC_2 does not melt but dissociates at 1700 °C into TiC and a liquid[17], the erroneous information that it has a melting point of over 3000 °C[41] is still being disseminated. Furthermore, and prior to our work, many of the Ti_3SiC_2 samples fabricated in bulk form were unstable above ≈ 1450 °C[32-34,35]. We have shown that, if pure, Ti_3SiC_2 is thermally stable to at least 1700 °C in inert atmospheres[43,44]; a result that has been confirmed recently by others[45,46]. Another important misconception that tempered the enthusiasm for Ti_3SiC_2 was again, the erroneous belief that its oxidation resistance was poor above 1200 °C[32,39,40].

Despite the aforementioned pitfalls, Pampuch, Lis and co-workers[32-38], came closest to fabricating pure bulk samples; their best samples were ≈ 80-90 vol. % pure (balance TiC). Using these samples they were the first to show that Ti_3SiC_2 was elastically quite stiff, with Young's and shear moduli of 326 GPa and 135, respectively[34] and yet was easily machinable. They also confirmed its relative softness (Vickers hardness of 6 GPa) and noted that the high stiffness-to-hardness ratio was more in line with ductile metals than ceramics, and labeled it a "ductile" ceramic. Apart from these properties and a report that the thermal expansion of Ti_3SiC_2[42] was 9.2 x 10^{-6} K^{-1}, no other properties were known.

For the sake of completion it should be noted that reference to Ti_3SiC_2 in the literature occurs in another context. This phase is sometimes found at the interface when Ti and SiC are in contact[42,47-59] at higher temperatures. The latter are encountered when Ti is used as braze material to bond SiC to SiC, in SiC Ti-reinforced metal matrix composites, or as potential electrodes in SiC-based semiconductor devices[59].

Quite recently, we identified, Ti_4AlN_3, henceforth referred to as 413, to be a related compound[60-63]. At which point it became apparent that we were dealing with a family of ternary layered compounds with the general formula: $M_{N+1}AX_N$, where N is 1, 2 or 3, M is an early transition metal, A is an A-group (mostly IIIA and IVA) element, and X is either C or N. During the past four years, and funded primarily by the National Science Foundation, we have shown that these phases represent a new class of solids that can be best described as *thermodynamically stable nanolaminates*. It has long been predicted, and our results fully confirm, that nanoscale solids, especially laminates, should exhibit unusual and exceptional mechanical properties. Full-scale exploitation of this idea, however, had been hindered by two fundamental problems. The first has to do with the cost of manufacturing bulk samples: Making large parts by molecular beam epitaxy, for instance, is not commercially viable. The second problem is more

fundamental: Even if fabricated, such fine-scale assemblages would not be thermodynamically stable and as such would be of limited use at elevated temperatures.

Another powerful idea to emerge in the last decade in the materials community is that of biomimetics, wherein nature's splendid designs that had evolved over millions of years, would be imitated. For example, abalone shell, mainly comprised of a brittle calcium carbonate, is quite tough. This toughness arises from a submicron polymer film that lies between the calcium carbonate layers. The microstructural similarities between the fractured surfaces of abalone shell and those of the $M_{N+1}AX_N$ phases are remarkable. The layering in abalone, however, is on a much coarser scale. Another crucial distinction is that the properties of abalone are optimized for room temperature use. Heating an abalone shell to a couple of hundred degrees destroys the polymer, and concomitant toughness. Wood is another example, where again there is a marked resemblance to the $M_{N+1}AX_N$ phases.

Since 1996, when our first paper on Ti_3SiC_2[43] was published, we have embarked on an ambitious program whose goal is to synthesis and characterize all the $M_{N+1}AX_N$[43,44,60-114] phases. To date, we have fabricated and characterized $\approx$ 15 of the roughly 50 $M_{N+1}AX_N$ phases known to exist (Table I). Thermally, elastically, chemically and electrically, they share many of the advantageous attributes of their respective *stoichiometric* binary metal carbides or nitrides: they are elastically stiff, electrically and thermally conductive. Mechanically, however, they cannot be more different: they are readily machinable, relatively soft, resistant to thermal shock and unusually damage tolerant. They are the only polycrystalline solids that deform by a combination of kink and shear band formation, together with the delaminations of individual grains. Dislocations multiply and are mobile at room temperature, glide exclusively on the basal planes, and are overwhelmingly arranged either in arrays or kink boundaries. They combine ease of machinability with very decent mechanical properties, especially at temperatures > 1000 °C. Furthermore, Ti_3SiC_2 and Ti_4AlN_2 couple thermal isotropy with mechanical anisotropy.

As discussed in this paper, this unusual combination of properties is traceable to their layered structure, the mostly metallic - with covalent and ionic contributions - nature of the MX bonds that are exceptionally strong, together with M-A bonds that are relatively weak, especially in shear. The best-characterized ternary to date is Ti_3SiC_2. We currently know its tensile, compressive and flexural strengths and their temperature dependencies. Its creep, hardness, oxidation resistance, fatigue, fracture toughness and R-curve behavior, tribological properties and surface characteristics have been measured. Additionally its electrical conductivity, Hall and Seebeck coefficients, heat capacity, both at low and high temperatures, elastic properties and their temperature dependencies, thermal expansion and thermal conductivity have been quantified.

In brief, and despite the relatively short time these compounds have been identified as having unusual properties, we have come a long way in understanding their physical, mechanical and chemical properties. The purpose of this paper is to summarize this understanding. This paper is divided into nine parts. The following section reviews the structure and bonding commonalties and trends between these phases. Section 3, deals with some recent ab initio calculations that, for the most part, capture the essence of the bonding in these solids. Section 4 summarizes our knowledge of the thermal properties, including Rietveld analysis of high temperature neutron diffraction results, thermal expansion and conductivity and thermal stability. The fifth section deals with the electrical transport, including conductivity, Hall and Seebeck coefficient

measurements. The elastic properties are reviewed in section six. The seventh, and longest section, deals with their mechanical response. The last major section deals with chemical reactivity and oxidation resistance. The final sections deal with outstanding issues and some of the potential applications for these solids.

2. STRUCTURE AND BONDING

The $M_{N+1}AX_N$ phases are layered hexagonal (space group D^4_{6h}-$P6_3/mmc$) with two formula units per unit cell. Figures 1a, b and c compare the unit cells of the 211, 312 and 413 phases, respectively. In each case near close-packed layers of M layers are interleaved with layers of pure group A-element, with the X-atoms filling the octahedral sites between the former. The A-group elements are located at the center of trigonal prisms that are larger than the octahedral sites and thus better able to accommodate the larger A-atoms. The M_6X octahedra are edge sharing and are identical to those found in the rock salt structure of the corresponding binary carbides (see Fig. 4). The main difference between the structures shown in Fig. 1 is in the number of M layers separating the A-layers: in the 211's there are two; in the 312's, three, and in the 413's four. As discussed in more detail later, this layering is crucial and fundamental to understanding the properties in general, and the mechanical properties in particular.

Table 1 lists all the $M_{N+1}AX_N$ phases known to date, together with their lattice parameters and theoretical densities. The A-group elements are mostly IIIA and IVA. All but four compounds are 211's; by far the most prevalent structure. Al is the most versatile A-group element with 8 compounds, including nitrides, 312's and the sole 413 phase. With nine Ga forms the most 211 phases. As noted above, the vast majority of these phases were discovered in the sixties by Nowotny and co-workers[1-18]. Interestingly enough, a table similar to the one shown in Table I, appeared 30 years ago in this publication[1].

There are only three 312 phases known to date: Ti_3SiC_2[11], Ti_3GeC_2[12] and Ti_3AlC_2[19,20]. The only Si-containing ternary is Ti_3SiC_2, and there are no reports of N-containing 312 phases. The only 413 phase known to exist is Ti_4AlN_3[60–63]. This phase was initially believed to be $Ti_3Al_2N_2$[115,116]. Later, it was suggested, mostly on chemical analysis, that it was isostructural with Ti_3SiC_2[117]. Recently, however, we have unequivocally shown by high resolution transmission electron microscopy, HRTEM[60], Rietveld analysis of neutron diffraction, ND, data[63], and by careful mapping of the ternary phase diagram[61] that this phase possesses the unit cell shown in Fig. 1c. The corresponding HRTEM image is shown in Fig. 2, wherein the layered nature of the compound is clearly visible[60]. It is worth noting that this phase is N deficient since its exact stoichiometry is $Ti_4AlN_{2.9}$[60]. Similarly, we found that only a Ti:Al:C ratio of 3:1.1:1.8 led to single phase sample, i.e. $Ti_3Al_{1.1}C_{1.8}$[96]. Since this composition was not otherwise confirmed it should be considered preliminary at this stage.

The structure of Ti_2AlN as determined by HRTEM[89] agrees with that previously determined from Rietveld analysis of diffraction data[1,4]. Conversely, the crystal structures of thinned Ti_3SiC_2, $Ti_4AlN_{2.9}$ and Ti_3AlC_2 samples do not[60,89]. For example, the HRTEM image

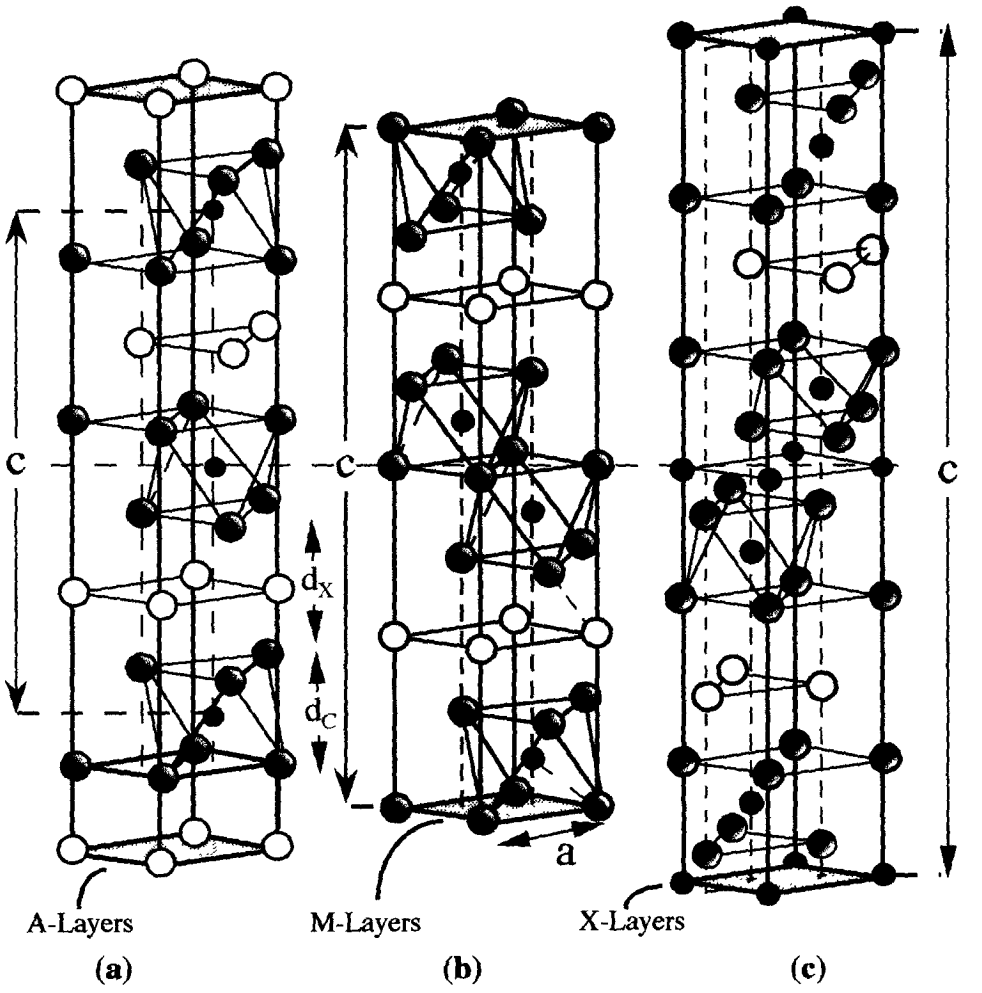

Figure 1: Unit cells of, a) 211, b) 312 and c) 413 phases. Unit cells are delineated by vertical arrows labeled c. The horizontal dashed line is drawn through the centers of the unit cells.

shown in Fig. 2 does not correspond to the unit cell shown in Fig. 1c. Thinning the samples results in a dimensionally induced polymorphic phase transformation, which involves the shearing of the Si or Al planes in opposite directions. These transformations in some ways resemble the dimensionally-induced HCP to FCC transformations observed in Ti-based thin multilayers[118-124]. More work, however, is required to establish the commonality of these phenomena and understand the nature of the driving forces and transformation mechanisms, neither of which is totally understood for the Ti-based work[118-123].

One of the leitmotifs of this work is the close resemblance in structure, and many of the properties, between the $M_{N+1}X_N$ phases and their corresponding stoichiometric MX binaries. It is thus useful at this juncture to briefly point out their structural similarities, which is best shown schematically (Fig. 3). To convert Ti_3SiC_2 (Fig. 3a) to TiC (or 413 to TiN): i) replace the Si atoms by C. This results in the highly twinned rock salt structure, wherein the planes previously occupied by the Si layers are now mirror planes (Fig. 3b); ii) de-twin every other Ti_3C_2 block of layers (by rotation around an axis perpendicular to c-axis). The resulting plane is the (110) plane.

Table 1: Summary of all $M_{N+1}AX_N$ phases known to date. The theoretical density (Mg/m^3) is in bold letters. The a and c lattice parameters (Å) are in brackets. Most of this list appeared in Ref. 1.

IIB	IIIA	IVA	VA	VIA
	Al **Ti_2AlC, 4.11** (3.04,13.60) **V_2AlC, 4.07** (3.1,13.83) **Cr_2AlC, 5.24** (2.86,12.8) **Nb_2AlC, 6.50**(3.10,13.8) **Ta_2AlC, 11.82** (3.07,13.8) **Ti_2AlN, 4.31** (2.989,13.614) **Ti_3AlC_2, 4.5** (3.075,18.578) **Ti_4AlN_3, 4.76** (2.988, 23.372)	**Si** **Ti_3SiC_2** **4.52** (3.0665,17.671)	**P** **V_2PC** **5.38** (3.077,10.91) **Nb_2PC** **7.09** (3.28,11.5)	**S** **Ti_2SC, 4.62** (3.216,11.22) **Zr_2SC, 6.20** (3.40, 12.13) **$Nb_2SC_{0.4}$,** (3.27,11.4) **Hf_2SC,** (3.36, 11.99)
Zn	**Ga** **Ti_2GaC, 5.53** (3.07, 13.52) **V_2GaC, 6.39** (2.93, 12.84) **Cr_2GaC, 6.81** (2.88, 12.61) **Nb_2GaC, 7.73** (3.13, 13.56) **Mo_2GaC, 8.79** (3.01, 13.18 **Ta_2GaC, 13.05** (3.10, 13.57) **Ti_2GaN, 5.75** (3.00, 13.3) **Cr_2GaN, 6.82** (2.875, 12.77) **V_2GaN, 5.94** (3.00, 13.3)	**Ge** **Ti_2GeC, 5.68** (3.07, 12.93) **V_2GeC, 6.49** (3.00, 12.25) **Cr_2GeC, 6.88** (2.95, 12.08) **Ti_3GeC_2, 5.55** (3.07, 17.76)	**As** **V_2AsC** **6.63** (3.11, 11.3) **Nb_2AsC** **8.025** (3.31, 11.9)	**Se**
Cd **Ti_2CdC** **9.71** (3.1, 14.41)	**In** **Sc_2InC** **Ti_2InC, 6.2** (3.13, 14.06) **Zr_2InC, 7.1** (3.34, 14.91) **Nb_2InC, 8.3** (3.17,14.37) **Hf_2InC, 11.57** (3.30,14.73) **Ti_2InN, 6.54** (3.07,13.97) **Zr_2InN, 7.53** (3.27,14.83)	**Sn** **Ti_2SnC, 6.36** (3.163,13.679) **Zr_2SnC, 7.16** (3.3576, 14.57) **Nb_2SnC, 8.4** (3.241,13.802) **Hf_2SnC, 11.8** (3.320,14.388) **Hf_2SnN, 7.72** (3.31,14.3)	**Sb**	**Te**
	Tl **Ti_2TlC, 8.63** (3.15,13.98) **Zr_2TlC, 9.17** (3.36,14.78) **Hf_2TlC 13.65** (3.32,14.62) **Zr_2TlN, 9.60** (3.3,14.71)	**Pb** **Ti_2PbC, 8.55** (3.20,13.81) **Zr_2PbC, 9.2** 3.38,14.66 **Hf_2PbC, 12.13** (3.55,14.46)	**Bi**	

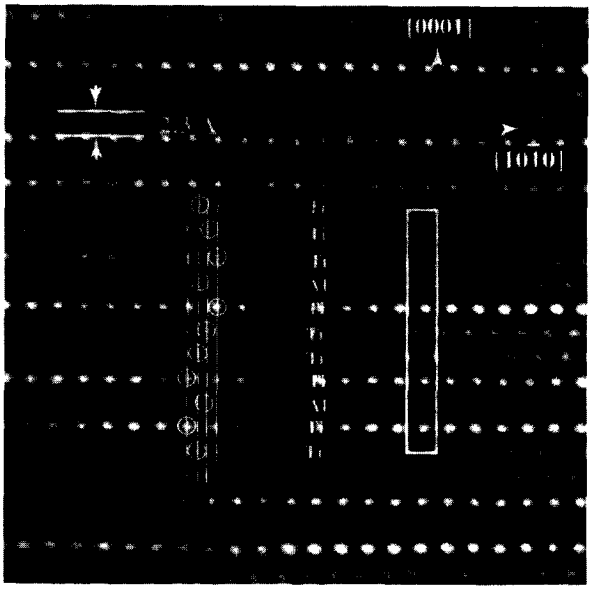

Figure 2: HRTEM image of $Ti_4AlN_{2.9}$ along [1 1 0] zone. The simulated contrast (thickness = 250 Å, defocus = – 48 nm), shown in inset, is superimposed on the experimental image.

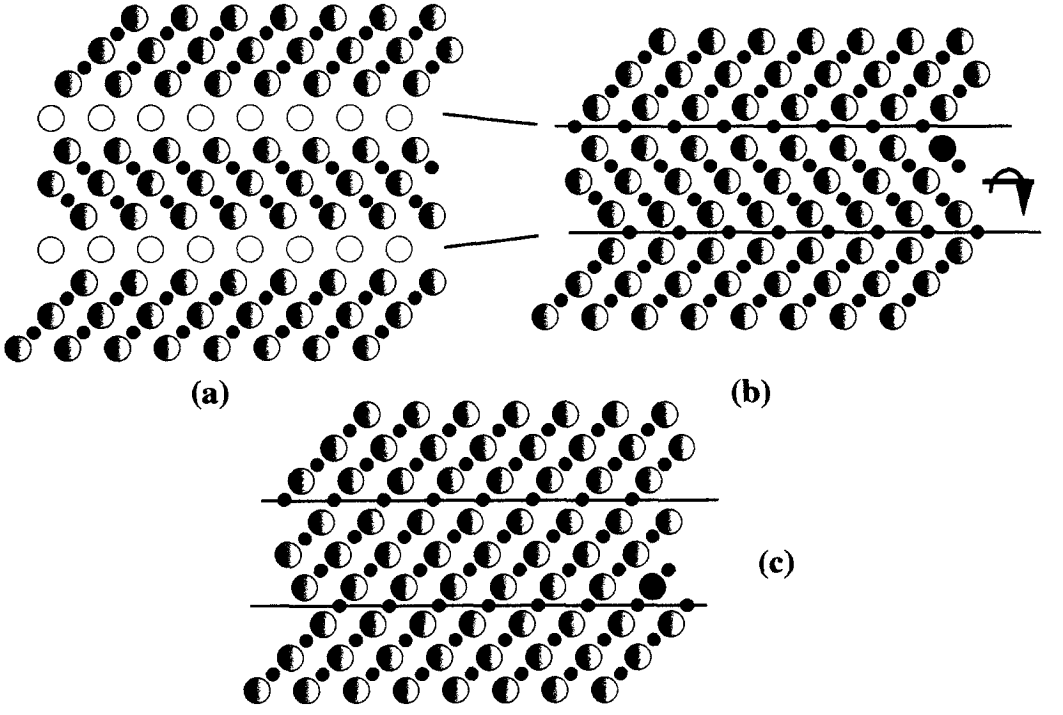

Figure 3: a) Schematic of (11 0) plane in Ti_3SiC_2. b) Replacement of Si by C atoms results in a highly twinned TiC structure. c) De-twining by rotation around axis shown in b results in TiC. Plane shown in (110) in TiC.

of the rock salt structure (Fig. 3c). In the case of Ti_3SiC_2, the transformation is associated with a 15 vol. % shrinkage. As discussed in section 8, this transformation is more than academic; it is one of the preferred modes by which Ti_3SiC_2 reacts and decomposes

Given the close similarities of the structures of the $M_{N+1}AX_N$ and MX phases, it is not surprising that an excellent, almost one-to-one, correlation exists between the a-lattice parameters[1] of the former, and the M-M distances in the corresponding MX binaries, d_{M-M}[124] (Fig. 4a)[1]. The inclined line in Fig. 4a has a slope of unity, which implies that for the most part, the correlation is excellent. For reasons that are not clear the Cr-containing ternaries (far left of figure) represent the only exception. A possible explanation could be that Cr is the only transition metal listed in Table 1 that does not crystallize in the rock salt structure. The M-M distances for Cr plotted in Fig. 4a are for Cr_2C_3.

Figures 4b and c plot the dependence of the c-lattice parameters of the ternary phases on d_{M-M} and d_A, the diameter of the A-group element. From these two figures the following salient points are noteworthy:

- The P, S and As-containing ternaries have significantly shorter c-lattice parameters than the Ge ones, which, in turn, are lower than those of the remaining compounds (Fig. 4b).
- For each A-group element, the c-parameter increases linearly with increasing d_{M-M} (Fig. 4b).
- The c/a ratio for the 211's range from 3.5 to 4.6, with the lowest values belonging to the P, S and As-containing ternaries, followed by those for Ge, etc. The simplest explanation is to assume the ternaries to be interstitial compounds in which the *A*- and *X*-atoms fill the interstitial sites between the M atoms. In such a scheme, the c-parameter, comprised of 4 M-layers per unit cell, should be $\approx$ 4 times the a-parameter, which is turn is $\approx d_{M-M}$. In other words, the 211's should have a c/a ratio of $\approx$ 4, as observed. Similar arguments for the 312's, with 6 layers of Ti atoms per unit cell, predict a ratio of $\approx$ 6; the 413's a ratio of $\approx$ 8. The actual c/a ratios are, respectively, $\approx$ 5.8-6[11,19] and 7.8[63 115], supporting the notion of interstitial compounds.
- The relationship between the c-parameter and d_A is more complicated, highly nonlinear, and separable into three regimes (Fig. 4c). For d_A < 2.5 Å the c-lattice parameters are relatively small and increase slightly with increasing d_A. Around 2.5 Å, there is strong, almost step-like, dependence of the c-parameter on d_A. For d_A > 2.5 Å, with the exception of the Nb, and maybe the Ti-containing ternaries, the c-lattice parameters are more or less independent of d_A. Even for the latter two, the dependence is much weaker for d_A > 2.5 Å. The most likely explanation for these observations is that for d_A < 2.5 Å the A-atoms are small enough to allow for the formation of d-d bonds between the M-layers on either side of them (Fig. 5c). Presumably, for d_A > 2.5 Å these bonds do not form, or if they do are weak, and the c-axis increases accordingly. Supporting evidence for this conjecture is shown in Fig. 4d, in which the width of the A-atom sandwich (see Fig. 1a), d_X, is plotted versus d_A. For the 211's, the former is related to d_c and c by[78]:

$$c \approx 2\, d_C + 2\, d_X$$

where d_C is defined in Fig. 1a (i.e. $d_C = a_{MX}/\sqrt{3}$, where a_{MX} is lattice parameter of MX's). The assumption made here is that d_X for the binaries and ternaries are identical, which is a good

[1] The results shown in Fig. 4a include the 211, 312 and 413 phases.

assumption[78]. Also plotted on the same figure, as a cross-hatched band are the d_{M-M} distances in the binaries, which clearly separate the S, P and As compounds with $d_X < d_{M-M}$, from the rest of the ternaries for which $d_X > d_{M-M}$. These conjectures notwithstanding, more work is needed to better understand the relationship between c and d_A.

Finally it is important to note that in addition to the list shown in Table 1, the number of solid solution permutations and combinations is obviously quite large; roughly a quarter of the periodic table could, in principle, come into play. It is possible to form solid solutions on the M sites, the A-sites and the X sites and combinations thereof. A continuos series of solid solutions, $Ti_2AlC_{0.8-x}N_x$, where x = 0 to ≈ 0.8, occurs at 1490 °C[125]. Furthermore, we have preliminary results that indicate that Ti_3SiC_2 and Ti_3AlC_2 also form a complete range of solid solutions. Solid

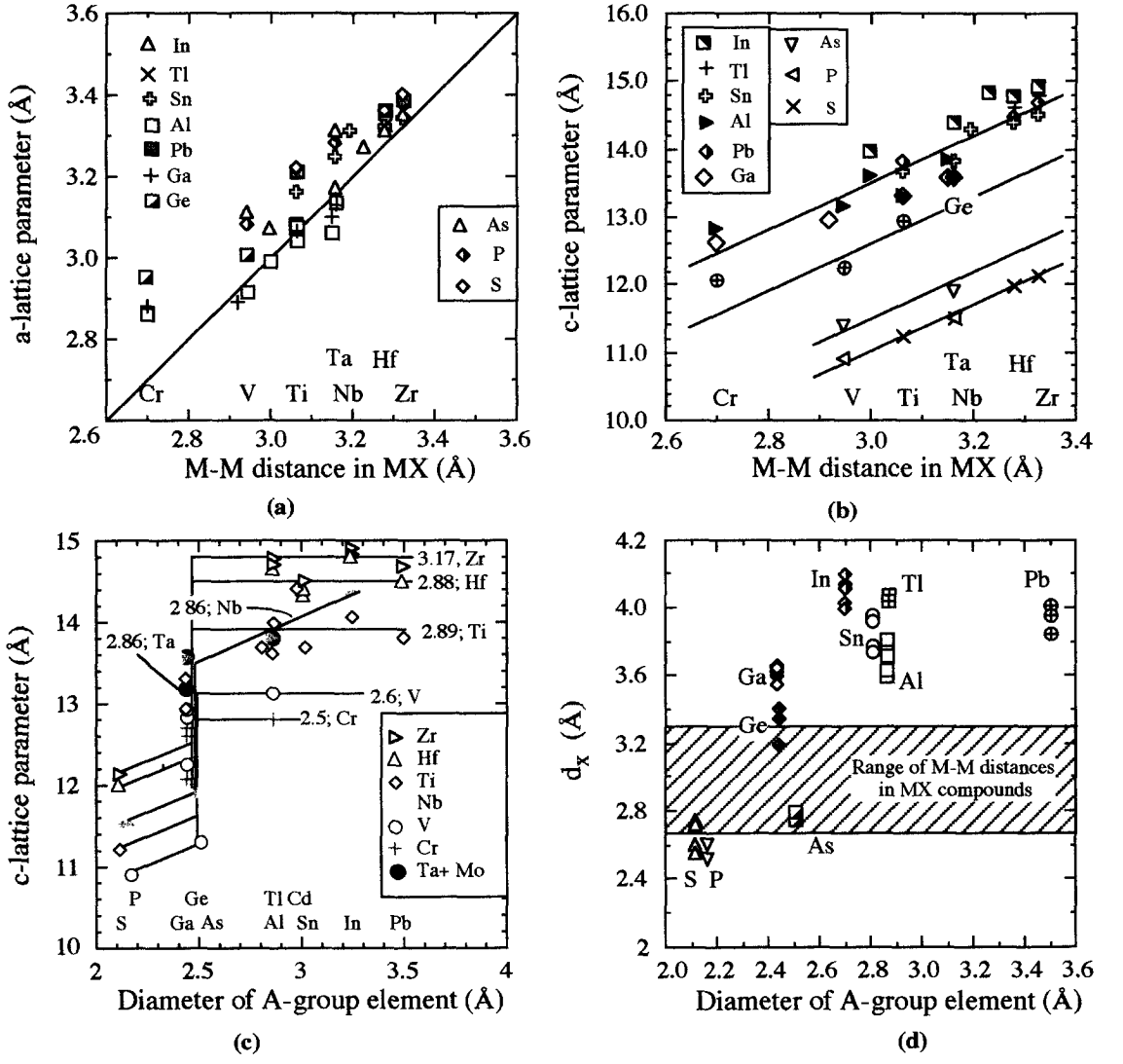

Figure 4: Functional dependence of: a) a-lattice parameter, and, b) c-lattice parameters in $M_{N+1}AX_N$ compounds on M-M distance in corresponding stoichiometric MX compounds. Dependence of: c) c-lattice parameters and, d) dx (see text) on diameter of A group element. Numbers in front of the transition metal elements in c denote their atomic radii.

solutions also form on the M-sites. Amongst the ones known to exist are: $(Ti,Cr)_2AlC$[18], $(Ti,V)SC$[126,127], $(Nb,Zr)_2AlC$, $(Ti,V)_2AlC$, $(Ti,Nb)_2AlC$, $(Ti,Ta)_2AlC$, $(V,Nb)_2AlC$, $(V,Ta)_2AlC$ and $(V,Cr)_2AlC$[10]. Interestingly enough, it has recently been shown that there is little solubility between B and C in the Ge-containing ternaries[128]. The generality of this result remains an outstanding question at this time.

3. THEORETICAL MODELING

Before delving in the details of some recent ab initio calculations for Ti_3SiC_2 and some of the other ternaries it is instructive to review the electronic structures of stoichiometric TiC and TiN[124,129-132], in which it is well established that all three main types of bonding, metallic, covalent and ionic exist. In both compounds, there is a non-vanishing density of states, DOS, at the Fermi level, E_F. For TiC, E_F falls in a local minimum; for TiN, E_F is pushed into the higher energy Ti d-d orbitals. The ionic contribution to the bonding results from a partial charge transfer from the Ti to the non-metallic element.

Three main types of covalent bonds have been identified in TiC and TiN. The lobes of the Ti_{eg} orbitals extend towards the neighboring non-metal atoms and can form pd_σ bonds with the 2p orbitals of the neighboring non-metal atoms (Fig. 5a). The lobes of the Ti t_{2g} orbitals are capable of forming pd_π bonds with the 2p orbitals of the adjacent non-metal atoms (Fig. 5b). These interactions are mostly bonding. Lastly, the same lobes can form metal-metal dd_σ bonds with t_{2g} orbitals of adjacent Ti atoms (Fig. 5c). This type of bonding occurs primarily at energies above E_F for TiC, and near E_F for TiN.

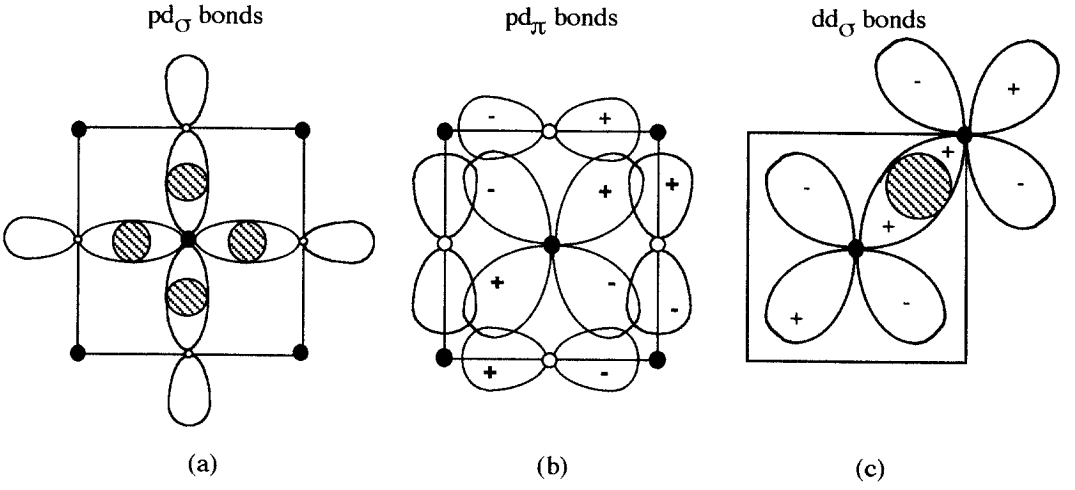

Figure 5: Schematic representation of: a) pd_σ bonds between Ti e_g and non-metal 2p orbitals in the (100) plane of NaCl structure; b) pd_σ bonds between Ti t_{2g}, and non-metal 2p orbitals; c) dd_σ bonds between Ti Ti t_{2g} orbitals. In all cases, the non-metal atoms are located at the center of each edge.

Not much exists along the lines of ab initio calculations for the $M_{N+1}AX_N$ phases. The first paper to tackle any of them (Ti_3SiC_2) was published late in 1998[133]. Since then the number of papers on the subject has increased[134-138]. To date the most active groups working on the subject are those of Medvedeva, Ivanovsky et al.[133-135], and Zhou and Sun[136-138]. The former use the full-potential linear-muffin-tin-orbital (FLMTO) method; the latter, a linear combination of atomic orbitals, LCAO, approach.

Not surprisingly there are many similarities between the electronic structures of the ternary phases and the corresponding binaries. There are, however, some important differences. The following conclusions, pertaining to Ti_3SiC_2 and Ti_3AlC_2, are based on the work of Medvedeva et al.[133-135]. They are:

- In both compounds there is substantial overlapping of the bonding and anti-bonding orbitals near E_f. The largest contribution comes from the 3d states of the Ti_I atoms[1] in the vicinity of the Si (Fig. 6a) or Al layers (Fig. 6b).
- Similar to TiC, the p-d interactions between Ti and C atoms are quite strong (Figs. 7c).
- The interactions between the Ti_I and Si or Al atoms (Fig. 7d) are weaker than the $Ti_{I,II}$-C interactions.
- The ionic component results from a charge transfer from the Ti to the other atoms. The effective charges of the muffin-tin spheres for Ti_3AlC_2 are[135]: Ti_I, + 0.21e; Ti_{II}, + 0.28e; Al, - 0.22e and C, - 0.26 e. The corresponding values for TiC[131] calculated by the FLMTO method are: Ti, - 0.36e; C + 0.43e; in TiN; Ti, - 0.32e; N, + 0.46e. And while the absolute values are comparable, they are, surprisingly, opposite in sign. In Ti_3AlC_2 electrons are transferred from Ti to the Al and C atoms, while in TiC the transfer is in the opposite direction. In this respect, it is worth noting that the direction of charge transfer in TiC has not been unambiguously determined. For example the LCAO models predict a charge transfer from the metal to C[132], which is opposite to that of the muffin tin approximation[131].
- All models predict an anisotropy to the electrical conductivity.
- For Ti_3SiC_2, E_F coincides with a peak at $\approx$ 5 states/(eV•unit cell) in the total DOS (Fig. 6a). In Ti_3AlC_2, E_F falls in a local minimum, and the total DOS is 3.35 states/(eV•unit cell). Both of these values are in excellent agreement with our measured values[87,88] (see below).
- Within the basal planes dd_π interactions between the Ti atoms play a role in the bonding (Figs. 7a and 7b). However, the bonds between the Ti_I atoms (Fig. 7a) are stronger than those between the Ti_{II} atoms (Figs. 7b). The same is true for Ti_3AlC_2. The reason for this state of affairs is believed to be a weakening of the Ti-Si and Ti-Al bonds which considerably strengthens the metallicity of the Ti_I 3d bonds. This weakening is believed to occur by a redistribution of electrons from the Ti 3d-C 2p sub-band into the Ti_I 3d, 4s metallic bonds. The same conclusion was reached for Ti_3GeC_2[138]. At around E_F, the DOS originates from

[1] For sake of consistency, the following notation scheme is used throughout this paper. The M and X-atoms adjacent to the A-layers are labeled as I; those farther away by II. Note that in the 211, there are 3 unique atoms, in the 312's four, and in the 413's five.

nearly free electron states of the Ti_I atoms. Interestingly enough, symmetry dictates that the Ti_I-Ti_I bonds be equal in length to the Ti_{II}-Ti_{II} bonds.

Qualitatively the results of Sun and Zhou[136-138] (Fig. 6c) are comparable to those of Medvedva et al. Quantitatively, however, their $N(E_F)$ is of the order of 50-60 states/(eV•unit cell)[136,138]; values that are simply too high, and not supported by experiment. At the other extreme their DOS values at E_F for Ti_2AlC and Ti_2AlN are quite low[13] and comparable to stoichiometric TiC.

Partial support for the conclusions of the ab initio calculations can be found in recent X-Ray photoelectron spectroscopy, XPS, measurements[73,74] on Ti_3SiC_2, $Ti_3Al_{1.1}C_{1.8}$ and $Ti_4AlN_{2.9}$ summarized in Table 2. The salient points are:

• The Si 2p level in Ti_3SiC_2 occurs at 98.5 eV; a value substantially lower (i.e. less bound) than in bulk Si (99.5 eV), SiO_2 (103.5 eV), SiC (100.5 eV) or Si_3N_4 (101.8 eV). This indicates the relative weak bonding of Si to its surroundings.

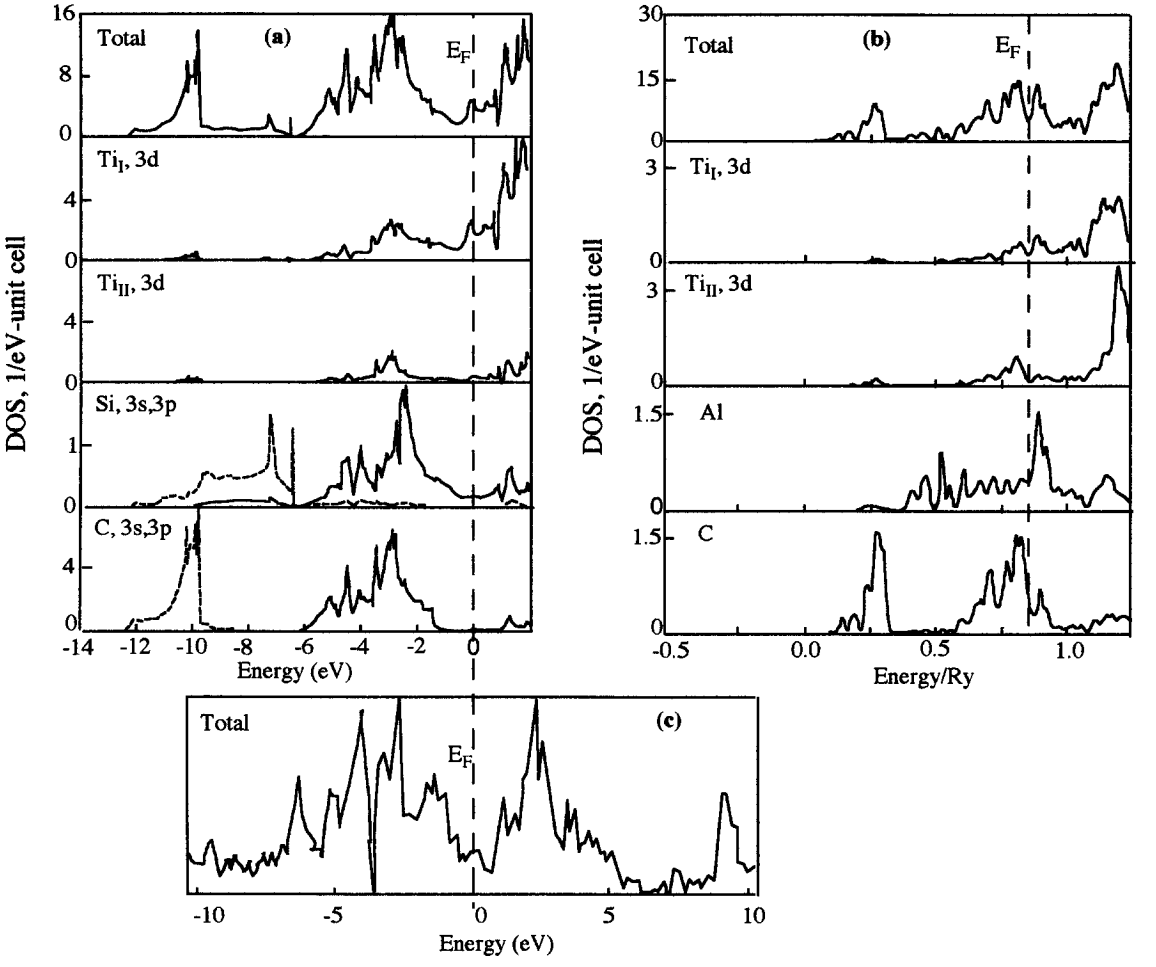

Figure 6: Total (top) and local DOS's for a) Ti_3SiC_2 from Ref. 133, and b) $Ti_3Al_{1.1}C_{1.8}$ from Ref. 135 and; c) Ti_3SiC_2 from Ref. 136. The x-axis in c is drawn on the same scale as the one in a.

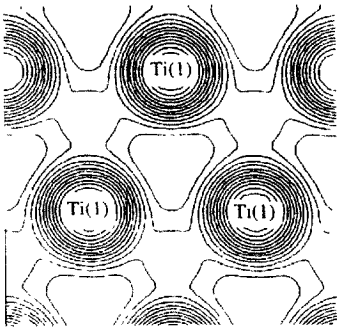

(a)

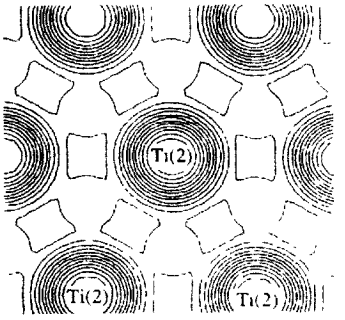

(b)

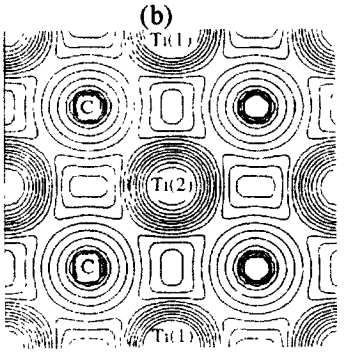

(c)

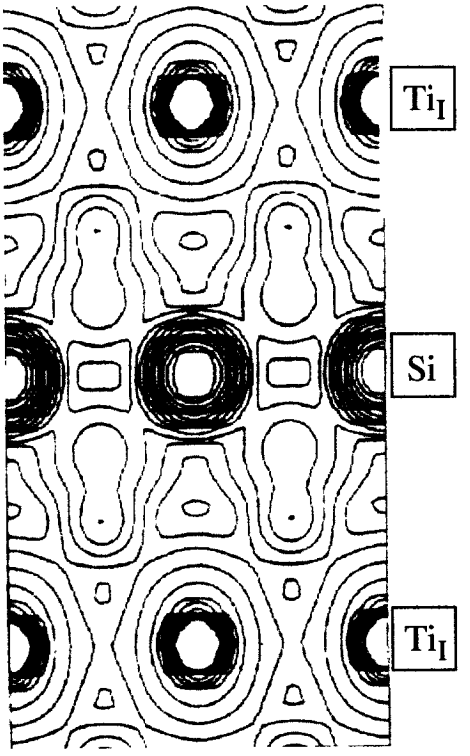

(d)

Figure 7: Charge density distribution, according to Ref. 133, in: a) (100) monolayers composed of Ti_I atoms; b) Ti_{II} atoms; c) Ti_I-C-Ti_{II} layers, and; d) Ti_I-Si-Ti_I layers.

• The binding energies of Al in the $Ti_3Al_{1.1}C_{1.8}$ and $Ti_4AlN_{2.9}$ structures, ($\approx$ 72 eV) are nearly 1 eV higher (i.e. better bound) than those in pure Al. This despite the fact that the Al-Al bond lengths in the ternaries ($\approx$ 3.0 Å) are longer than the ones in pure Al (2.863 nm). This is strong evidence that the enhancement in bonding of the Al atoms results from their bonding to the XTi_6 blocks, and *not* from bonds formed between them.

• Not surprisingly, the binding energies of the C atoms in the 312 structures are quite comparable to each other and to those in stoichiometric TiC. The same is true for the binding energies of the N atoms in $Ti_4AlN_{2.9}$ and stoichiometric TiN.

Table 2: Binding and kinetic energies for Ti_3SiC_2, Ti_3AlC_2, Ti_4AlN_3 and related compounds[73,74]

	XPS/XAES features (eV)			
Compound	Si or Al (2p)	Si or Al (KLL)	Ti (2p)	C or N (1s)
Carbides				
Ti_3SiC_2	98.5/102.3	1617.4/1610.6	454.0	281.0
Ti_3AlC_2	71.9	1393.4	454.5	281.5
TiC	-	-	454.4	281.6
Nitrides				
Ti_4AlN_3	72.0	1393.7	454.7	396.9
TiN			455.5	396.7
AlN	74.1	1388.6		397.3

- The binding energies of the Ti atoms in the 312's are comparable to each other and to those in stoichiometric TiC. The binding energies are also quite comparable to those in metallic Ti (454.0 eV). Why the binding energy of Ti in stoichiometric TiN is about 1 eV higher than 413, despite the fact that the Ti-N bond lengths in the TiN are longer (Table 3) is not clear at this time.
- The Al and N atoms are better bound in AlN than in the ternaries.

As discussed in the next section, the XPS results are in good agreement with the structural results as determined from Rietveld analysis of neutron and X-ray diffraction, XRD results.

4. THERMAL PROPERTIES

Further evidence for the conclusions reached above are presented in this section in which the thermal properties of some of the ternary compounds are reviewed in detail.

4.1 Rietveld Analysis of Room Temperature Neutron Diffraction Data

The merits of the FLMTO model can be appreciated by a comparison of the various bond lengths in Ti_3SiC_2 and $Ti_4AlN_{2.9}$ determined from Rietveld analysis of room temperature ND data summarized in Table 3[63,77]. Also included in the table are the bond lengths for Ti_2AlN[4], stoichiometric TiN and TiC[124], Ti, Si and Al. These results indicate that:

- On *average*, the Ti-X bonds in the ternaries are slightly shorter than the corresponding stoichiometric Ti-X bonds in the binaries. This is an important result, the full implications of

which will be discussed shortly.

• In both Ti_3SiC_2 and $Ti_4AlN_{2.9}$, the Ti_I-X bonds are shorter than the Ti_{II}-X. The fact that the Ti_{II}-N_{II} bonds are longer, and thus presumably weaker than the Ti_I–N_I bonds is consistent with

Table 3: Bond lengths (Å), from Rietveld refinement of neutron powder diffraction data of Ti_4AlN_3[63] and Ti_3SiC_2[77]. Also included are bond lengths for Ti_2AlN, TiC, TiN, Ti, Al and Si.

Compound	Atoms	Bond Length (Å)
$Ti_4AlN_{2.9}$ [Ref. 63]	Ti(II) - N(II)	2.141(2)
	Ti(II) - N(I)	2.093(2)
	Ti(I) - N(I)	2.080(2)
	Ti(II) – Ti(II)[a]	2.988[b]
	Ti(II) – Ti(I)[c]	2.913(4)
	Ti(I) - Ti(I)[a]	2.988[b]
	Ti(I) – Al	2.818(3)
	Al – Al	2.988[b]
Ti_2AlN [Ref. 4]	Ti – N	2.087
	Ti – Ti[a]	2.994
	Ti – Ti[c]	2.910
	Ti – Al	2.823
	Al – Al	2.994
Ti_3SiC_2 [Ref. 77]	Ti(I) – C	2.085(2)
	Ti(II) – C	2.1814(8)
	Ti(I) – Ti(I)[a]	3.06557(6)
	Ti(I) – Ti(II)[c]	2.9634(2)
	Ti(II) – Ti(II)[a]	3.06557(6)
	Ti(I) – Si	2.693(2)
	Si – Si	3.06557(6)
TiC[132] (stoichiometric)	Ti – Ti	3.062
	Ti – C	2.165
TiN (stoichiometric)	Ti – Ti	2.997
	Ti-N	2.12
Ti	Ti-Ti	2.951[a]
		2.987[c]
Al	Al – Al	2.863
Si	Si – Si	2.352

[a]distance between atoms within a layer

[b]distance determined due to special positions (1/3, 2/3, z)

[c]distance between atoms in different layers

the independently obtained evidence that the N-vacancies occur preferentially on the N_{II} sites[63]. This somewhat surprising result is not totally understood at this time. According to the FLMTO calculations, and as a result of the relative weakening of the Ti_I-Si bonds, the bonding between the Ti_I atoms within the basal planes is stronger than that between the Ti_{II} atoms (Figs. 7a and b). A similar charge transfer into the Ti_I-C bonds could explain this observation as well.

- The Ti_I-Ti_{II} distances in $Ti_4AlN_{2.9}$ and Ti_2AlN are comparable and shorter than those in Ti_3SiC_2.
- The a-lattice parameters of the ternary phases are almost identical to the M-M distances in the corresponding stoichiometric MX compounds, in agreement with the preceding discussion (Fig. 4a).
- Despite considerable overlap between the Ti d and Si p-orbitals (Fig. 6a) the Ti_I-Si distance in Ti_3SiC_2 (2.685 Å) is substantially longer than the ideal Ti-Si covalent distance (2.54 Å) but shorter than the corresponding distance in $TiSi_2$ (2.76 Å). This indicates that the Ti-Si bonds along the c-axis are stronger than those in $TiSi_2$, which melts at 1470 °C.
- The Si-Si distance in elemental Si (2.3532 Å) is considerably shorter than the Si-Si distance in Ti_3SiC_2 (3.0656 Å). Consequently, and in contrast to the FLMTO calculations that suggest otherwise[133], the presence of Si-Si bonds in Ti_3SiC_2 is highly unlikely. Similarly, the Al-Al distances in pure Al are shorter than those in $Ti_4AlN_{2.9}$.

Further insight into the bonding can be gleaned from analyzing the temperature dependence of the equivalent isotropic, U_{eq}, atomic displacement parameters, ADPs, of the unique atoms in Ti_3SiC_2 and $Ti_4AlN_{2.9}$ listed in Table 4 and shown in Figs. 8a and b, respectively[77,98]. The ADP is a measure of the mean-square displacement amplitude of an atom about its equilibrium position. At all temperatures, but especially at the higher temperatures, the amplitudes of vibration of the Si and Al atoms are considerably higher than the Ti or X atoms (Figs. 8a and b). Furthermore, at all temperatures, the amplitudes of vibrations of the Si atoms are higher than those of the Al atoms (Table 4 and Fig. 8). This is consistent with the lack of restraint, or absence of bonds, along the a-axis in the case of the Si atoms.

The thermal ellipsoids (99% probability) at room, and elevated temperatures for Ti_3SiC_2 (Figs. 9a,b) and $Ti_4AlN_{2.9}$ (Figs. 9c and d) are also instructive. From these results it is clear that the vibrations of the Ti and X atoms are comparable, and lower than those of Si and Al. At the highest temperatures examined (Figs. 9b and d), the Si and Al-atoms vibrate more along the a-axis that along the c-axis once again consistent with the idea that there is little bonding between the Si or Al atoms themselves.

The room temperature U_{eq} values for stoichiometric TiC and TiN[139,140] are also listed in Table 4. On *average* (last row in Table 4) $\overline{U}_{eq}$ of the atoms in Ti_3SiC_2 are comparable to those in stoichiometric TiC; this is true even when the amplitudes of vibration of the Si atoms are included In contrast, the *average* $\overline{U}_{eq}$ at room temperature of $Ti_4AlN_{2.9}$ are, not only significantly lower than those in stoichiometric TiN[139,140], but even lower than the corresponding

values in stoichiometric TiC[139,140] (Table 4); here again even when the values for the Al atoms are included. This once again reflects the strengths of the bonds in these solids.

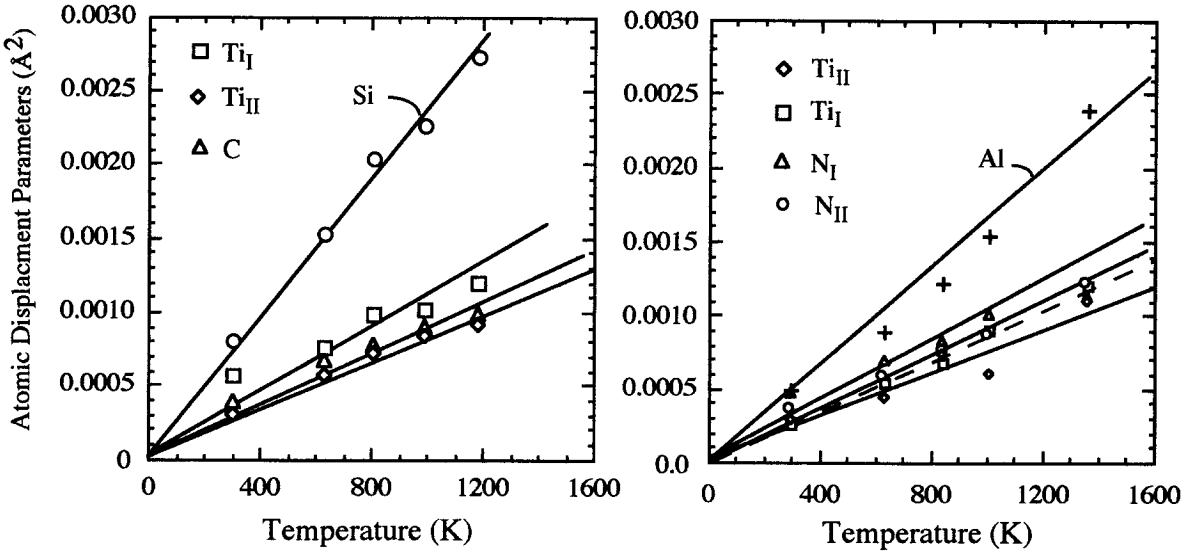

Figure 8: Temperature dependence of U_{eq} for the unique atoms in: a) Ti_3SiC_2[77], and b) Ti_4AlN_3[98] structures.

Table 4: Summary of room temperature U_{eq} (Å^2) for Ti_3SiC_2, $Ti_4AlN_{2.9}$, stoichiometric TiC and TiN.

Atom	Ti_3SiC_2 (Ref. 77)	TiC	$Ti_4AlN_{2.9}$ (Ref. 98)	TiN
Ti_I	0.0057(6)	0.0033[139]	0.0029(6)	
Ti_{II}	0.0029(9)		0.0026(7)	
Si or Al	0.0080(6)		0.0044(8)	
C or N_I	0.0038(3)	0.0056[139]	0.0036(3)	
N_{II}			0.0046(4)	
Average	0.005	0.0045[139]	0.0034	0.0083[140]

The Debye temperature, θ_D, is related to $\overline{U}_{eq}$'s by the following equation[141].

$$\theta_D = \frac{6\xi h^2}{8\pi^2 m k_B \overline{U}_{eq}^2}\left\{\frac{\phi(x)}{x} + \frac{1}{4}\right\} \quad (1)$$

where k_B, h, m and ξ are, respectively, Boltzmann's and Planck's constants, the molecular weight and the number of atoms per formula unit. x is the ratio of θ_D to the absolute temperature and:

$$\phi(x) = \frac{1}{x}\int_0^x \frac{\varsigma}{e^{\varsigma} - 1} d\varsigma \quad (2)$$

The θ_D's of Ti_3SiC_2 and $Ti_4AlN_{2.9}$ estimated from the $\overline{U}_{eq}$, averaged over all temperatures are listed in the last column in Table 6. These values, while still quite high, are $\approx$ 12 to 15 % lower

than the θ_D's calculated using other techniques (see below). It should be noted that Eq. 1 is strictly applicable only to a cubic crystal containing only one atom. Nevertheless, it is useful for comparison purposes, especially if the structures compared are similar or related.

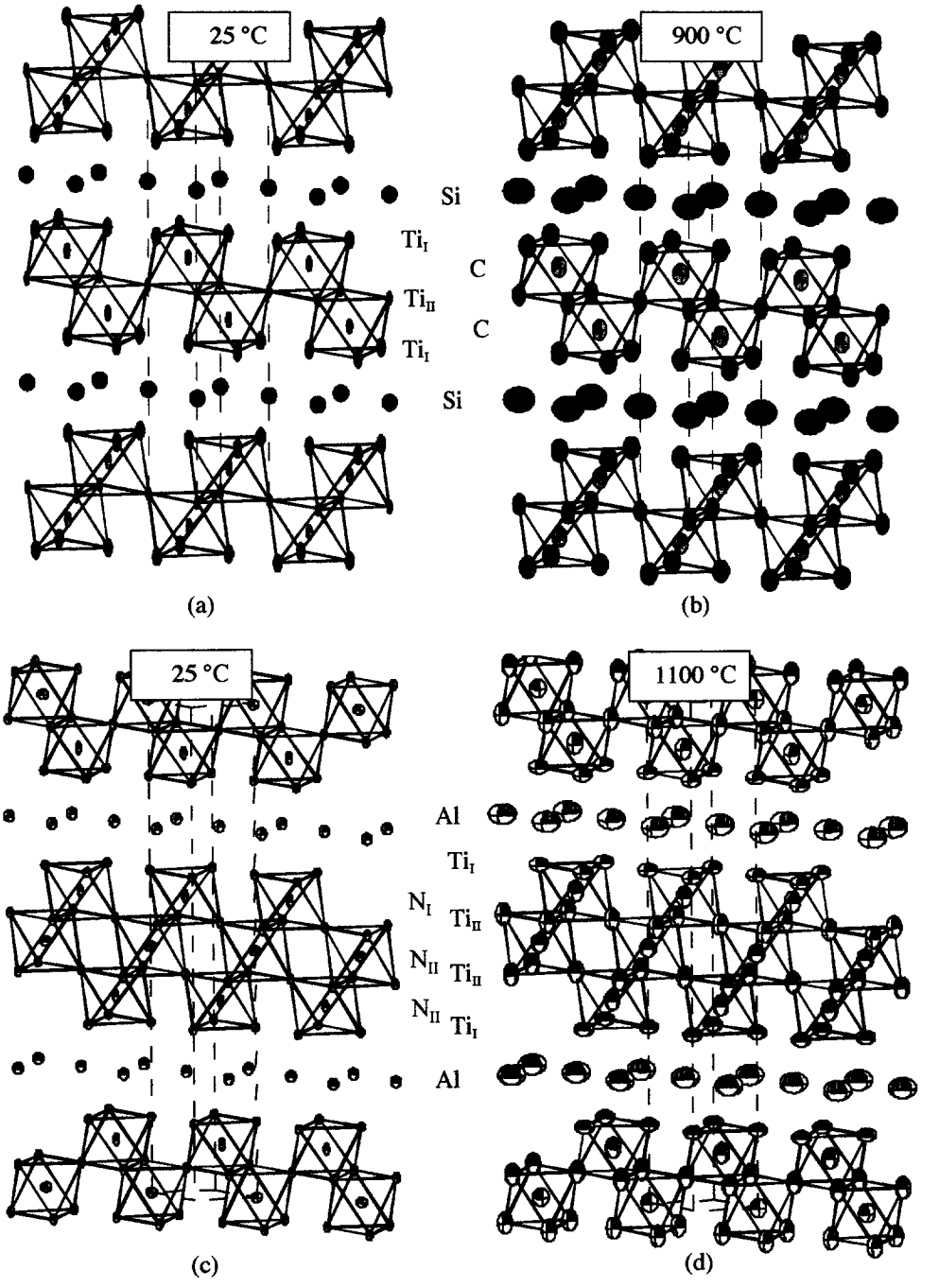

Figure 9: Thermal ellipsoids (99% probability) of atoms: a) Ti_3SiC_2[77] at 298 and, b) 1173 K; c) Ti_4AlN_3[98] at c) 298 and d) 1367 K. The dotted lines outline one unit cell.

In summary, both the XPS and ND results suggest that the A-atoms are strongly bonded to the XTi_6 blocks via, presumably, p-d overlap *out* of the basal planes, and not through bonds *in* the basal planes. This overlap is stronger in the Al-containing ternaries than in Ti_3SiC_2. Whether these conclusions extend to the other $M_{N+1}AX_N$ compounds, especially those in which the A-atoms are large (e.g. Sn, Pb, In, etc.) is unknown at this time. More ND work is indicated and should be carried out.

4.2 Heat Capacities, Thermodynamic Parameters and Thermal Stability

The molar heat capacities at constant pressure, c_p, of Ti_3SiC_2[77], $Ti_4AlN_{2.9}$[98] and Nb_2SnC[103] in the 300 to 1300 K temperature range are plotted (open symbols) in Fig. 10. The results for Ti_2AlC[104] are almost indistinguishable from those of Nb_2SnC and are not shown. The gray lines represent the best fit of the experimental points using the Debye model. Also plotted in Fig. 10, as filled symbols, are the data corresponding to (N+1) x c_p of the corresponding MX binaries. The two sets of results are almost indistinguishable, which implies that as a first approximation, the entropy content of the binaries and ternaries are comparable. The latter can thus be used until the thermodynamic parameters of the ternaries are independently measured.

Furthermore, since on average the bond distances in the ternaries and the corresponding binaries, are comparable, it follows that as a first approximation, the standard free energies of formation of the ternaries, $\Delta G°_f$ are (N+1) times those of the corresponding binaries[145]. In other words:

$$\Delta G°_f (M_{N+1}AX_N) = (N+1) \times \Delta G°_f (MX) \quad (3)$$

Only two reports exist in the literature for the experimental determination of $\Delta G°_f$[46,146] of Ti_3SiC_2. The reliability of the earlier results[146], is suspect, however, since they predict an increase in the stability of Ti_3SiC_2 with increasing temperatures. In a more recent paper, Du et al.[46], using a combination of theoretical modeling and experimental observations, concluded that $\Delta G°_f$ of Ti_3SiC_2 from the elements is:

$$\Delta G°_f \text{ (kJ/mol)} = -547{,}145 + 24.84\,T \quad (4)$$

Their results are listed in Table 5, together with 3 times those of TiC in the 300-1500 K temperature range. The two sets of results are quite close; the maximum deviation being 2.5 % at 1500 K. Thus, based on one datum point it appears that not only are the entropies of the ternaries and binaries comparable on an absolute scale, but their $\Delta G°_f$'s as well. Whether this is a general conclusion that applies to the other ternaries as well will require further experimentation. These

Table 5: Comparison of temperature dependence of $\Delta G°_f$ (kJ/mol) for Ti_3SiC_2, and 3 times $\Delta G°_f$ of stoichiometric TiC and difference between them.

Temp., K	300	500	700	900	1100	1300	1500	Ref.
Ti_3SiC_2	- 539.7	- 534.7	- 529.76	- 524.8	-519.8	-514.85	-509.9	46
3 x TiC	- 541.2	- 534.1	- 527.49	- 521.1	- 514.7	- 506.46	- 497.46	144
% difference	- 0.28	0.11	0.43	0.7	1	1.65	2.5	

caveats notwithstanding, and until the thermodynamic parameters of the ternary compounds are measured, a good approximation is to use the corresponding parameters for the MX binaries multiplied by the appropriate (N+1) factor

The $M_{N+1}AX_N$ ternaries do not melt; rather they decompose peritectically according to the following reaction:

$$M_{N+1}AX_N \Rightarrow M_{N+1}X_N + A \quad (I)$$

The decomposition temperatures vary over a wide range; from ≈ 850 °C for Cr_2GaN[85] to above 2300 °C for Ti_3SiC_2[46]. The decomposition temperatures of the Sn-containing ternaries range from 1200 to 1400 °C[69,99], and appear to scale with the melting point of the corresponding MX phases (see Fig. 11). Given the stability of the $M_{N+1}X_N$ blocks and the fact that the A-layers are relatively loosely held in the structure, this result is not too surprising.

Another complicating factor that is important to appreciate and that has caused, and is still causing, considerable confusion in the literature is that the decomposition temperature is a strong function of impurities, both metallic impurities like Fe or V[93], as well as non-metallic impurities such as O. This sensitivity to impurities could partially explain the misconception that Ti_3SiC_2 was unstable above ≈ 1450 °C[32,33,39].

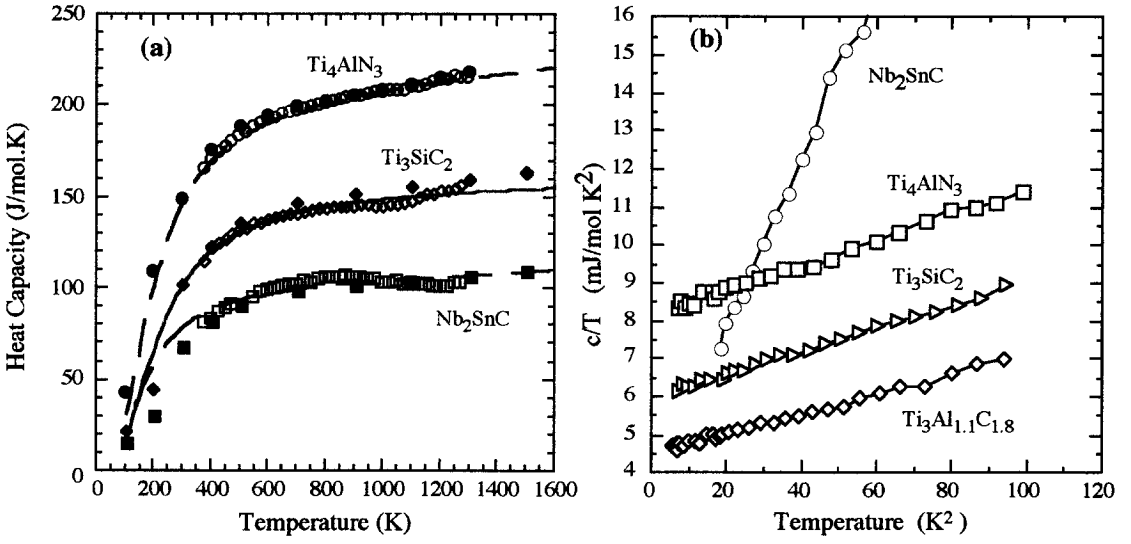

Figure 10: Temperature dependencies of c_p of Ti_4AlN_2[98], Ti_3SiC_2[77], and Nb_2SnC[103], represented by open symbols. Filled symbols are the corresponding c_p values for the MX compounds multiplied by the appropriate (N+1) factor in $M_{N+1}AX_N$. Solid gray lines are best fits using the Debye model. b) Low temperature c_p data plotted as c_p/T versus T^2 (see text).

4.3. Low Temperature Heat Capacity

In the 2 to 15 K temperature range c_p monotonically increases with increasing temperature. When replotted as c_p/T versus T^2 (Fig. 10b), a linear fit representing:

$$c_p/T = \gamma + \beta T^2$$

prevails, confirming that,

$$c_p = \gamma T + \beta T^3 \quad (5)$$

as expected for well behaved metallic-like conducting materials. The parameters γ and β, are the coefficients of the electronic and lattice heat capacities, respectively. Table 6 compares these parameters for Ti_3SiC_2, $Ti_3Al_{1.1}C_{1.8}$ and $Ti_4AlN_{2.9}$[87,88], with some other Ti-containing solids. The values of γ range from a high of 8.12 mJ/mol•K^2 for $Ti_4AlN_{2.9}$, to a low of 4.48 mJ/mol•K^2 for $Ti_3Al_{1.1}C_{1.8}$. The β values range from a low of 0.026 mJ/mol•K for $Ti_3Al_{1.1}C_{1.8}$, to a high of 0.05 mJ/mol•K for Ti_3SiC_2. The low temperature c_p of Ti_3SiC_2 was measured twice; in the first measurement[87], a higher β value was obtained than in a subsequent measurement[88]. The latter is deemed more accurate.

Following the free electron model, γ is related to $N(E_F)$ by:

$$N(E_F) = \frac{3\gamma}{\pi^2 k_B^2} \quad (6)$$

Based on the results shown in Table 6, the $N(E_F)$ values are 3.8 (eV•unit cell)$^{-1}$ for $Ti_3Al_{1.1}C_{1.8}$ and 6.9 for Ti_4AlN_3 (eV•unit cell)$^{-1}$, the former in excellent agreement with the results of the FLMTO calculation[135]. Our first determination of $N(E_F)$ for Ti_3SiC_2[87], yielded 4.4 (eV•unit cell)$^{-1}$, the second[88], yielded 5 (eV•unit cell)$^{-1}$; both values again in excellent agreement with the theoretical values of 4.76[133] (eV•unit cell)$^{-1}$ and 5.55[135] (eV•unit cell)$^{-1}$.

According to Fig. 6, the Fermi level is located in the d-d Ti band and it is thus instructive to normalize the DOS's of the ternaries to a *per* Ti atom basis. When thus normalized (column 5 in Table 4), the range in DOS values narrows significantly (0.63 to 0.86 (eV•Ti atom)$^{-1}$). These values are roughly half those for Ti metal[144] (1.43 (eV•Ti atom)$^{-1}$). Also included in Table 6, are the DOS values for stoichiometric TiC and TiN. The $N(E_F)$ for the former is quite low (< 0.025-0.1 (eV Ti•atom)$^{-1}$) because, as noted earlier, E_F falls in a minimum of the DOS function[131,144].

The characteristic Debye temperature, θ_D, is related to β by:

$$\theta_D^3 = \frac{12\pi^4 N_{Av}\, \xi k_B}{5\,\beta} \quad (7)$$

where N_{Av} is Avogadro's number. Accordingly, with $\xi = 5.9$ for $Ti_3Al_{1.1}C_{1.8}$, a θ_D value of 764 K is obtained; the corresponding values for $Ti_4AlN_{2.9}$ and Ti_3SiC_2 are, respectively, 779 and 715 K. These θ_D values (column 7, Table 6) are in fair agreement with the θ_D values found from elastic constant measurements (column 8; see below) and from the Rietveld analysis of the ND scattering (last column) results discussed in the previous section. As is typical for many solids, the Debye temperatures calculated from elastic constant measurements are higher than those from the ND scattering, with those calculated from low temperature c_p measurements in between[142,147].

Table 6: Parameters derived from low temperature c_p measurements. Unless otherwise noted the results are taken from Ref. 88. Also included are the various values of the Debye temperatures derived from other methods and other Ti-containing compounds.

Material	γ (mJ/mol K^2)	$N(E_F)$ (eV• unit cell)$^{-1}$	$N(E_F)$ Theo. (eV• unit cell)$^{-1}$	$N(E_F)$ (eV•Ti atom)$^{-1}$	β (mJ/mol• K)	θ_D (K)		
						Low T c_p	Acoustic	HT ND
$Ti_3Al_{1.1}C_{1.8}$	4.48	3.8	3.35[135]	0.63	0.026	764	758[91]	-
$Ti_4AlN_{2.9}$	8.12	6.9	--	0.86	0.033	779	762[91]	682[98]
Ti_3SiC_2	5.21[87] 5.9	4.42[87] 5	4.8[133] 5.55[135]	0.73[87] 0.83	0.050[87] 0.032	620[87] 715	780[91]	608‡
Ti	3.36[143]			1.43[143]	0.026[143]	420[143]		
$TiC_{0.97}$	< 1	0.1-0.5[142]	≈ 0.3[144]	0.025-0.125		845[142]	940[142]	
TiN	2.5-3.3[142]	4.25-5.6[142]	≈ 0.9[144]	1.1-1.4			636[142]	

Clearly, one Debye temperature representation for an anisotropic, multi-element material is an oversimplification. This caveat notwithstanding, the θ_D values for the 312's and 413's are significantly higher than those of Ti or Ti_3Al, and comparable to those for $TiC_{0.97}$ (Table 6). This must reflect the partial, but significant, covalent and ionic character of the Ti-Ti, Ti-C or Ti-N bonds in the ternaries. To be further noted, the θ_D value for pure Ti is already amongst one of the higher ones in metals and alloys.

The only 211 phase for which the c_p has been measured at low temperatures is Nb_2SnC[103]. The results are shown in Fig. 10b. Not surprisingly, reducing the number of M-X-M layers to one, from two or three, results in a significant decrease in the Debye temperature (315 K). The DOS *per* Nb atom (0.66 (eV•Nb atom)$^{-1}$) is ≈ 5 times smaller than the corresponding value in elemental Nb[148].

4.4. Thermal Expansion

The bulk dilatometric thermal expansion coefficients, TEC's, of the ternaries measured to date are listed in Table 7; they range from a low of ≈ 7.5, to a high of 10.5 x 10^{-6} K^{-1}. Interestingly enough the highest value is that of the quaternary compound[97], $TiAlC_{0.5}N_{0.5}$. This value is significantly higher than the TEC's of the end members and, as discussed below, is a strong indication for the presence of a solid solution softening effect in this system at higher temperatures.

For a given A-element the TEC's of the ternaries scale with those of the corresponding MX binaries. This is obvious from Fig. 11, in which the TEC's of the Sn- and Pb-containing ternaries and corresponding binaries, MC's, are plotted versus the melting point of the latter[149].

Once again given the structural similarities, such a correlation is not surprising. Furthermore, since the TEC's of the ternaries are higher than their corresponding binaries, this implies the M-A bonds are, on average, weaker than the MC bonds; again no surprises.

Table 7: Summary of dilatometric thermal expansion results. (x 10^6 K^{-1}) The uncertainty for most the values is ± 0.2.

Compound	TCE	Compound	TCE	Compound	TCE
Ti_2AlC	8.8	Ti_2AlN	8.2	$Ti_2AlN_{0.5}C_{0.5}$	10.5
Ti_3SiC_2	9.1	Ti_3AlC_2	9.0	$Ti_4AlN_{2.9}$	9.7
Ti_2SnC	10	Zr_2SnC	8.3	Nb_2SnC	7.8
Hf_2SnC	8.1	Zr_2PbC	8.2	Hf_2PbC	8.3
Nb_2AlC	7.5	(NbTi)AlC	8.5		

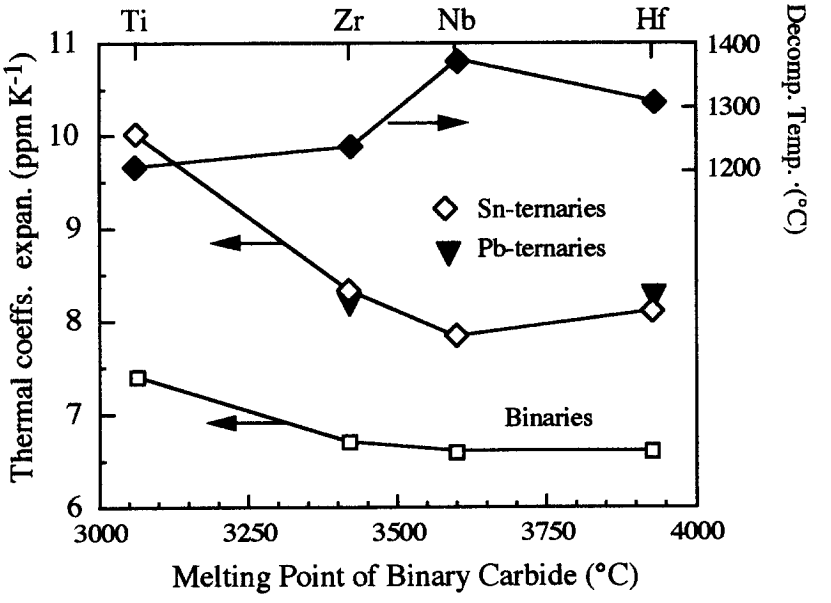

Figure 11: Thermal coefficients of expansion, TCE's, of Sn- and Pb-containing M_2AC phases in the 25-1000 °C temperature range[99] plotted as a function of melting points of corresponding stoichiometric MC's. Also plotted (lower line) are the TCE's of the latter. Uppermost curve is a plot of the decomposition temperatures of the Sn- and Pb-containing M_2AC phases[99].

To gain further insight into the thermal expansion behavior of these ternaries the lattice expansions along the *a*- and *c*-directions for a number of ternaries were calaculated from high temperature diffraction experiments. The results are summarized in Table 8, from which one can conclude that:

- Along the c-axis, the Ti-C bonds in Ti_2AlC[104] are weaker than the Ti-N bonds in Ti_2AlN. The opposite is true along the a-axis. The same reversal is also apparent when Ti_3SiC_2 and Ti_4AlN_3 are compared. This is further evidence for the strengths of the Ti-Al bonds in the c-direction.

- The bulk TEC's of Ti_2AlC and Ti_2AlN are comparable, but the nitride is more isotropic.
- The Ti-C bonds along the a-axis are weaker in Ti_3SiC_2 than in Ti_2AlC. In either case, these bonds are comparable, and maybe even slightly stronger than those in stoichiometric TiC.
- Despite the differences in structure, it is reasonable to conclude that along the c-axis the Ti-Si bonds in Ti_3SiC_2 are weaker than the Ti-Al bonds in Ti_4AlN_3; a conclusion corroborated by the XPS and structural results (Tables 2 and 3).
- On average, the bonds in Ti_2AlN are not only distinctly stronger in the a- and c-directions than those in Ti_4AlN_4, but must also be stronger than the bonds in stoichiometric TiN. The fact that the replacement of N by Al in TiN enhances the bonding, despite the fact that the number of valence electrons is reduced by two, is important because it strongly implies that some of the electrons in stoichiometric TiN are residing in anti-bonding orbitals[131]. Presumably, the replacement of the N atoms by Al reduces the number of electrons in the anti-bonding orbitals further stabilizing an already stable structure.

The reasons for all of these observations are not totally clear at this time, but must be ultimately be traceable to the intricacies of the bonding mechanisms, especially those between the Ti and Al planes. This is obviously a very fertile field of theoretical modeling and research.

Table 8: Summary of thermal expansion results determined from XRD and ND for select ternary phases. Also shown are the values for TiC and TiN.

Compound	Ti_2AlC[98]	Ti_2AlN[98]	Ti_3SiC_2[77]	$Ti_4AlN_{2.9}$[98]	TiC[149]	TiN[149]
α_a, (K)-1	7.1±0.3	8.6±0.2	8.6	9.6	7.4	9.35
α_c, (K)-1	10±0.5	7.0±0.5	9.7	8.8	7.4	9.35
Unit cell expansivity	8.1	8.1	8.9 ± 0.1	9.4 ± 0.2	7.4	9.35
Dilatometric	8.8	8.2	9.1 ± 0.2	9.7 ± 0.2		

4.5. Thermal Conductivity

The temperature dependencies of the thermal conductivities, k_{total}, of Ti_3SiC_2[77], $TiAlC_2$[104], $Ti_4AlN_{2.9}$[98] and Nb_2SnC[103] are compared in Fig. 12. The highest room temperature conductivity belongs to $TiAlC_2$; the lowest to $Ti_4AlN_{2.9}$, with Ti_3SiC_2 and Nb_2SnC in between. The thermal conductivities of $TiAlC_2$ and Ti_3SiC_2 are higher than those of Ti. The slopes of the curves also vary; they are positive for Nb_2SnC and $Ti_4AlN_{2.9}$, and negative for the other two.

In general, k_{total} is given by:

$$k_{total} = k_e + k_{ph} \tag{8}$$

where k_e and k_{ph} are the electronic and phonon contributions to k_{total}. k_e, can be estimated from the Wiedmann-Franz Law:

$$k_e = \frac{L_o T}{\rho} \tag{9}$$

where ρ is the electrical resistivity at temperature T, and L_o is the classic Lorenz number, 2.45 x 10^{-8} W•Ω/K^2. As discussed below, at temperatures greater than ≈ 70 K, ρ of the ternaries can be

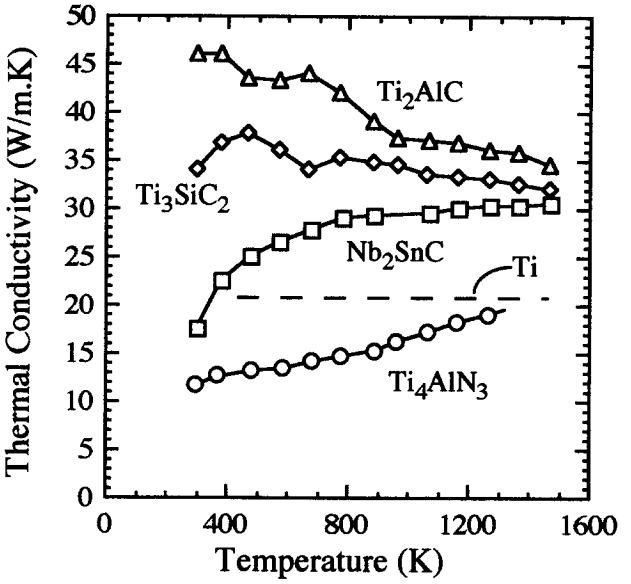

Figure 12: Effect of temperature on thermal conductivities of ternary compounds. Also included are values for pure Ti.

represented by:

$$\rho = a\,T + b \tag{10}$$

where $a > 0$, and b is the intercept at 0 K. It follows that at higher temperatures:

$$k_e = \frac{L_o T}{aT + b} \tag{11}$$

Using the electrical resistivity values and their temperature dependencies (Table 10), it is straightforward to determine the various parameters listed in Table 9. Also listed in Table 9 are the corresponding parameters for near stoichiometric TiC_x, TiN_x and NbC_x for comparison. At room temperature, the Wiedmann-Franz Law is not applicable to Nb_2SnC, nor, for that matter to NbC (see Table 9). To calculate the room temperature k_{ph} values for Nb_2SnC, it was assumed that the Wiedmann-Franz Law was applicable at the higher temperatures (which is a good assumption for the binary carbides and nitrides[150]) and that, like $Ti_4AlN_{2.9}$, the phonon contribution to k_{total} was, as a first approximation, temperature independent.

Note that if the residual resistivity at 0 K is high, i.e. $b > 0$, (e.g. $Ti_4AlN_{2.9}$ or Nb_2SnC in Fig. 13a and b, respectively), then k_e must increase with increasing temperatures and vice versa. It follows that if k_{ph} is a weak function of temperature, the slope of k_{total} with temperature would be that of k_e. This explains why k_{total} for $Ti_4AlN_{2.9}$ or Nb_2SnC increase with increasing temperatures, while for Ti_3SiC_2 for which $b \approx 0$ (Fig. 13a), it is almost temperature independent.

It is fairly well established that for the binary transition metal carbides, the phonon contribution to k_{total} is much lower than one would expect based on their elastic stiffnesses; a

discrepancy now understood to result from strong phonon-point defect interactions[152-154]. This is especially true when it is appreciated that it is difficult, if not impossible, to fabricate MC_x samples with x = 1; x in the best single and polycrystals is ≈ 0.96[147,151]. A perusal of Table 9 indicates that in general, a similar problem arises for the ternary phases; the k_{ph} are relatively low for solids of their stiffnesses. For example, k_{ph} of Ti_3SiC_2 at room temperature almost vanishes. However, since Ti_3SiC_2 is quite stiff, and believed to be a line compound with few point defects (see next section), the reason for the suppression of k_{ph} cannot be point defects, and must lie elsewhere.

The results listed in Table 9 can be understood by making the following hypothesis: Since the A-group elements are relatively weakly bound in the structure, they are most probably potent phonon scatterers. It is useful in this context to think of the A-group atoms as "rattlers", defined as atoms that vibrate about their equilibrium position more than the other atoms in the structure (Fig. 8a). The simplest expression for k_{ph} is:

$$k_{ph} = 1/3\ c_v\ v_m\ \lambda \qquad (12)$$

where c_v, v_m and λ, are respectively, the heat capacity per unit volume, the mean velocity of sound and the mean free path of the heat carrying phonons. If the rattlers are truly localized oscillators (or Einstein oscillators), it follows that λ should be the distance between the rattlers[155-156]. For Ti_3SiC_2 at room temperature, $v_m \approx 6000$ m/s (Table 12), $k_{ph} \approx 1$ W/m•K, and $c_V \approx 2.3$ J/cm^3•mol. It follows from Eq. 12 that $\lambda \approx 2.2$ Å, which is surprisingly, and probably fortuitously, very close to the Si-Si distance (≈ 3Å) in Ti_3SiC_2. Repeating the same calculations for $Ti_4AlN_{2.9}$ yields ≈ 17Å; a reasonable result since the Al atoms are better bound in the structure than the Si atom, *and* $Ti_4AlN_{2.9}$ is much more defective. For Nb_2SnC, assuming $k_{ph} \approx 5$ W/m•K λ is ≈ 14 Å. However, since 5 W/m•K must be an upper limit for k_{ph}, this result is again quite reasonable; had k_{ph} been 2 W/m•K instead, λ would be ≈ 6 Å. In the case of Ti_2AlC, the situation is less clear

Table 9: Summary of thermal conductivity (W/m•K) results for a number of ternary carbides, near-stoichiometric TiC_x[150,151], $TiN_{0.99}$[151] and NbC_x[149].

Com-pound	k_{total} W/m•K @ 300 K	1300 K	300 K k_e	300 K k_{ph}	1300 K k_e	1300 K k_{ph}
Ti_3SiC_2	34	33	33 (97%)	≈ 1 (3%)	32 (97%)	≈ 1 (3%)
Nb_2SnC	17.5	30.5	12.5‡ (72)	5‡ (28%)	25 (82%)	5 (18%)
$Ti_4AlN_{2.9}$	12	20	2.8 (23%)	9.2 (77%)	10 (50%)	10 (50%)
Ti_2AlC	46	36	20 (43%)	26 (57%)	NA	NA
TiC_x	33.5[150]	39[150]	12[150] (36%)	21.5 (64%)	24 (66%)	15 (38%)
$TiC_{0.96}$	14.4[151]	33.4[151]	7.35[151] (50%)	7.05 (50%)		
$TiN_{0.99}$	27.4[151]	45.3[151]	29.4‡‡			
NbC_x	14[149]		21[149]‡‡			

‡ To calculate this value, it was assumed that k_{ph} is not a function of temperature and equal to its value at 1300 K, where it is more likely that the classic Lorenz number is applicable.

‡‡ Since $k_e > k_{total}$, the Lorenz number must be < 2.45 x 10^{-8} W.Ω/K^2.

since $\lambda \approx 38$ Å, but here the case can be made that the Al atoms are so well bound in structure as to no longer act as "rattlers".

Evidence for strong scattering by "rattlers" *and* point defects is multifold and, referring to Table 9, includes the following observations:

- The majority of the heat in Ti_3SiC_2 and Nb_2SnC is carried by electronic defects, and the absolute value of k_{ph} is quite small ($\approx$ 1 to 5 $W \cdot m^{-1} K^{-1}$). The contribution of defects to phonon scattering in the case of Nb_2SnC cannot be discounted at this time. The residual resistivity of Nb_2SnC is relatively high (Fig. 13b) indicating a defective crystal.
- The replacement of the Si atoms in Ti_3SiC_2 by C to form TiC_x atoms *enhances* k_{ph} from ≈ 1 to at least 7 $W \cdot m^{-1} K^{-1}$.
- Replacing the Si by Al atoms to form Ti_2AlC results in a more than 20-fold increase in k_{ph}, indicating the scattering potency of the Si-atoms relative to the Al-atoms. This conclusion is believed to be valid despite the structural differences between Ti_2AlC and Ti_3SiC_2.
- The behavior of the Al-containing ternaries, especially $Ti_4AlN_{2.9}$, is similar to the MC_x binaries in that k_{total} increases with increasing temperature and is nearly equally divided between electron and phonon contributions, with the latter being nearly temperature independent[149-154] (compare TiC_x with $Ti_4AlN_{2.9}$ in Table 9). Given the confirmed presence of N vacancies in $Ti_4AlN_{2.9}$[63], it is fair to assume that they also are strong scatterers of phonons.
- Replacing the C atoms in TiC_x by Al atoms to form Ti_2AlC results in an *increase* in k_{ph}. The simplest interpretation is that the ternary has less point defects to scatter the phonons. As noted above, even in the best single or polycrystals of TiC_x the vacancy concentration ($\approx$ 4 %), is considerably larger than the one in $Ti_4AlN_{2.9}$ ($\approx$ 1.25%). Based on stoichiometry alone it is fair to assume that Ti_2AlC has even less defects.
- The phonon conductivity is greater in Ti_2AlC than in $Ti_4AlN_{2.9}$.What fraction of the phonons are scattered by vacancies, and what fraction is due to scattering by the Al atoms is unknown at this time. According to the TEC results, however, the atoms are better bound Ti_2AlC than in $Ti_4AlN_{2.9}$, which is consistent with the fact k_{ph} of the former is higher.

Clearly more work is needed to validate some of the ideas presented herein. Data for k_{total} in the 2 to 300 K temperature regime would be invaluable in shedding more light on the problem. These gaps in knowledge notwithstanding, it is fair to conclude that the thermal behavior of the $M_{N+1}AX_N$ phases depends on how strongly the A-group layers are bound in the structure: If weakly bonded, the A layers can be potent scatterers of phonons, in which case the contribution of k_{ph} to k_{total} can be drastically reduced. Furthermore, like in the binary carbides and nitrides, strong phonon-point defect scattering is operative. Finally, the main reason for the good thermal conductivities is their good electrical conductivities.

5. ELECTRICAL PROPERTIES

5.1. Electrical Conductivity

As a class, the $M_{N+1}AX_N$ phases are good electrical conductors, with room temperature resistivities, ρ_{300}, that range from 0.07 $\mu\Omega$•m to 2.7 $\mu\Omega$•m (Table 10). Like metals, the resistivities decrease linearly with decreasing temperatures (Fig. 13), and can be best described by:

$$\rho(T) = \rho_{300}[1 + \alpha(T - 300)] \qquad T > 100\ K \qquad (13)$$

where α is the temperature coefficient of resistivity. Table 10 lists the values of ρ, $d\rho/dT$ and α for a number of ternary compounds. In general, the values are comparable to those of Ti, $TiSi_2$ and Zr (Table 10).

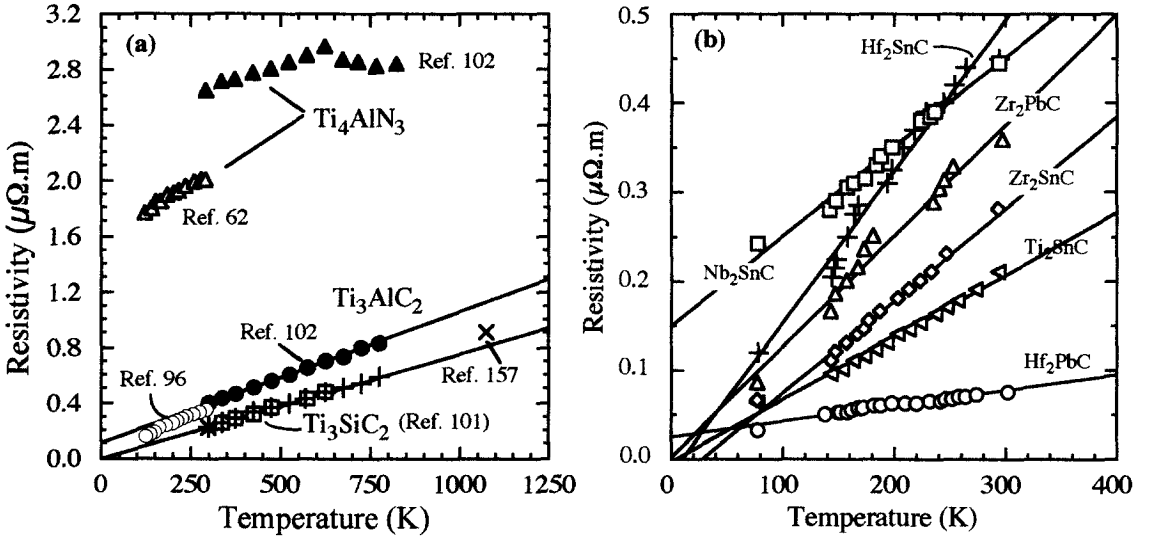

Figure 13: Effect of temperature on resistivities of; a) Ti_3SiC_2, $Ti_4AlN_{2.9}$ and $Ti_3Al_{1.1}C_{1.8}$, and; b) Sn- and Pb-containing M_2AC phases[99].

With the notable exception of $Ti_4AlN_{2.9}$, the resistivities of the Ti-containing ternaries are lower than those of Ti and TiC_x. However, the reproducibility in the results vary from compound to compound and can be separated into two groups. In the first, exemplified by Ti_3SiC_2, Hf_2SnC and Ti_2AlC, the scatter in ρ and $d\rho/dT$ is narrow (< 20%), which, in turn, is probably an indication that these phases are line compounds, i.e. exist over a narrow range of stoichiometry. This conclusion is consistent with the work of Wakelkamp et al.[46] who have shown, and we and others[46] have since confirmed, that Ti_3SiC_2 is essentially a line compound.

For the second group, encompassing most of the other compounds listed in Table 10, the scatter in ρ and $d\rho/dT$ is significant. For example, in our initial report on the Sn-containing ternaries[69], we reported the resistivity of Ti_2SnC to be 0.07 $\mu\Omega$•m. In our more recent work[99] the resistivity, at 0.22 $\mu\Omega$•m, was more than 3 times higher, for nominally identical samples, albeit

made months apart. Since these variations are too large to be attributed to experimental error in the measurements alone, their cause must lie elsewhere. The most likely variables are: i) variations in stoichiometry; ii) the presence of impurities or second phases and/or, iii) the presence of quenched-in point defects that could result from varying cooling rates. The latter

Table 10: Summary of electrical properties of ternary carbides and nitrides. Also included are the corresponding values for Ti, Zr and $TiSi_2$.

Compound	ρ_0 ($\mu\Omega$-m)	$d\rho/dT$ $\mu\Omega \cdot m \cdot K^{-1}$	α $(K)^{-1}$	Temp. Range (K)	Ref.
$Ti_3Al_{1.1}C_{1.8}$	0.387±0.007	0.00095	0.0024±0.0003	300-850	102
	0.345	0.00107	0.0031	120-300	96
$Ti_4AlN_{2.9}$	2.64±0.02	0.0009	0.00034±0.00001	300-620	102
	2.0	0.0015	0.00075	120-300	62
Ti_3SiC_2	0.227±0.003	0.00075	0.00328±0.00001	300-850	101
	0.222	0.00089	0.004	120-300	44
	0.21	0.0009	0.0043	298-1073	157
Ti_3GeC_2	0.22				65
Ti_2GeC	0.227				65
Ti_2AlC	0.36				65
	0.37				97
Ti_2AlN	0.312				65
	0.25‡				97
$Ti_2AlC_{0.5}N_{0.5}$	0.322				97
Ti_2SnC	0.222	0.00071	0.0032		99
	0.07				69
Zr_2SnC	0.28	0.00098	0.0035		99
	0.143				69
Nb_2SnC	0.4	0.00084	0.0021		99
	0.25				69
Hf_2SnC	0.45	0.00153	0.0034		99
	0.42				69
Zr_2PbC	0.36	0.0052	0.0144		99
Hf_2PbC	0.07	0.00044	0.0063		99
$TiSi_2$	0.13	≈ 0.0005	≈ 0.0038	77-300	158
Zr	0.4	0.00176	0.0044		159
Ti	0.465	0.0021	0.0045	77-300	160
	0.492	0.002	0.0041	4-300	159
	0.40	0.0017	0.00425	300-1100	161

‡ Sample was not single phase.

were not controlled, but in general were quite slow. Furthermore, in these metallic-like conductor, especially the ones with high $N(E_F)$'s, the concentration of impurities would have to be quite high to significantly affect the resistivities. It is important to note that the same wide variations in ρ and dρ/dT are characteristic of the binary transition metal carbides and nitrides[153], in which case much of the variation has been traced back to variations in vacancy concentrations. It is thus reasonable to conclude that in the ternaries, the scatter is also due to the creation of vacancies, possibly as a result of non-stoichiometry. This is especially true given the efficacy of vacancies in scattering both phonons and electrons in $Ti_4AlN_{2.9}$ (see section 5.3). These conclusions notwithstanding, clearly much more work systematic work, as a function of stoichiometry, cooling rates, etc., is needed in order to better understand the nature of electrical transport in these ternary compounds.

5.2. Hall and Seebeck Coefficient Measurements

The room temperature Hall coefficient, R, values for Ti_3SiC_2, $Ti_4AlN_{2.9}$ and $Ti_3Al_{1.1}C_{1.8}$ are summarized in Table 11[102]. For $Ti_3Al_{1.1}C_{1.8}$ and $Ti_4AlN_{2.9}$, R is positive indicating that the majority carriers are electron holes. The situation for Ti_3SiC_2 is more ambiguous. In one set of experiments, R was measured for 4 samples; three gave negative values and one a positive value. In another set of measurements the Hall voltage was below the detectability limit of our instrument. These result, strongly suggest, and the Seebeck measurements confirm[101], that Ti_3SiC_2 is a mixed conductor. At 298K, both positive and negative values of R have been reported for Ti as well[159,161]. In all cases for TiC_x, at room temperature, R is negative[147,162,164,165]. With increasing temperatures, R drops, reaches a minimum at ≈ 1000 K[165]. This behavior was interpreted as indicating the appearance of hole conductivity.

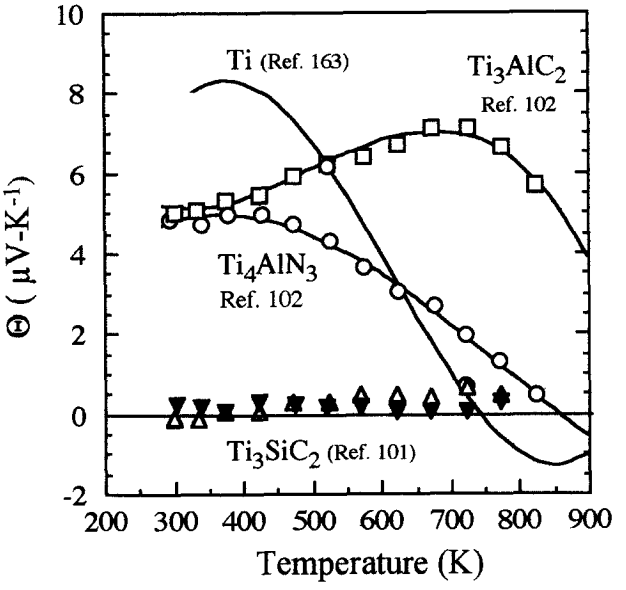

Figure 14: Effect of temperature on Seebeck coefficients of Ti_3SiC_2[101], $Ti_4AlN_{2.9}$[102] and $Ti_4AlN_{2.9}$[102]. Also included are the results for Ti[163].

The temperature dependence of the Seebeck coefficients, Θ, of Ti_3SiC_2[101] $Ti_3Al_{1.1}C_{1.8}$[102] and $Ti_4AlN_{2.9}$[102] are shown in Fig. 14. These results confirm that at room temperature $Ti_3Al_{1.1}C_{1.8}$ and $Ti_4AlN_{2.9}$ are indeed hole conductors, with the contribution of electrons becoming more important at higher temperatures. The thermoelectric response of Ti_3SiC_2, on the other hand, is unique; Θ is essentially temperature independent over, at least, the 300 to 850 K temperature range[101]. The simplest interpretation of these results is to assume that: i) concentrations of the free electrons, n, and electron holes, p, are and equal, and, ii) their respective mobilities are also equal, i.e. $\mu_e = \mu_p$. As discussed in the next section this is a key assumption made to decipher the details of the conduction mechanisms in Ti_3SiC_2.

5.3. Conduction Mechanisms

In principle, and assuming a single carrier model for the conductivity, it is possible to infer the concentration and charge of the majority electronic species from a knowledge of R and σ. With two carriers the situation is more complicated and the appropriate equations are:

$$\sigma = e\,(n\,\mu_e + p\,\mu_p) \tag{14}$$

$$R = \frac{p - n(\mu_e/\mu_h)^2}{e\,(p + n(\mu_e/\mu_h)^2} \tag{15}$$

where μ_e, μ_h and e are, respectively, and electron and hole mobilities and the electronic charge. For $Ti_3Al_{1.1}C_{1.8}$ and $Ti_4AlN_{2.9}$, p >> n, and Eqs. 14 and 15 simplify to, $\sigma = ep\mu_p$ and R = 1/ep, respectively. Thus, p and μ_p are readily calculated (Table 11).

When the R-values are sensitive to small variations in defect structure and/or small deviations in chemistry, as in the case for Ti_3SiC_2 or Ti (i.e. when the system is in a mixed n/p regime) R cannot be used to accurately estimate the number of carriers. To solve for the latter, two assumptions are made[102]. First, and in analogy to the free electron model, n is assumed to be proportional to the cube of $N(E_F)$ expressed on a per unit volume basis. The second assumption is the one reached in the previous section, viz., n = p and $\mu_e = \mu_p$. The last step is to compare the conductivities of Ti_3SiC_2 with the other two. The details can be found elsewhere[102]; the results are listed in Table 11.

Based on these results, it follows that Ti_3SiC_2 is the most conductive because both n and p are high and both contribute to the conductivity. The slightly lower mobility of the carriers in Ti_3SiC_2 relative to $Ti_3Al_{1.1}C_{1.8}$ is probably due to an enhanced scattering of electrons by the Si atoms relative to the Al atoms. In $Ti_3Al_{1.1}C_{1.8}$, the conductivity is depressed because the number of charge carriers is low. A conclusion corroborated by theoretical calculations[135] (Fig. 6b) and experimentally verified[88], that show that E_F in $Ti_3Al_{1.1}C_{1.8}$ falls in a local minimum in the total DOS[88]. In contradistinction, E_F for Ti_3SiC_2 occurs near a local maximum (Fig. 6). Lastly, $Ti_4AlN_{2.9}$ is the least conductive, not because of a lack of carriers - its DOS at E_F is higher than either Ti_3SiC_2 or $Ti_3Al_{1.1}C_{1.8}$[88] - but because the mobility of those carriers is low, presumably due to scattering by the vacancies known to exist in that structure[63]. It is fairly well established that vacancies in non-stoichiometric transition metal carbides and nitrides are potent scatterers of electrons[153]. Comparing

Table 11: Summary of electrical transport parameters calculated from room temperature conductivity and Hall measurements[102]. Also included are the results for TiC_x.

	R x 10^{11} m^3/C	σ_{300} $(M\Omega \cdot m)^{-1}$	μ_p x 10^5 $m^2 \cdot V^{-1} \cdot s^{-1}$	μ_n x 10^5 $m^2 \cdot V^{-1} \cdot s^{-1}$	p x 10^{28} (m^{-3})	n x 10^{28} (m^{-3})	Refs.
Ti_3SiC_2	± 0	4.5	≈ 6‡	≈ 6‡	24	24	102
			10‡‡	10‡‡	14	14	102
$Ti_3Al_{1.1}C_{1.8}$	7±1	2.75±0.2	≈ 19 ± 0.3		9±1		102
$Ti_4AlN_{2.9}$	3.5±1	0.23±0.5	0.8 ± 0.3		18±5		102
$TiC_{0.928}$	- 155	0.57		89.6		0.4	162
$TiC_{0.939}$	- 150	0.613		92		0.42	162
$TiC_{0.969}$	- 166	0.735		122		0.38	162
$TiC_{>0.969}$	- 150	1.05		158		0.4	162
$TiC_{0.95}$	- 261	0.645		168		0.24	147
$TiC_{0.92}$	- 167	0.58		97		0.37	147

‡ Calculated using $Ti_3Al_{1.1}C_{1.8}$ data. ‡‡ Calculated using $Ti_4AlN_{2.9}$ data. (see Ref. 102 for details).

our results for the ternaries with those for TiC_x (Table 11) leads further credence to our conclusions. TiC_x is not very conductive because of a dearth of carriers. The mobility is, however, quite high presumably because of a lack of "rattlers".

6. ELASTIC PROPERTIES

In general, the $M_{N+1}AX_N$ phases are elastically quite stiff. This is particularly true for the ternaries for which N >1. The room temperature Young's moduli, E_{RT}, are ≥ 300 GPa (Table 12). Similarly, the shear, μ_{RT} and bulk moduli are in the 120 and 200 GPa range, respectively (Table 12). Poisson's ratio for all compounds is ≈ 0.2, which is lower than that of pure Ti (0.3), and more in line with stoichiometric TiC (≈ 0.19). Not surprisingly, given the larger fraction of M-X bonds in the 312's and 413 as compared to the 211's, the latter are less stiff. For example, at ≈ 200 GPa the Young's modulus of Ti_2AlC is significantly lower than that of Ti_3AlC_2 at ≈ 300 GPa. The Young's moduli of Zr_2SnC, Nb_2SnC and Hf_2SnC, at 178, 216 and 237 GPa, respectively, are also lower[99].

Like most solids, above a certain temperature (≈ 100 K), the Young's, E, and shear, μ, moduli decrease linearly with increasing temperatures according to:

$$\mu/\mu_{RT} = 1 - \omega_\mu (T - 298) \qquad T > 125\ K \qquad (16)$$

and

$$E/E_{RT} = 1 - \omega_E (T - 298) \qquad T > 125\ K \qquad (17)$$

where ω_i is the temperature dependence of the appropriate modulus. These values are listed in Table 12.

The mean velocity, v_m, of sound in a solid is defined as:

$$v_m = \left[\frac{3}{2v_l^3 + v_s^3}(v_s v_l)^3\right]^{1/3} \qquad (18)$$

where v_l and v_s are the longitudinal and shear velocities, respectively. Knowing v_m the Debye temperature, θ_D, can be estimated from:

$$\theta_D = \left(\frac{h}{k_B}\right)\left(\frac{3\,\xi\,\delta\,N_{Av}}{4\,\pi\,m}\right)^{1/3} v_m \qquad (19)$$

where δ and m are the density and molecular weight, respectively. Knowing v_m,, θ_D can be calculated and the results are tabulated in Table 6 (column 8). In general, these values are in good agreement with the θ_D values calculated by other methods, which gives credence to all the results. As noted above these Debye temperatures are quite high and more in line with stiff ceramics such as Al_2O_3 and Si_3N_4 than with metals.

The densities of the $Ti_{N+1}AlX_N$ ternaries are comparable to Ti metal, but are at least twice as stiff, and maintain their high stiffnesses to high temperatures. For example, at 1273 K the shear modulus of $Ti_3Al_{1.1}C_{1.8}$ is $\approx$ 88 % of its room temperature value. Elastically, Ti_3SiC_2, Ti_3AlC_2 and $Ti_4AlN_{2.9}$ are comparable to Mo, a metal prized for its stiffness and excellent high temperature properties, but not its low density or machinability. The range of stiffnesses for these compounds are also comparable to those of hot pressed Si_3N_4 and Al_2O_3.

Table 12: Summary of sound velocities and moduli of Ti_3SiC_2, $Ti_4AlN_{2.9}$, and $Ti_3Al_{1.1}C_{1.8}$. Unless otherwise noted, all the data are taken from Ref. 91. The data for $TiC_{0.96}$, Mo and Si_3N_4 are also included.

	v_l (m/s)	v_s (m/s)	Density	Young's Mod. (GPa)	Shear Mod. (GPa)	Bulk Mod. (GPa)	Poissons Ratio	ω_E (K^{-1}) x 10^4 (T > 125 K)	ω_μ (K^{-1}) x 10^4 (T > 125 K)
Ti_3SiC_2	9100[a] 9142[b]	5570[a] 5613[b]	4.4 4.5[8]	333[a] 339[b]	139[a] 142[b]	185[a] 187[b] 206[166]	0.20 0.20 0.20	- 0.88[a] - 0.75[b] - 0.95[83]	- 1.4[a,b] - 1.4
Ti_4AlN_3	8685	5201	4.7	310	127	185	0.22	- 0.74	- 1.5
Ti_3AlC_2	8880	5440	4.2	297.5	124	165	0.20	- 0.84	- 1.2
$TiC_{0.96}$			4.93	491	205	272	0.2		- 0.54
Mo			10.2	318	122	267			- 1.46
Si_3N_4			3.2	320	126	232			

a: 3-5 μm grains; b: 100-300 μm grains.

The Raman spectroscopy of these compounds supplies yet another clue to their properties, especially their mechanical response discussed in the next section. By comparing the Raman spectra of Ti_3SiC_2 with those of $TiC_{0.67}$, we confirmed the presence of a soft mode at 150 cm^{-1} (Fig. 15)[75]. This mode was assigned to a shear mode between the Ti and Si layers; not unlike the ones observed between layers in graphite. The corresponding shear modes for Ti_2AlN and $Ti_4AlN_{2.9}$ are located at 135 cm^{-1} and 153 cm^{-1}, respectively[111].

The results of Onodera et al,[166] who carried out synchrotron x-ray diffraction measurements on Ti_3SiC_2 under pressures up to 61 GPa at room temperature are also noteworthy. Their bulk

modulus is roughly 9 % higher than the ones measured by ultrasound (Table 12). Interestingly enough and in total agreement with the TEC results, they found that the decrease with pressure of the c-axis length is faster than that of the a-axis length implying that the Ti-Si bonds, along the c-axis are weaker than the Ti-C bonds along the a-axis.

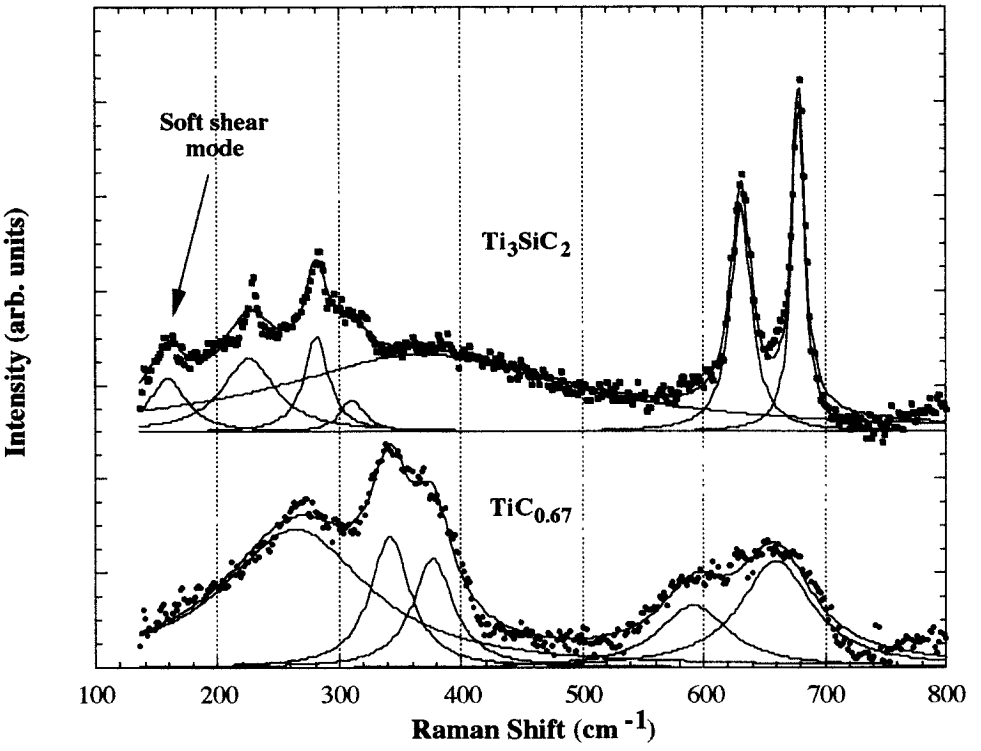

Figure 15: Experimental data and curve fitting of Raman spectra for Ti_3SiC_2 and $TiC_{0.67}$[75]

7. MECHANICAL PROPERTIES

It is in their mechanical response that the uniqueness of the $M_{N+1}AX_N$ phases ternaries is most apparent. At the very onset of our work, we had compelling evidence demonstrating their nanolaminate nature. Micrographs such as the ones shown in Fig. 16 were routinely observed on fractured surfaces and near areas of intense plastic deformation[44,65,66,76,86]. Because the vast majority of our work has been on Ti_3SiC_2, the discussion in this section will deal mostly with that compound. The conclusions reached, however, are of general validity for all the $M_{N+1}AX_N$ phases tested to date.

Like most materials, the mechanical properties of Ti_3SiC_2 depend on grain size. In the coming sections reference will be made to two microstructures[44], fine-grained (Fig. 17a) and coarse-grained (Fig. 17b), henceforth referred to, respectively, as FG and CG.

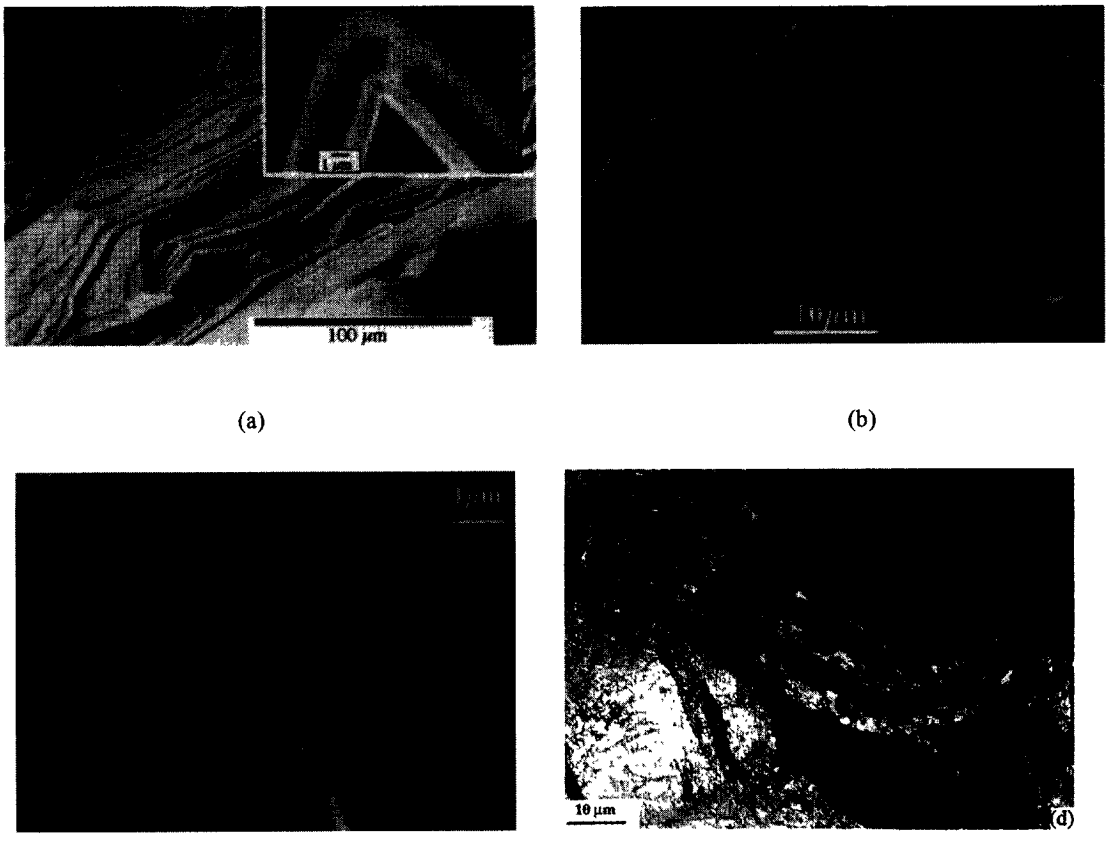

(a) (b)

(c) (d)

Figure 16: a) SEM micrograph of a typical fractured surface in Ti_3SiC_2. Inset shows a higher magnification SEM micrograph of prominent feature labeled "A" showing very sharp radii of curvatures possible. b) Morphology of Ti_3SiC_2 surface after scribing with a sharp object. c) Example of nested layers. d) Polished and etched optical micrograph of a grain deformed at room temperature showing extraordinary extent by which a single grain can bend, curl and fold on itself.

7.1 Compressive and Tensile Properties

Typical stress-strain curves for Ti_3SiC_2 deformed under compression loading at various temperatures are shown in Fig. 18a[86]. Unless otherwise noted, the data shown in Fig. 18a are for the FG microstructure. At room temperature, and using a strain rate of 5×10^{-3} s^{-1}, the failure is brittle. The failure stress is a function of grain size: the FG material fails at $\approx$ 1 GPa; the CG at $\approx$ 700 MPa. At 1200 °C, there is a distinct non-linearity in the stress-strain curves, that is followed by a region of apparent "strain hardening". At 1300 °C, the stress-strain response, in compression exhibits three stages, labeled, respectively, A, B and C (Fig. 18a, inset): (a) an elastic regime, (b) an inelastic deformation stage, or apparent "hardening" regime, and, (c) a distinct softening until failure. At higher temperatures the extent of the softening regime is significantly larger than the "hardening" regime. The strains to failure are in excess of 15 %.

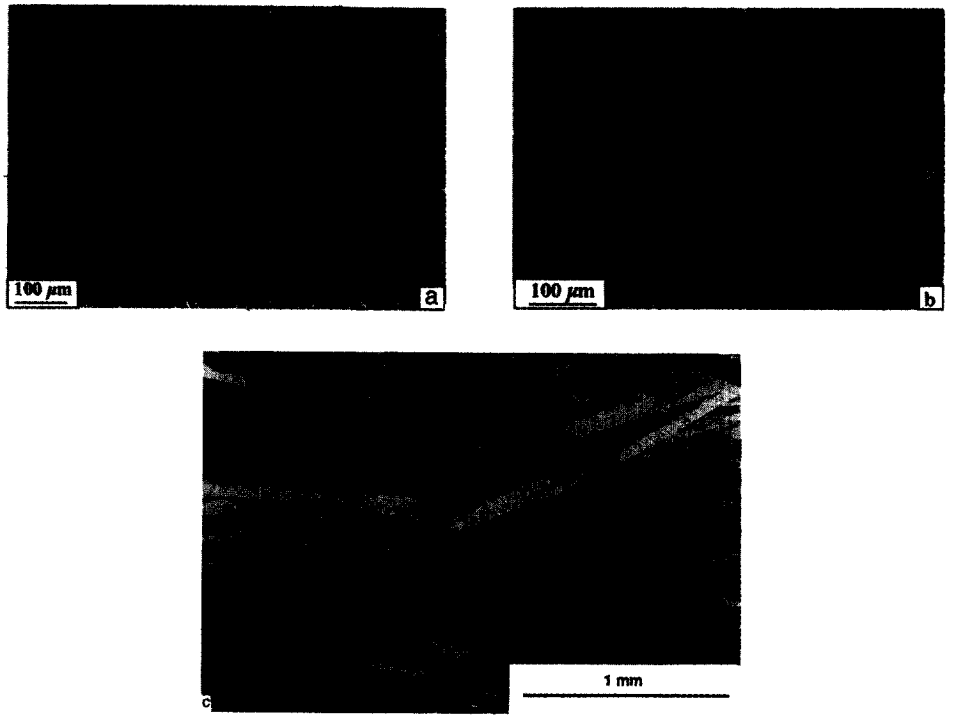

Figure 17: Polished and etched optical micrographs of: a) fine, b) coarse and, c) highly oriented macro-grained samples of Ti_3SiC_2.

Because the transition between the elastic and inelastic deformation regions is *not* a yield point (see below), the stress at which this transition occurs will henceforth be referred to as the inelastic deformation stress or **IDS**. A plot of IDS versus temperature during compression is shown in Fig. 18b, from which it is clear that significant softening occurs at temperatures above 1100 °C. The latter can thus be considered a plastic-to-brittle transition temperature, and will henceforth referred to as PBTT.

The temperature dependence of the tensile response of FG samples[94] (Fig. 18c), tested at a strain rate of 1.4 x 10^{-4} s^{-1}, is similar to that under compression, in the sense that three regions (inset in Fig. 18c) are present and considerable softening at temperatures above 1100 °C is observed (Fig. 18b, lower curve). The strains to failure depend on temperature but at 1200 °C, and using a strain of rate of 4 x 10^{-4} s^{-1}, they exceed 5%. The response shown in Fig. 18c suggested a strong strain-rate sensitivity, which was verified as shown in Fig. 18d, where it is clear that the shape of the curves and the IDS's are strong functions of strain rate. The strain-rate sensitivity, $\approx$ 0.5, is quite high and is more characteristic of super-plastic solids than it is of typical metals or ceramics[167-171]. This does *not* imply, however, that the deformation in Ti_3SiC_2 is similar to deformation in super-plastic ceramics; i.e. that the microstructure remains self-similar. As discussed below, the strain in Ti_3SiC_2 is mostly due to the formation of cavities and cracks.

Before proceeding much further it is important to review the evidence for why the IDS is *not* a yield point, (i.e. implies the presence at least five independent slip-systems). Had the IDS been a yield point it would be difficult, if not impossible, to explain the following observations:

• the large asymmetries in the IDS under compression and tension (Fig. 18b) at all temperatures, but especially at the higher temperatures. Such an asymmetry would not exist had the IDS been a true yield point.

• the extremely high "hardening" rates observed after the IDS. This is especially clear in the compression test at 1200 °C (Fig. 18a), where the stress increases from ≈ 550 MPa to ≈ 850 MPa over a strain increment of about 0.05. Such exceedingly high hardening rates have never been reported, even for ductile metals, and especially at such high temperatures. The alternate explanation must be that region B is a region of inelastic deformation in which damage is initiated but, for reasons elaborated on in the next section, does not lead to catastrophic failure.

• The high dependence of the IDS point *and* the shape of the stress-strain curves on strain rate (Fig. 18d). Here again, it would be unlikely for a solid with 5 independent slip systems to exhibit such a strong dependence. The effect of strain rate is so crucial that it is possible to obtain some plasticity (1-2 %) before failure in polycrystalline samples tested at room temperature[62,96,97,172] (Fig. 19a). This plasticity is due to the formation of shear bands typically oriented at ≈ 45 ° (i.e. along planes of maximal shear) to the loading direction (Fig. 19b). The shear bands have a high volume fraction of voids and cavities that are bridged by ligaments comprised of grains that have been severely deformed, delaminated and/or kinked (Fig. 19c). This propensity for shear band formation is common in these phases (see below).

• Finally it is important to note that despite vast differences in their physical, electrical, thermal and chemical properties, Ti_3SiC_2 and ice behave almost identically when their mechanical properties are compared[177]. This rather surprising result stems from the fact that both are crystalline solids that are plastically very anisotropic; deformation occurs overwhelmingly, if not exclusively, by slip along the basal planes. This anisotropy in turn is why the response of both solids is so strain rate sensitive; if loaded rapidly, both are brittle, but if loaded slowly they are quite plastic (Fig. 18d). In both cases, microcracks and their linkage play a dominant role in their brittle response.

These conclusions are also in accord with our transmission electron microscopy, TEM, observations; to date no evidence exists for the presence of slip systems other than basal.

7.2 Hardness and Damage Tolerance

Relative to the MX phases, the $M_{N+1}AX_N$ phases are relatively soft and the hardness is quite anisotropic. This was first documented by Nickl et al.[25], who working with small single crystals prepared by CVD, reported Knoop hardness values normal and parallel to the basal planes of 12-15 and 3-4 GPa, respectively. Much later, Pampuch et al.[33], using hot pressed samples that contained some ≈ 15 vol. % TiC, reported a Vickers hardness, H_v, of about 6 GPa, the latter in agreement with Goto and Hirai's value on CVD samples[26]. Both groups also showed that the Vickers microhardness was a function of indentation load. Pampuch et al. were also the first to note that the hardness to modulus ratio, H_V/E, was more comparable to that of ductile metals than typical ceramics.

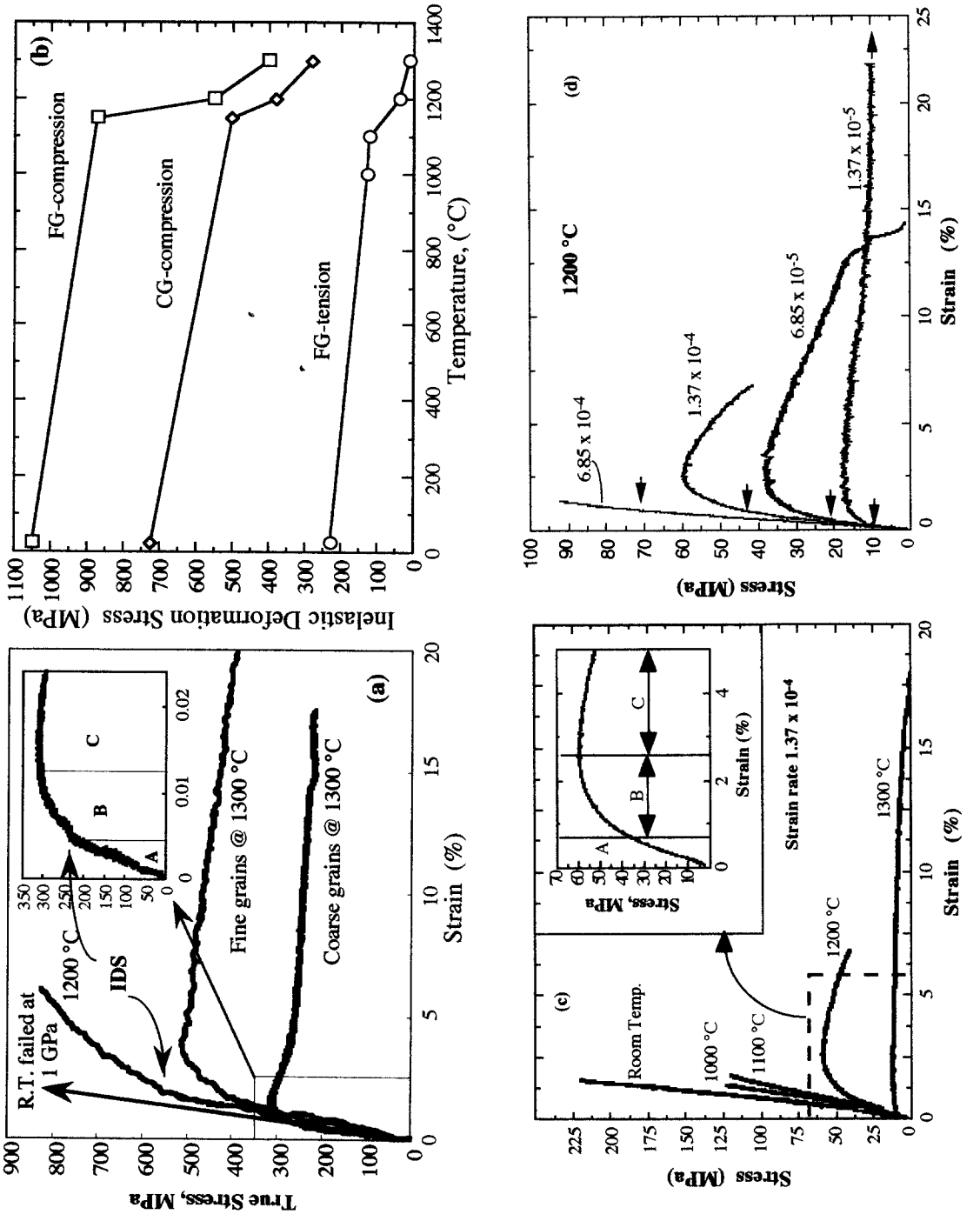

Figure 18: a) Stress-strain curves as a function of temperature and grain size in, a) compression. Unless otherwise noted the curves are for the fine-grained microstructure[86]. (Inset shows three regimes (see text). b) Effect of grain size and temperature on compressive and tensile strengths of Ti_3SiC_2. c) Effect of temperature on tensile stress-strain curves of FG Ti_3SiC_2[94]. d) Effect of strain rate on shape of tensile stress-strain curves of FG samples of Ti_3SiC_2 at 1200 °C[94].

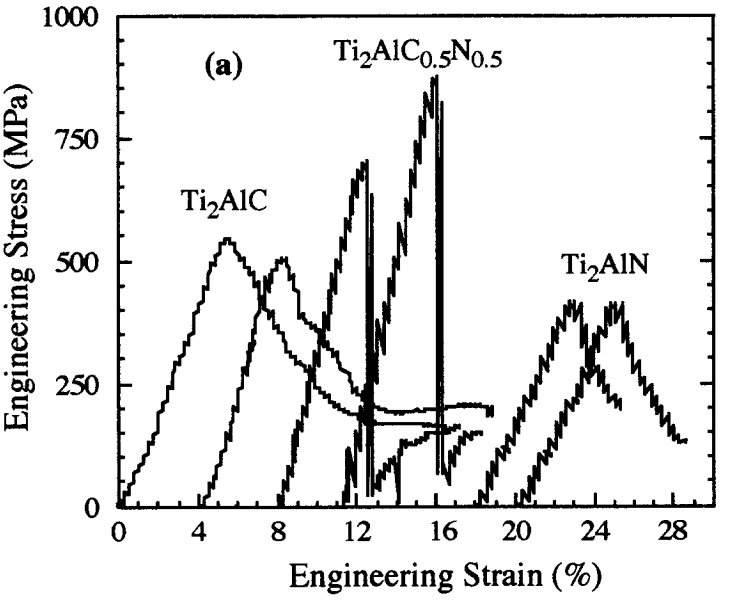

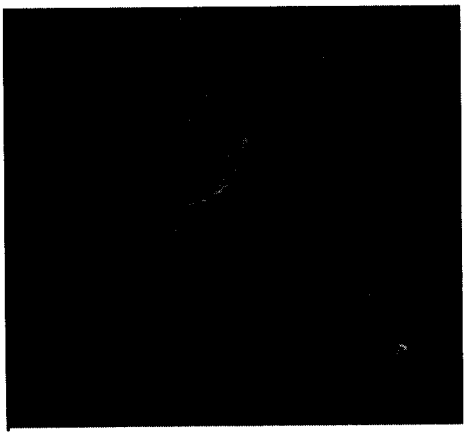

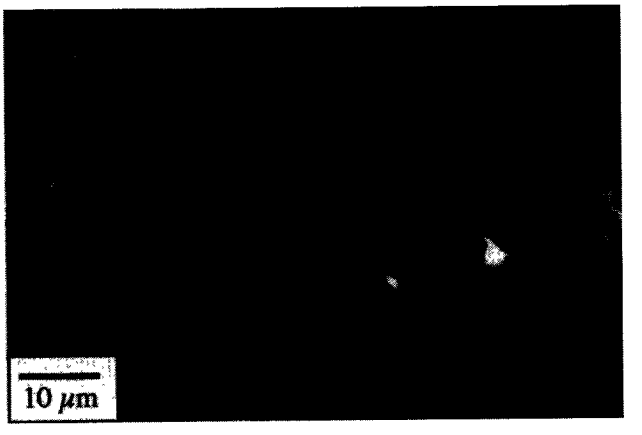

(b) (c)

Figure 19: a) Room temperature engineering stress-strain curves in compression for $Ti_2AlN_{0.5}C_{0.5}$ (middle curves), Ti_2AlN (right) and Ti_2AlC (left). Curves are shifted to the right for clarity. Note graceful nature of failure[97]. b) Low magnification SEM micrograph of $Ti_3Al_{1.1}C_{1.8}$ sample compressed at room temperature showing shear band[96]; c) higher magnification micrograph showing extent of damage to grains in shear band

The hardness values of all the ternary phases synthesized fall in the narrow range of 2-5 GPa. The highest value, 5.5 GPa, was measured on $Ti_2AlC_{0.5}N_{0.5}$[97]. In some cases, the hardness is a function of applied load (e.g. Fig. 20, top curve), in others it is not.

Polycrystalline ceramics at room temperature are brittle. The implications of this simple statement are far reaching because it renders them difficult to machine, prone to thermal shock, and sensitive to minute defects that can be introduced during processing and/or service. It would be fair to say that but for their brittleness, ceramics would have found their way into many more

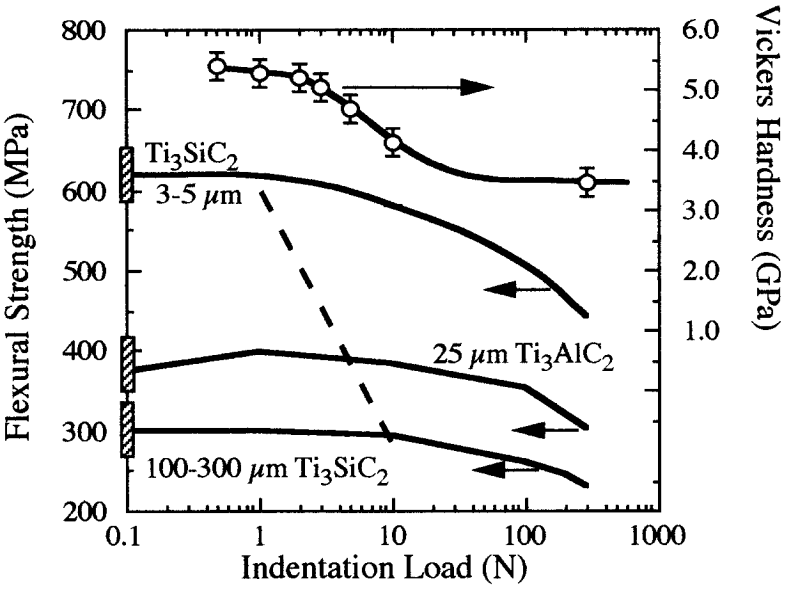

Figure 20: Vickers hardness versus indentation load of $Ti_3Al_{1.1}C_{1.8}$ (top curve, right axes); four-point flexural strength (left axis) vs. indentation loads for 25 μm $Ti_3Al_{1.1}C_{1.8}$ samples[96] and Ti_3SiC_2 for grain sizes indicated[86]. The inclined dashed line is expected behavior for brittle solids[176].

structural applications. Therefore, the importance of the remarkable damage tolerance[62,66,71,86,96,173-175] exhibited by the $M_{N+1}AX_N$ phases cannot be overemphasized. The damage tolerances of Ti_3SiC_2[66,86,175] and $Ti_3Al_{1.1}C_{1.8}$[96] are best exemplified in Fig. 20, in which the functional dependence of post-indentation bend strengths are plotted versus the Vickers indentation loads. The plot shown in Fig. 20 is not a log-log plot - which is the standard way of plotting such data[176] - but rather a semi-log plot. (The expected behavior of a perfectly brittle material is shown as a dashed line in Fig. 20). The hatched areas on the left represents the flexural strengths that result from naturally occurring flaws. Clearly, and at least for $Ti_3Al_{1.1}C_{1.8}$, the post-indentation flexural strengths are almost independent of indentation loads. This is especially true when it is appreciated that, because of its relatively low hardness (top curve in Fig. 20) a 300 N indentation load translates to a defect size of ≈ 0.4 mm. Such a defect spans ≈ 20 % of the sample's width and ≈ 27 % of its thickness and is roughly equal to the ≈ 25 % reduction in flexural strength (375 to 300 MPa). In other words, the reduction in strength is of the same order of magnitude as the reduction in cross-sectional area. Similarly, a 100 N indentation reduces the retained strength by only ≈ 7 %.

The same is true for Ti_3SiC_2, for which the retained flexural strengths are plotted for the two grain sizes indicated in Fig. 20[86]. Because the natural flaws in brittle solids typically scale with the inverse of the grain size, the reduction in strength for the FG material is slightly more severe than the CG (Fig. 20) Ti_3SiC_2[86].

Vickers indentations in most brittle solids result in the formation of sharp cracks that typically emanate from the corners of the indent. These cracks greatly magnify the effect of the indentations and result in sharp reductions in strength as a function of flaw or indentation size. It is quite difficult, if not impossible, to induce cracks from the corners of Vickers indentations in

is quite difficult, if not impossible, to induce cracks from the corners of Vickers indentations in the $M_{N+1}AX_N$ phases[35,62,66,96,97]. The main reason therefore for the damage tolerance characteristic of these solids is their ability to contain and confine the extent of damage to a small area around the indentation. Some of microstructural features observed around indentations in Ti_3SiC_2 are shown in Fig. 21a-d[66]. From these micrographs and others (not shown) the following energy-absorbing mechanisms have been clearly identified: diffuse microcracking, delamination and crack deflection (Fig. 21a), grain push-out and pull-out (Fig. 21b), and the buckling of individual grains (Fig. 21c). The micrographs shown in Fig. 21 were the first indication of the nanolaminate nature of these solids[66].

The evolution of deformation–microfracture damage below Hertzian contacts in a CG Ti_3SiC_2 was also studied[71,174]. The Hertzian indentation stress–strain response deviates strongly from linearity beyond a well-defined maximum, with pronounced strain–softening, indicating exceptional deformability in an otherwise elastically stiff solid. Surface and subsurface ceramographic observations reveal extensive quasi-plastic microdamage zones at the contact sites. These damage zones are made up of multiple intragrain slip and intergrain shear failures, with attendant microfracture at high strains. No ring cracks or other macroscopic cracks are observed on, or below the indented surfaces as is typical of most other brittle solids. The results

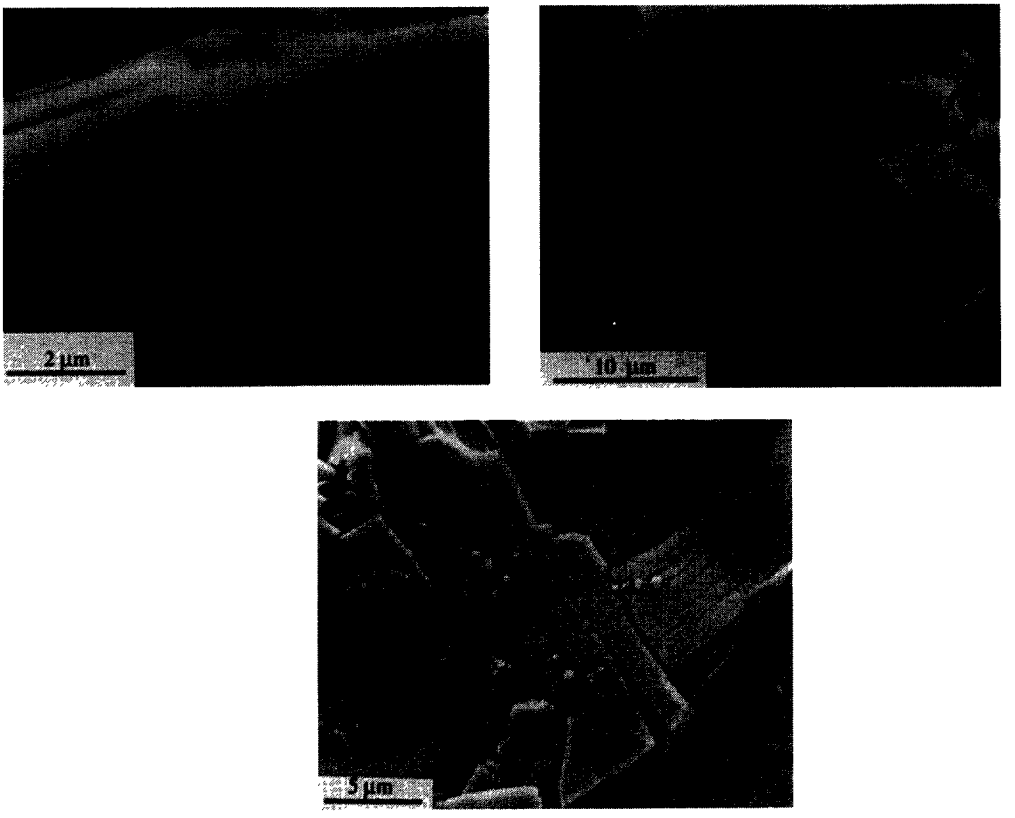

Figure 21: Microstructural features associated with indentation damage[66]; a) laminate fracture, b) grain pullout and, c) grain buckling.

suggest that Ti_3SiC_2 may be ideally suited to contact applications where high strains and energy absorption prior to failure is required. The results also suggest that Ti_3SiC_2 may be susceptible to fatigue. As discussed below, however, such fears are unfounded.

7.3. Thermal Shock Resistance

As noted above one of the more detrimental consequences of brittleness is susceptibility to thermal shock. Most brittle solids can only be subjected to a limited thermal shock, or quench, before they shatter or their strengths drop dramatically. Metals on the, other hand, are not susceptible to thermal shock because they can dissipate the thermal stresses by plastic deformation. The response of Ti_3SiC_2[43,86,175], Ti_4AlN_2[62] and $Ti_3Al_{1.1}C_{1.8}$[96] to thermal shock is unique (Fig. 22) - the behavior is neither a step function (as in ceramics) nor a horizontal line (as in metals). Instead the response is a function of grain size. Quenching the CG Ti_3SiC_2 samples from 1400 °C into ambient temperature water, not only does *not* affect their post-quench flexural

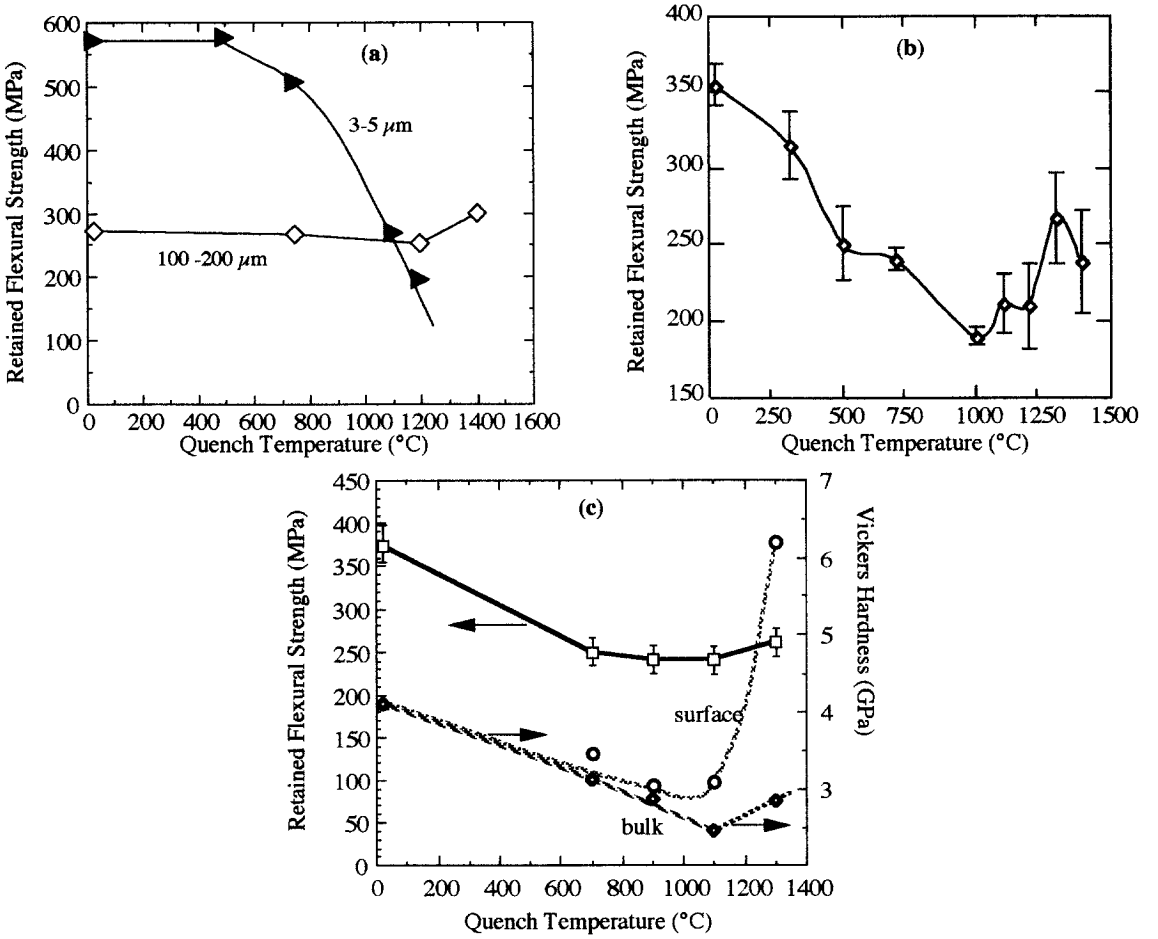

Figure 22: Retained flexural strengths versus quench temperature for: a) FG and CG Ti_3SiC_2. b) for ≈ 20 μm Ti_4AlN_2[62] and, c) ≈ 20 μm, $Ti_3Al_{1.1}C_{1.8}$ top curve (left axis). Vickers microhardness values of surface (cross-hatched line, right axis) and bulk hardness values (dashed line, right axis)[96].

strengths, but actually increases them slightly (Fig. 22a, lower line). This effect is not an artifact of the experiment, but is observed in $Ti_4AlN_{2.9}$ (Fig. 22b), and to a lesser extent in $Ti_3Al_{1.1}C_{1.8}$ (Fig. 22c). The flexural strengths of the post-quench FG Ti_3SiC_2 samples, on the other hand, decrease by $\approx$ 10% and $\approx$ 50% after ΔT quenches of 750 °C and 1000 °C, respectively (Fig. 22a, top curve).

The responses of $Ti_4AlN_{2.9}$ (Fig. 22b) and $Ti_3Al_{1.1}C_{1.8}$ (Fig. 22c), with grain sizes ($\approx$ 25 μm) intermediate between the FG and CG of Ti_3SiC_2, are also unique in that their post- quenched flexural strengths go through a minimum at a ΔT of $\approx$ 1000 °C. Furthermore, the reduction in strength ($\approx$ 40%) is not catastrophic. Post-quench surface hardness measurements of the $Ti_3Al_{1.1}C_{1.8}$ bars show that the surface hardness (Fig. 22c, center curve), similar to the post-quench bend strengths, goes through a minimum[96]. This enhancement in hardness is only skin-deep, however; the hardness of the sub-surface layers (Fig. 22c, lowest curve) do not rise as dramatically as the surface layers. Since the XRD spectra of the quenched samples did not detect the formation of any ancillary phases, apart from a very thin oxide layer that was carefully removed before testing, the simplest explanation is that a compressive layer forms on the surfaces of these ternaries as a result of quenching. How that occurs is not clear at this time and more work is needed to understand this intriguing phenomenon.

7.4 Fatigue and R-Curve Behavior

The cyclic-fatigue crack growth rates, da/dN, are plotted as a function of the applied stress-intensity range, ΔK, for the FG Ti_3SiC_2 samples in Fig. 23[95]. Also included are the results for other metals and ceramics all tested under the same conditions as Ti_3SiC_2 ($R = K_{min}/K_{max} = 0.1$ and $\nu = 25$ Hz in room air). The high dependence of da/dN, on ΔK is typical of ceramics. The fatigue threshold, ΔK_{TH}, for the CG samples, ~ 9 MPa$\sqrt{m}$, is one of the highest fatigue thresholds ever observed in a monolithic, non-transforming ceramic. For the FG samples, the fatigue threshold drops to ~6.5 MPa$\sqrt{m}$.

Field emission SEM images of fatigue damage behind the crack tip of CG Ti_3SiC_2 specimen (not shown) revealed profuse amounts of wear debris along contacting surfaces. Significant bending, basal plane delaminations and shear faulting in individual grains have also been observed[95]. These mechanisms probably reduce the severity of frictional damage in these microstructures and help to account for the very high fatigue thresholds.

Both the FG and CG microstructures exhibited substantial rising R-curve behavior[95] (Fig. 24a). The FG samples initiated at $\approx$ 8 MPa$\sqrt{m}$, rising to $\approx$ 9.5 MPa$\sqrt{m}$ after $\approx$1.5 mm of crack extension. The CG samples exhibited substantially stronger R-curve properties than the FG samples (Fig. 24a). The first specimen initiated at $\approx$ 8.5 MPa$\sqrt{m}$, and crack-growth resistance rose to $\approx$14 MPa$\sqrt{m}$, after $\approx$ 4 mm of crack extension; the second specimen initiated at $\approx$ 11 MPa$\sqrt{m}$ and grew up to ~16 MPa$\sqrt{m}$ after ~2.7 mm of crack extension. Note that for each R-curve, the initial crack length is indicated, and it appears that the initial flaw size affects the initiation toughness; a result that is most likely due to residual bridging in the pre-crack.

Evidence for both elastic-ligament bridging and frictional pullout were found and such bridging processes are similar to those observed in well-studied ceramic systems like Al_2O_3, Si_3N_4 and SiC. However, other more surprising bridging phenomena are observed such as the heavily deformed lamellae seen to bridge the crack (Fig. 24b). These bridges occur with significant amounts of delamination and bending. These ligaments are further examples of the extent by which individual grains of Ti_3SiC_2 can deform [see below]. Such processes are highly unusual and unique to these ternary systems, and must at least partially, account for the high plateau fracture toughness levels observed. Furthermore, and unlike most monolithic ceramics which exhibit bridging zones that commonly extend <1.5 mm behind the crack tip under quasi-static loading conditions, Ti_3SiC_2, shows more extensive bridging zones having lengths of over 5 mm in the CG microstructure. This suggests that the bridges in Ti_3SiC_2 are more tenacious than those found in typical monolithic ceramics. The higher potency of Ti_3SiC_2 bridging grains is almost certainly due to their quasi-plastic nature, which allows for greater damage tolerance and energy dissipation during bridge pull-out and failure. Furthermore, the metallic nature of the bonding obviously precludes the easy fracture of these ligaments as would occur in other layered materials such as mica or graphite.

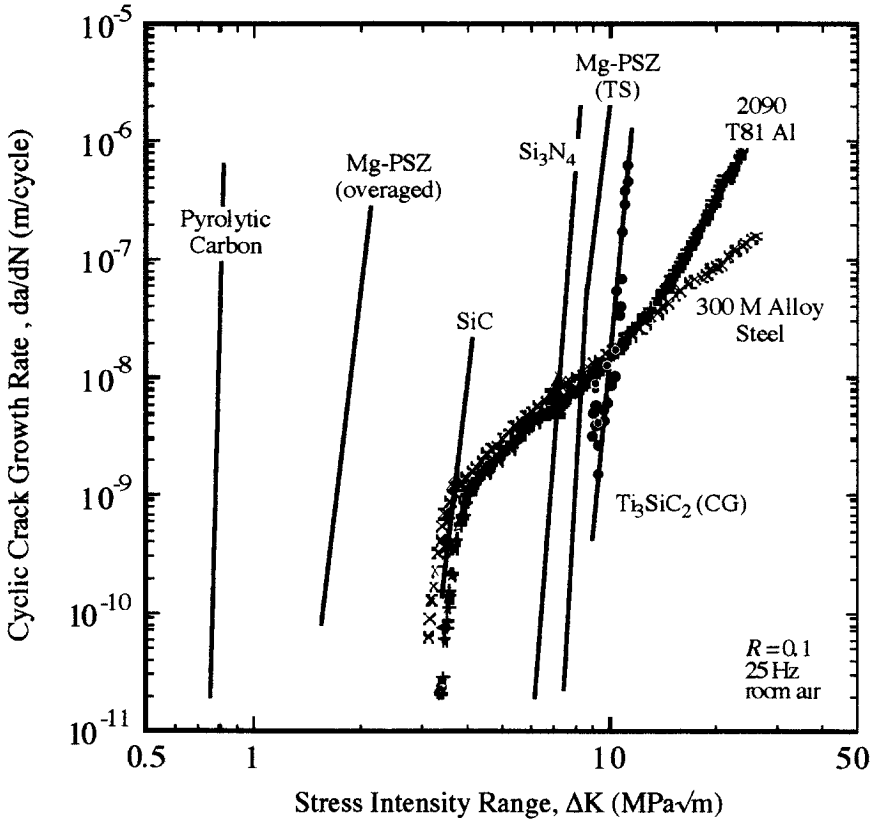

Figure 23: Cyclic-fatigue crack growth rates, da/dN of coarse-grained Ti_3SiC_2 plotted as a function of the applied stress-intensity range, ΔK. Also shown is the behavior of a range of metals and ceramics. The cyclic-crack growth rates in the Ti_3SiC_2 are low and the fatigue threshold is quite high.

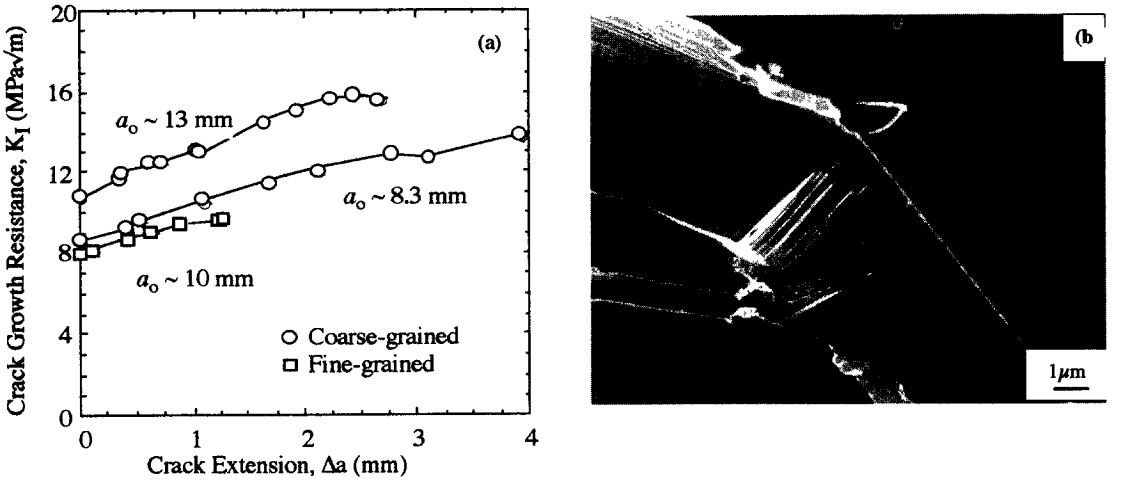

Figure 24: a) Crack-growth resistance, K_I, plotted as a function of crack extension, Δa, for both the FG and CG Ti_3SiC_2 microstructures. The initial flaw size, a_0, is indicated for each measured R-curve. b) Field-emission SEM image of a bridged crack in the CG Ti_3SiC_2. Heavily deformed lamella bridge the crack, and significant amounts of delamination and bending are observed. Such processes are highly unusual in ceramic systems and may, at least partially, account for the extremely high plateau fracture toughness values shown in a.

7.5 Creep Properties

Based on the effect of strain rate on tensile properties (Fig. 18d), the ultimate use of Ti_3SiC_2 at higher temperatures will, most probably, be creep limited. All creep curves exhibit three regimes in succession[106]: i) a very short, primary regime; ii) a region in which the creep rate, $\dot{\varepsilon}$, is more or less constant with time. Since this region also corresponds to the minimum creep rate, $\dot{\varepsilon}_{min}$, it will henceforth be referred to as the minimum creep rate region; iii) a region in which $\dot{\varepsilon}$ is no longer linear with time and gradually increases until failure. i.e. a 'tertiary creep region. The ratio of the duration of the tertiary and minimum creep regions increases as the overall time of the tests increase. At high stresses and lower temperatures, the majority of the strain occurs during the minimum creep rate region[105].

Minimum creep rates, $\dot{\varepsilon}_{min}$, are most often expressed as:

$$\dot{\varepsilon}_{min} = A\sigma^n \exp\left(-Q/RT\right) \tag{20}$$

where A, n and Q are, respectively, a temperature independent constant, stress exponent and activation energy for creep. Least squares fits of ln $\dot{\varepsilon}_{ss}$ vs. ln σ plots (not shown) yield n values that vary between ≈ 1.4 to 1.8. Since one activation energy (≈ 420 kJ/mol) is sufficient to describe the results over the entire range of testing temperatures and stresses, it is fair to assume that one creep mechanism is operative, in which case, based on Eq. 20, a ln-ln plot of $\dot{\varepsilon}_{min} \cdot \exp(Q/kT)$ vs. σ should result in a straight line. Figure 25b shows that to be the case; a least squares fit of which yields n = 1.5 and A = 2.2×10^7 $s^{-1}\cdot MPa^{-3/2}$. It thus follows that in 1000-

1200 °C temperature range and for stresses that vary from 10 to 100 MPa, $\dot{\varepsilon}_{min}$ of FG Ti_3SiC_2 is well represented by[106]:

$$\dot{\varepsilon}_{min} = (2.2 \times 10^7)\, \sigma^{1.5} \exp\left(-\frac{420 \pm 15 kJ/mol}{RT}\right) \tag{21}$$

The time to failure, t_f, is well represented by a Monkman-Grant expression, namely: $t_f(s) = 0.019/\dot{\varepsilon}_{min}$. Two failure modes are observed. At all but the highest stresses, cavities nucleate, more or less homogeneously over the entire gage area, grow and eventually coalesce into relatively large microcracks, whose further growth must be blunted by crack tip plasticity. Because Ti_3SiC_2 lacks five independent slip systems the cavities must form at the very onset of the creep deformation process and not surprisingly most of the strain is attributable to the formation of cavities and microcracks. The second mode, at high stresses, is more reminiscent of subcritical crack growth, in which the cavities form in the local field of a stress concentrator, followed by relatively rapid crack growth.

Currently, not enough data exist to unambiguously determine the creep mechanism(s). The recent realization, however, that Ti_3SiC_2 and ice share more than a passing similarity in their response is an important development that should greatly enhance our understanding of both crystalline solids.

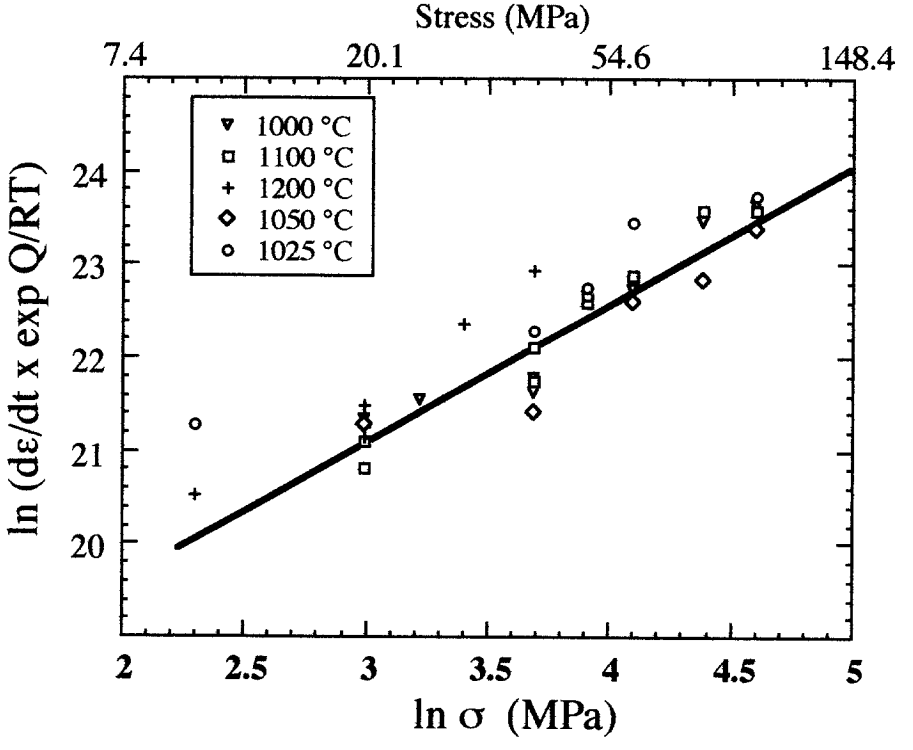

Figure 25: ln-ln plot of $\dot{\varepsilon}_{min} \bullet \exp(Q/RT)$ vs. σ for all temperatures and stress levels. Equation of solid line is given by Eq. 20.

7.6 Tribological Properties

In our first report on Ti_3SiC_2 we noted that there was an element of self-lubricity to the solid[43]. When taken together with its the layered nature and the fact that the bonding between the layers is weaker than along the layers, especially in shear, its relationship to graphite was obvious and pointed out. This led Myhra et al. to measure the friction coefficients of the basal planes of Ti_3SiC_2 using lateral force microscopy[178-179]. They showed that that the basal have one of the lowest friction coefficients, μ, of any solid measured to date. As important, the low values of μ are maintained even after six months exposure to the atmosphere.

Unfortunately, this low μ does not translate to low friction in polycrystalline samples[92]. We recently carried out a detailed wear and friction study on FG and CG discs of Ti_3SiC_2 in pin-on-disk sliding wear tests against a 440C steel pin, and as rectangular pins in diamond belt abrasion tests. In the pin-on-disc test, irrespective of the grain size, it was found that the material undergoes an initial transition stage where the μ increases linearly to 0.15 to 0.45. After this transition stage, μ, rises to steady state values, of about 0.8 for both microstructures. The transition from the low to high μ is due to accumulation of debris entrapped between the disc and the pin, resulting in third-body abrasion.

The average sliding wear rates in the pin-on-disc tests were 4.2×10^{-3} and 1.3×10^{-3} $mm^3/N.m$ for the FG and CG discs, respectively. In the diamond belt abrasion tests, the average wear rates were much higher: $\approx 6 \times 10^{-2}$ and $\approx 4 \times 10^{-2}$ $mm^3/N.m$ for the FG and CG samples, respectively. In contrast to many brittle solids, the wear resistance of the CG samples was better than the FG samples. In both microstructures, grain pull-outs and fractures were observed. In addition, delamination, crack bridging, grain deformation, and microcracking were operative in the CG material. It is this multitude of possible sliding energy dissipation mechanisms, essentially the same observed around hardness indentations, (Fig. 21) that is believed to enhance the wear resistance of the CG material relative to the FG one. These results are consistent with the higher fracture toughness of the CG material (Fig. 24a).

It should be emphasized that the wear resistance was measured under the most stringent conditions, vis. low humidity and no lubricant. Whether the relatively high friction coefficients will prevail in the presence of a lubricant is an open question at this time. The results of Myhra et al.[178-179] suggest that if highly oriented microstructures (or single crystals) can be grown, such that the basal planes are parallel to the surface, such surfaces should exhibit very low μ values, and most probably also be wear resistant. The latter is predictable from the anisotropy in hardness alluded to above.

7.7. Solid Solution Hardening and Softening

Very little work exists on the properties of solid solutions between the $M_{N+1}AX_N$ phases. At room temperature and comparable grain sizes, $Ti_2AlC_{0.5}N_{0.5}$ is stronger in compression (Fig. 19a), harder and more brittle than the end members, Ti_2AlC and Ti_2AlN[97]. This is compelling evidence for the presence of a solid solution hardening mechanism, which in turn implies that dislocations

must play a role with endowing these ternaries with their room temperature quasi-plasticity. It is worth noting here that the failure mode of the end members in compression is not catastrophic, but graceful, with strains to failure of the order of 5 % (Fig. 19a).

Conversely, and quite surprisingly, at temperatures > 1200 °C a solid solution *softening* effect is observed[97], the reasons for which are currently a mystery. This effect, however, is in agreement with the fact the TEC of the solid solution is higher than the end members (Table 7). Thus, partially replacing the C with N atoms, or vice versa, somehow destabilizes the structure at higher temperatures. Here again is a fruitful area for theoretical modeling.

7.8 Machinability

One of the more remarkable properties of the $M_{N+1}AX_N$ phases is the ease by which they can be machined using high-speed tool bits with no lubrication or cooling required. They can even be cut with manual hack-saws. It is important to note that the machining does not occur by plastic deformation, as in the case of metals, but rather by the breaking off of tiny microscopic flakes. In that respect, they are not unlike other machinable ceramics such as Maycor™. The analogyy with ice is also apt. The $M_{N+1}AX_N$ compounds do not machine by scooping ice cream (as in metals), but rather by shaving ice.

7.9 Compression Behavior of Quasi-Single Crystals of Ti_3SiC_2

Before delving into the details of the atomistic models it is important to describe the results of a series of experiments that were key in developing the former. Highly oriented macro-grained samples of Ti_3SiC_2 can be grown by a sinter-forge technique[76]. The grains grow in a chevron pattern that develops normal to the hot pressing or forging direction (Fig. 17c) in which the basal planes are inclined $\approx 30°$ to the horizontal. Normal to that face, the grains extend across the sample width (see Fig. 28).

The room temperature stress strain curves of samples compressed along the x and z directions (inset of Fig. 26) are characterized by a marked anisotropy[76] (Fig. 26). Samples tested in the same direction as the hot pressing or forging direction, (i.e. along x-direction) yield around 200±10 MPa and deform plastically thereafter. These samples can be compressed to strains that exceed 50 % at room temperature. At 1300 °C the shapes of the stress-strain curves (not shown) are similar to those at room temperature, but yield at the lower stress of 120±10 MPa. Post-test examination indicated that the plastic deformation is correlated with the formation of two shear bands, that form parallel to the basal planes (Fig. 27a). Where the shear bands intersect the right-hand edge of the sample a bulge is apparent confirming the plastic nature of the deformation. The two bands intersect left of center, and their intersection results in the creation of cavities and pores (Fig. 27a). A higher magnification optical micrograph of one of the shear bands (Fig. 27b) shows it to be $\approx$ 100 μm wide. At this magnification, the damage appears to be confined to the shear band. Like the shear bands in the polycrystalline samples (Fig. 19b), they are characterized by intense deformation, rotation and breakup of the grains.

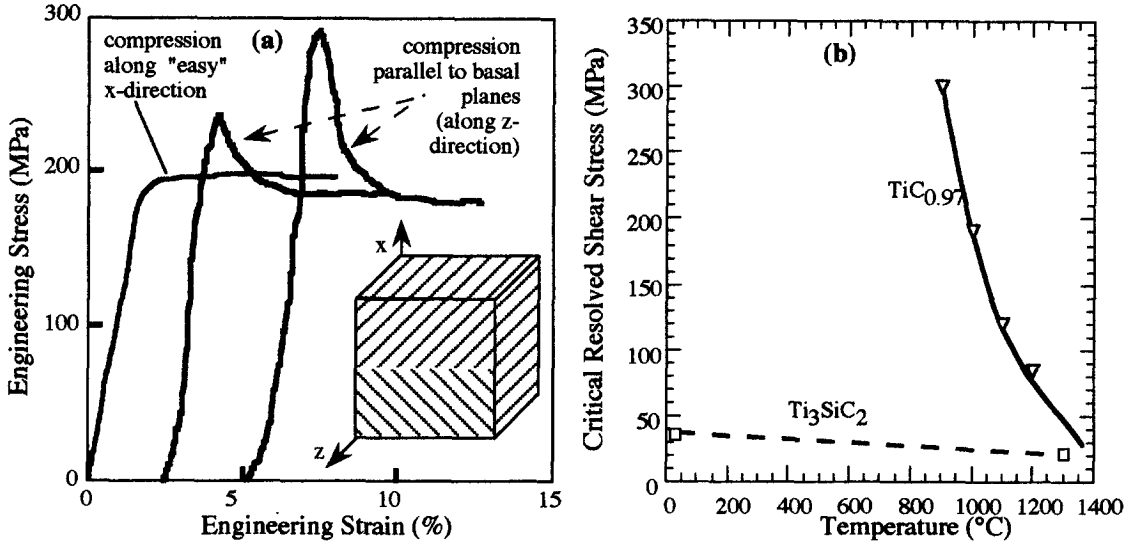

Figure 26: a) Effect of Ti_3SiC_2 grain orientation on room temperature engineering stress-strain curves compressed in the z-directions and the x-direction (i.e. parallel to the basal planes)[76]. The curves are shifted by 2.5 % strain for clarity's sake. Inset is schematic of basal plane orientations relative to the load direction. b) Temperature dependence of critical resolved shear stresses for Ti_3SiC_2[76] and $TiC_{0.97}$[180].

As discussed below, basal plane dislocations are mobile and multiply at room temperature. In other words, the initiation of the shear band is related to dislocation motion. Hence, the data shown in Fig. 26a can be used to estimate the critical resolved shear stress,CRSS. To estimate the latter, the angles between the loading direction and the slip planes and directions must be known. The former is $\approx 65°$. The angle between the slip and the loading directions is unknown. Its maximum value, however, is when the slip direction, $[11\bar{2}0]$, is the same as the slip plane, viz. 65°. Thus the *minimum* critical resolved shear stress at room temperature is $\approx$ 36 MPa. Similarly, the *minimum* CRSS at 1300 °C is estimated to be $\approx$ 22 MPa. Figure 26b compares the CRSSs of $TiC_{0.97}$[180] and Ti_3SiC_2 as function of temperature. At 900 °C, the CRSSs differ by about an order of magnitude; at 1300 °C, they differ be only a factor of $\approx$ 2. This graph dramatically illustrates the fundamental differences in mechanical properties between TiC and Ti_3SiC_2.

The more interesting response occurs when the samples are loaded normal to the basal planes (i.e. along the z-direction in inset of Fig. 26). In this orientation, the resolved shear stress is ≈ 0 and yet significant (> 15 %) plasticity is observed. The stress-strain curves show a clear maximum in the "yield" stress, which is followed by a region of strain softening (Fig. 26), before leveling off at $\approx$ 200 MPa. Two nominally identical samples were tested; one yielded at 230 MPa, the second at 290 MPa. This scatter and strain softening are consistent with the deformation mode proposed below. Here again the deformation is mostly confined to two intersecting shear bands that emanate from the corners and form an inverted chevron shape (Fig.

28a). Where they intersect a large void is present (top center). The most important and telling detail, however, is observed at the corners of the cubes, one of which is shown as an inset in Fig. 28. The plastic buckling of the corner grain occurs by the formation of a kink band (see next section).

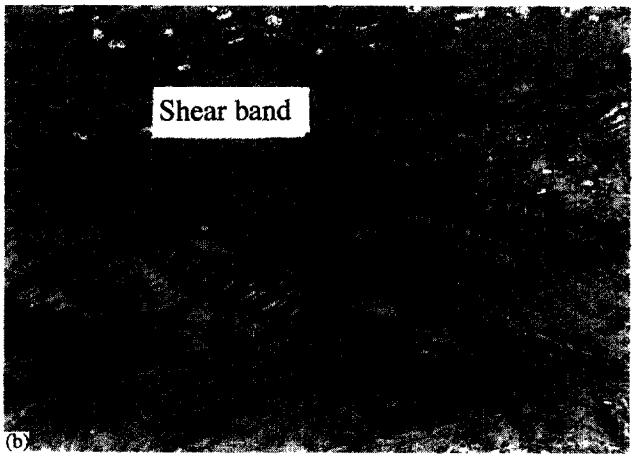

Figure 27: Polished and etched optical micrograph of: a) surface of cube subjected to a 6% compressive strain, in the x-direction[76]. Basal planes make an angle of ≈ 25 ° with the horizontal; load was applied vertically. b) Higher magnification of shear band, where extensive grain breakup, rotation, etc., is apparent. The material outside the shear band appears to have remained intact.

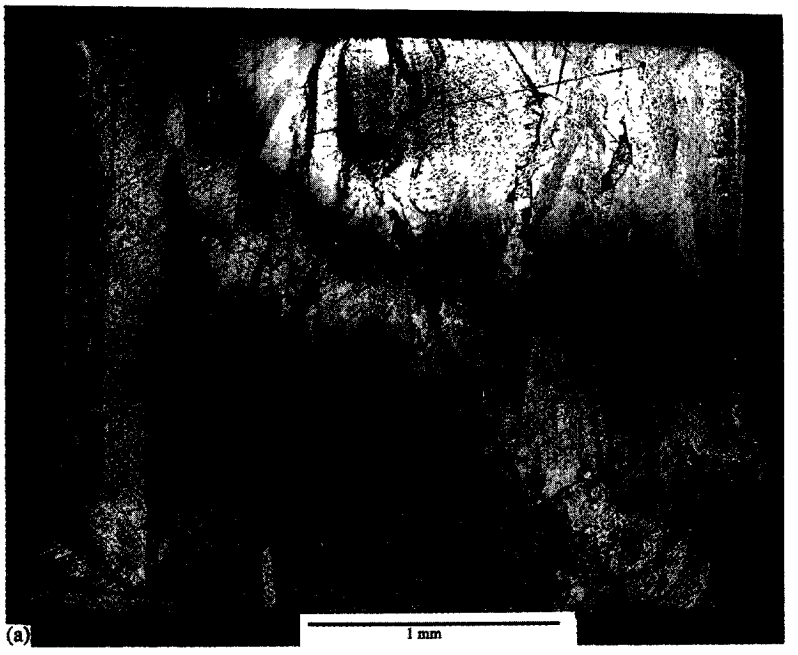

(a)

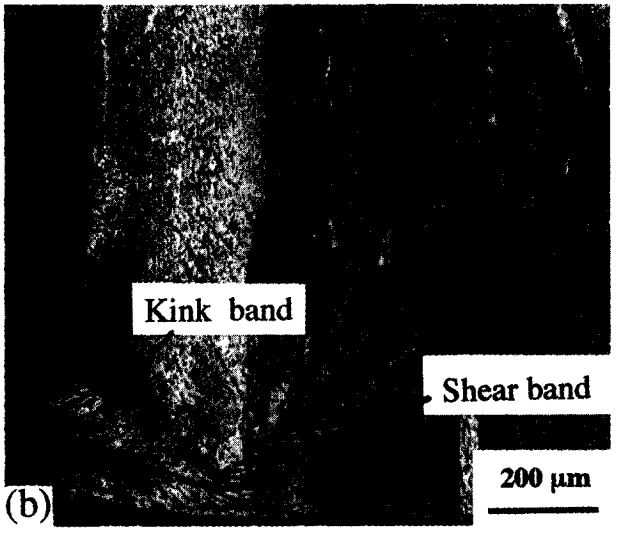

(b)

Figure 28: Polished and etched optical micrograph of surface of cube subjected to a compressive strain along the z-direction in which the basal planes are parallel to the vertically applied load. Inset shows higher magnification micrograph of left-hand side bottom corner. Note buckling of corner and relationship between kind and shear band angles.

The strain softening following the peak in stress observed in Fig. 26a, is clearly a texture-related phenomenon. The simplest interpretation is that the kinking at the corners reorients the basal planes into an easy glide direction. Once reoriented, basal slip takes over resulting in the shear bands. Clear evidence for lattice rotation can be seen in the lower left-hand side corner (Fig. 28b). The kinking or buckling deformation mode is a result of an instability and/or a lack of constraints and as such is dependent on stochastic microstructural features such as imperfections, sharp corners, voids, planar misalignment, etc. The more than 22 % difference in the values of the maximum stresses of the two nominally identical samples (Fig. 26) is consistent with such a deformation mode. In contrast, the stress needed to further plastically deform the crystal, which presumably is dominated by what is occurring within the shear bands, is more or less constant and fairly reproducible at $\approx$ 200 MPa. Furthermore, given the combination of stress concentration and lack of constraint at the corners it is not surprising that they should buckle first and initiate the two shear bands.

7.10 Kink Bands

Kinking and kink bands mostly occur in materials with a strong anisotropy in their shear strengths when they are loaded parallel to their weak shear planes. This mechanism has been invoked to explain deformation in single crystal hexagonal metals[181-183], highly constrained rocks[184], organic crystals[185], card decks[186], rubber laminates[187], oriented polymer fibers[188-192], wood[193], graphite fibers[194,195], laminated C-C and C-epoxy composites[196-198] and highly textured Zn polycrystalline samples[199], among others. Despite the apparent ubiquity of this deformation mode in nature, it is quite rare in polycrystalline crystalline solids, especially if they are not highly constrained.

Orowan was the first to report on the formation of kink bands in single crystals of hexagonal Zn loaded parallel to their basal planes[181]. Later, Hess and Barrett[182] proposed a model to explain the formation of these bands by the regular glide of dislocations. The major elements of their model are summarized schematically in Fig. 29a to d. Initially and upon loading a long thin column of length L, elastic bending (Fig. 29a) creates maximum shear stresses, assuming perfect symmetry, at L/4 and 3L/4 (Fig. 29b). Above a critical value this shear stress is sufficient to create, within the volume that is to become the kink band, pairs of dislocations of opposite sign that move in opposite directions (Fig. 29c). The end result is two regions of severe lattice curvature, separated from each other and from the un-kinked crystal, by well-defined kink planes BC and DE in Fig. 29d. These kink planes or boundaries have an excess of edge dislocations of one sign, which, in turn, are responsible for the lattice rotations observed. Such kink bands would be expected only in crystals that are not subject to twinning as a result of compressive stresses, such as hexagonal metals or alloys having an axial c/a ratio greater than ≈ 1.73[182]. It is thus not surprising that Ti_3SiC_2 with a c/a ratio of 5.76, and the other $M_{N+1}AX_N$ phases, deform by this mechanism. In contrast to twining, the plane of kinking need not be a crystallographic plane; its orientation depends on the stress condition[181].

Hess and Barrett did not elaborate on the specific mechanism for the formation of the kink planes or dislocations walls. A few years later Frank and Stroh[200] proposed a model in which

pairs of dislocation of opposite sign nucleate and grow at the tip of a thin elliptical kink (labeled T in Fig. 29e), when the applied shear stress exceeds some critical value. As long as the pair of dislocation walls are within the crystal or grain they are attracted to each other but are held apart by the external stress (Fig. 29e). Once the walls extend to the free surface the strong attraction disappears and the dislocation walls become parallel planes (Fig. 29f). A continuing stress

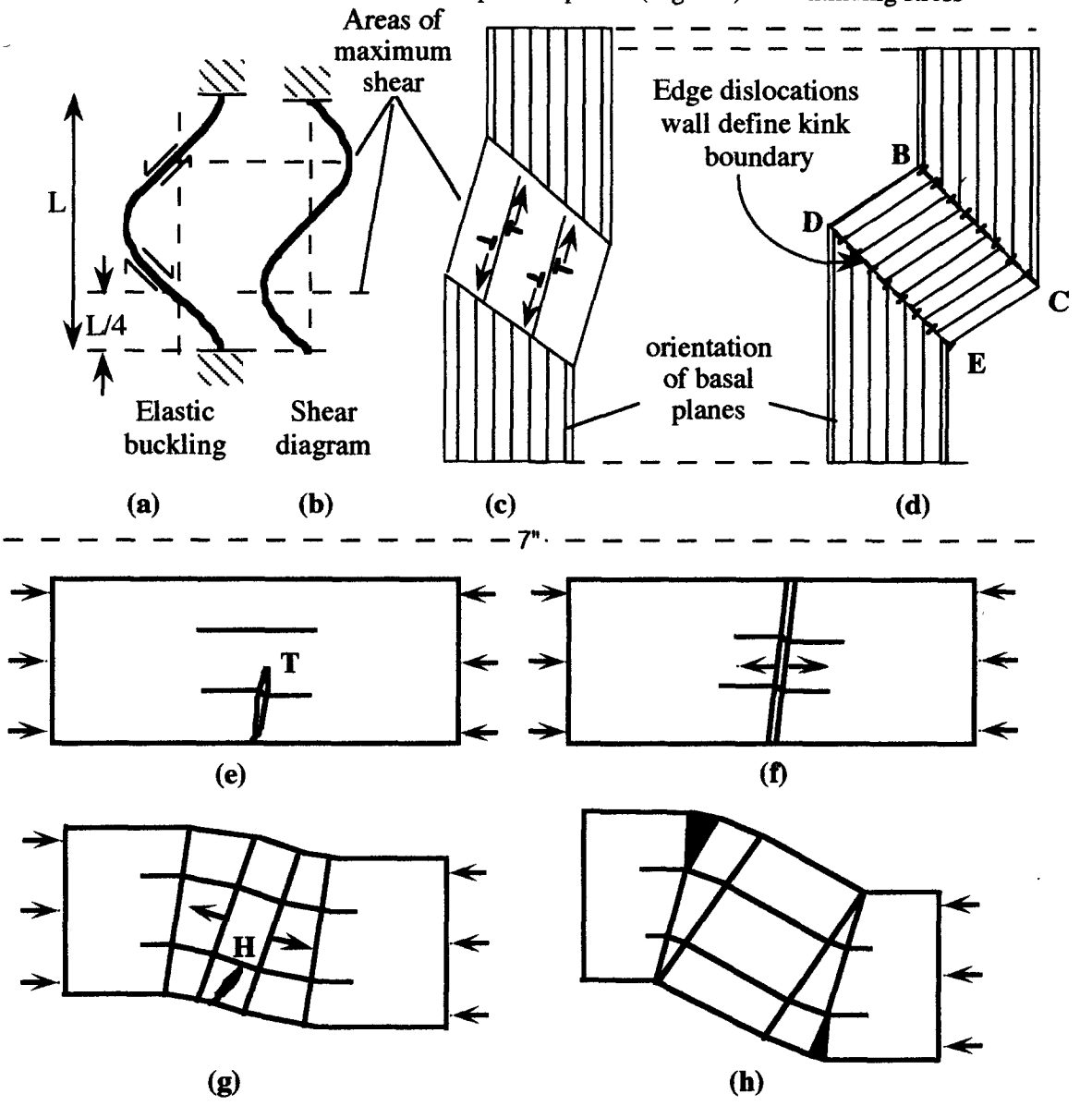

Figure 29: Scheme of kink band formation a-d after Ref. [182] and e-h after Ref. [200]. a) Elastic buckling, b) corresponding shear diagram showing maximum shear at l/4 and 3L/4. c) Initiation of pairs of dislocations from area of maximum shear. d) Kink band and kink boundaries comprised of edge dislocations of one sign giving rise to classic stove-pipe shape; e) Initiation of kink band at tip of narrow kink, T; f) Intersection of T with free surface removes the attractive energy between the walls and allows them to separate and move in opposite directions; g) and h) repetition of same process to create more dislocation walls.

should then force the walls apart. The process of wall formation can be then repeated at the same source resulting in the generation of new dislocation walls (Fig. 29g-h). If the component dislocations in successive walls are not on the same slip plane, the walls could unite or collapse forming a kink plane or boundary. The collapse does not occur simultaneously along the whole wall but sequentially, starting at one end of the kink boundary and moving to the other end as shown schematically in Figs. 29h.

The accumulation of several walls in a relatively thin region create a kink boundary. Hess and Barrett also suggested that the first wall can be stopped by some defect resulting in accumulation of walls near the defect. Alternatively, as proposed by Frank and Stroh, since each wall has a different angle to the external load, as a result of successive changes of lattice direction (Fig. 29h), the increase in the shear stress for each successive wall formed may result in their moving faster, leading to their accumulation.

A dislocation wall extending across a grain is a low-energy configuration (Fig. 30a). However, if, for some reason, the dislocation wall is forced to divide (Fig. 30b), Stroh[201] has shown that the magnitude of the stress between the ends can be high enough to open a crack of limited length propagating normal to the wall as shown in Fig. 30c. Typical examples of delaminations associated with dislocation walls observed in Ti_3SiC_2 are shown in Fig. 30d and e, where the resemblance of some of the features in this micrograph with the schematic shown in Fig. 30c is obvious. Delaminations are always associated with walls. Direct evidence for the arrangement of dislocations in a wall is shown in Fig. 30f, which is a higher magnification TEM micrograph of the feature depicted by arrows in Fig. 30d[84].

7.11 Atomistic Deformation Processes in Ti_3SiC_2

One of the more intriguing questions concerning the mechanical properties of Ti_3SiC_2, and related materials, is their ability to contain damage, i.e. their damage tolerance. At face value this is a surprising result for a layered material that is so clearly prone to delamination and lacks 5 independent slip systems. In this section a dislocation based model, that builds on earlier ideas proposed for kink band formation in hexagonal metallic single crystals[181,182,20,201] is presented that explains most of our TEM observations as well as why these materials are damage tolerant.

Before describing the model it is necessary to describe the types and arrangements of the dislocations that exist. Dislocations in Ti_3SiC_2 are overwhelmingly arranged either in arrays (Fig. 31) wherein the dislocations exist on identical slip planes; or in dislocations walls, wherein the dislocations form a low angle grain boundary normal to the basal planes[72,82,84]. The arrays propagate across entire grains and are responsible for deformation by regular glide. The walls form as a result of the formation of the kink bands. A typical example of a series of almost parallel walls is shown in Fig. 32a. Selected area diffraction patterns (Fig. 32b) provide compelling evidence that these walls result in lattice rotation and consist of rows of dislocations. A schematic of the arrangement is shown in Fig. 32c.

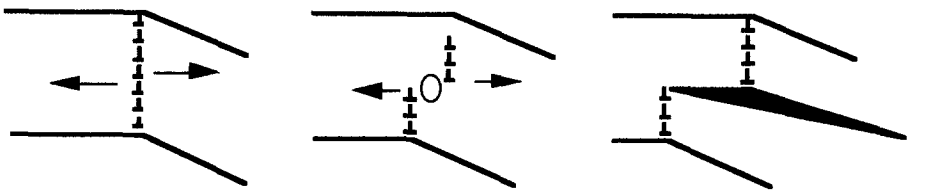

(a) (b) (c)

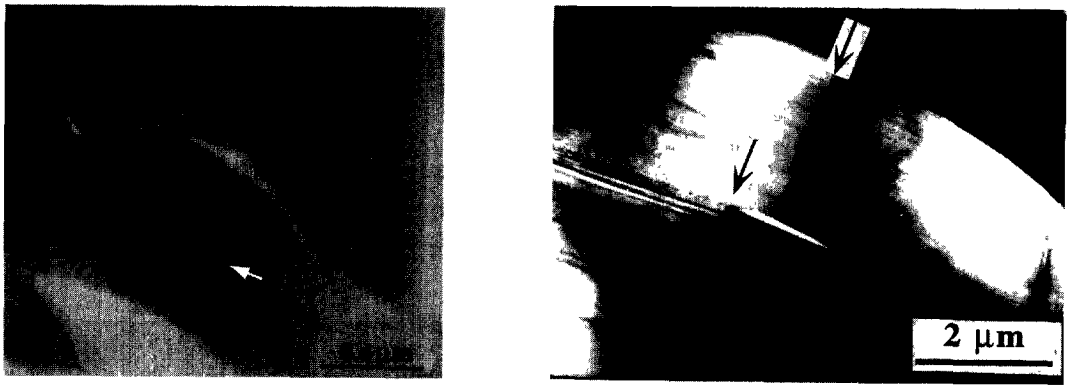

(d) (e)

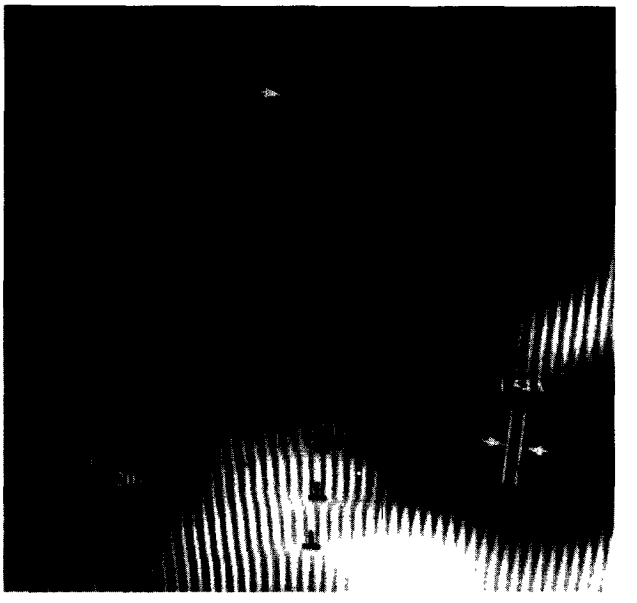

(f)

Figure 30: a-c Nucleation of a crack normal to a dislocation wall when the latter is subjected to a shear stress taken from Ref. 201. d), and e) TEM micrographs showing a number of delaminations associated with dislocation walls. f) Higher magnification TEM micrograph of dislocation wall depicted by arrow in d in which individual dislocations and their alignment is obvious.

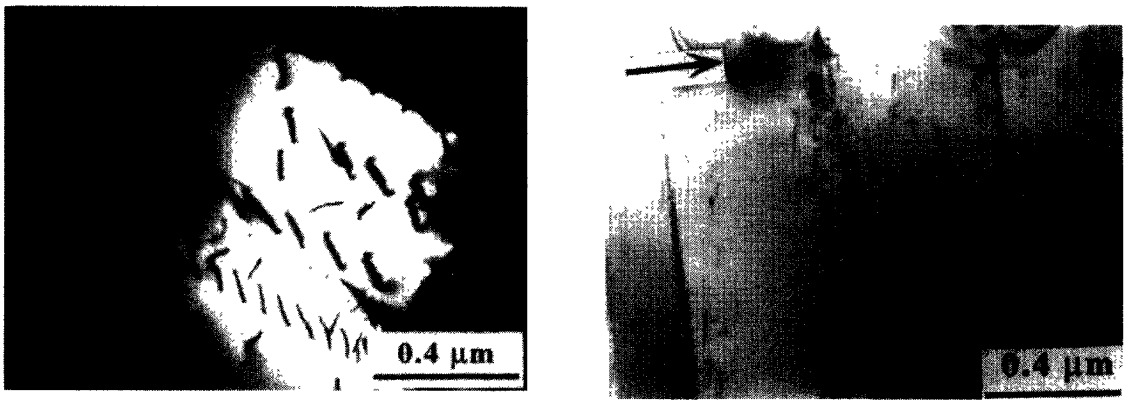

(a) (b)

Figure 31: a) Typical TEM micrograph after deformation at room temperature. Number and spatial extent of dislocation arrays is greatly increased compared to the undeformed samples[72]. b) Bright field image of an area containing dislocation arrays. Specimen is close to the orientation where basal planes are in an edge-on position[84].

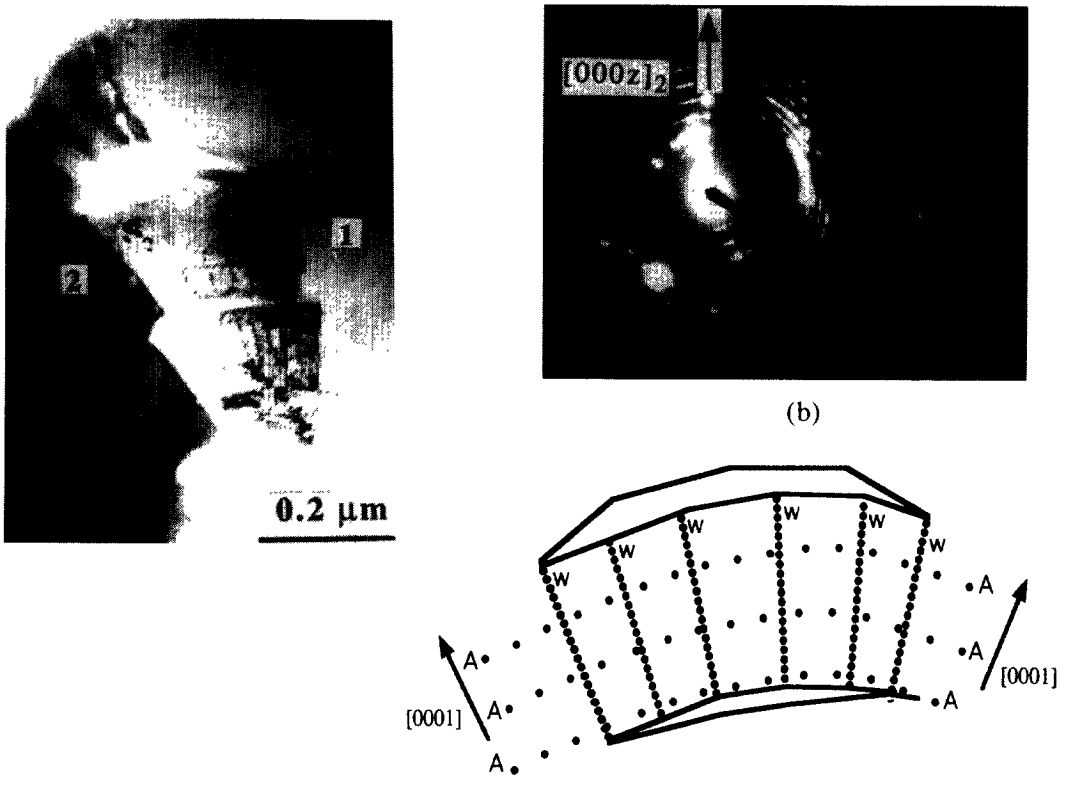

Figure 32: a) Bright field image of a bent region delaminated in 3 slices S_1-S_3 and containing separated walls and arrays. (b) Selected area diffraction from the same region, but tilted to an edge-on position for the basal planes demonstrating lattice rotation around $<1\bar{1}00>$ directions; (c) schematic of S_2 showing walls (W) and arrays (A).:

The key to understanding the mechanical response of Ti_3SiC_2, especially under compression, is to appreciate the four following facts. Fist basal plane dislocations are mobile and multiply at room temperature. Second, as noted above, these dislocations are overwhelmingly arranged either in arrays or walls. Third, the intersection of the arrays and walls can result in delamination. Fourth, the metallic nature of the bonding insures that the layers, once delaminated remain intact, rather than fracture. It is this combination of attributes that cause these ternaries to behave as nanolaminates.

A bright field image of a kink band with a high misorientation angle containing delamination cracks is shown in Fig. 33[84]. The classic "stove pipe" shape predicted by the model (Fig. 29d) is obvious. It is important to note that none of the models dealing with kink band formation discuss delaminations, since the latter do not occur in metals. Such delaminations, however, have been observed in single crystal SiC samples deformed at temperatures in excess of 1500 °C[202]. Separate dislocation walls, which are generally normal to the basal planes, but are inclined to the kink boundaries, are denoted by V giving rise to the V-shaped regions predicted in Fig. 29h. Delamination cracks are *always* associated with the kink bands, and are typically present along the basal planes *near or at dense* dislocation arrays. The sizes and asymmetries of the delamination cracks vary: The larger cracks are asymmetric, with the longer part typically propagating into the kink band. Some of these cracks propagate across the entire kink band, i.e. from kink boundary to kink boundary (Fig. 33). The ends of the delamination cracks are typically bound at one side by the original kink boundary that is dislodged parallel to the basal planes and outwards relative to the kink bands; the other side propagates into the kink band and is typically bound by a single dislocation wall.

A dislocation-based model, shown schematically in Fig. 34, has been proposed to explain most of the microstructural features observed in our work. The model also goes a long way in explaining the mechanical response of Ti_3SiC_2, especially in compression[84]. The basic elements of the model are: shear deformation by dislocation arrays, cavitation, creation of dislocation walls and kink boundaries, buckling and delamination. For the sake of brevity, only the model is presented here, the evidence for which can be found in Ref. 84.

Consider the two adjacent grains labeled S and P in Fig. 34a subjected to a vertical load. Because of the their orientation, the resolved shear stress on the basal planes (parallel line) of grain S is non-zero, while those in grain P are. The solid gray area in the figure represents the width, W, of grain P that ultimately buckles. When the resolved shear stress exceeds the critical value in grain S, it will deform by shear toward the lower left in Fig. 34a. This shear will occur by the formation of dislocation arrays. Grain P will not deform initially. The shear of grain S away from P, however, will create a cavity at the grain boundary between the two grains as shown schematically in Fig. 34b. As a consequence of the formation of this cavity, the shaded volume will tend to relax into that cavity, first elastically and then plastically. The plastic deformation is initially accommodated by the formation of dislocation arrays (represented by *dotted* vertical lines in Fig. 34b) that extend across the whole grain as a direct result of the shear stresses between the shaded area and the remainder of the grain. The change in shape can also be accommodated by the generation of dislocation walls normal to the applied load. These are depicted in Fig. 34b as short horizontal lines within the shaded area.

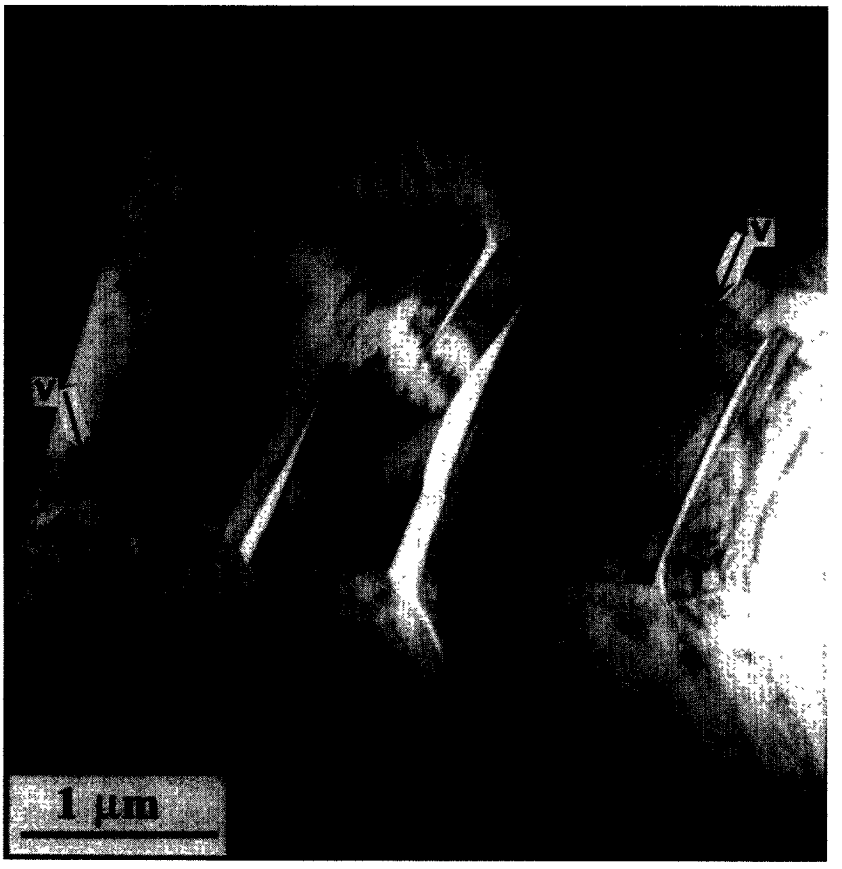

Figure 33: Bright field TEM image of a kink band with a high misorientation angle ("stove pipe") containing delamination cracks. Separate dislocation walls, which are generally normal to the basal planes, but are inclined to the kink boundaries are denoted by V. The same areas are depicted in Fig. 29h as dark triangles.

Upon further loading the shaded volume will, depending on its exact geometry relative to the location of the cavity and the local state of stress, plastically buckle into the cavity. Where along the length, L, of the lamella the shear is maximum depends on many factors such as the length-to-width ratio of the buckling section, the location of the constraints relative to L, and the symmetry of the loading environment, among others[182]. For example, in Fig. 29b the maximum shear is assumed to occur at L/4 and 3L/4. Regardless of the exact locations of the areas of maximum shear, the formation of shear bands requires that dislocation pairs be emitted from the center of what is to become the kink band and move in opposite directions[182]. This is a fundamental distinction between deformation by shear and kink band formation. For the sake of simplicity, the locations of maximum shear are chosen to be the areas labeled X and Y in Fig. 34b. It is the emission of dislocation walls of opposite sign from these locations that ultimately results in two kink bands, BC and DF, shown in Fig. 34c, or equivalently BC and DE in Fig. 29d.

It is worth noting that as the lattice rotates as a result of the formation of the dislocation walls and kink boundaries, the maximum shear stresses increase leading to an acceleration of the formation of these walls and can lead locally to geometrical softening[183].

Since the buckling and kinking occur while maintaining the mechanical integrity of the grain, then perforce the ends of the buckled volume (labeled A in Fig. 34c) *must* shear towards the center of that grain. Here again, the shear occurs via dislocation arrays that form in the buckled region. From a purely geometrical perspective (since only basal slip is available), the kink bands *cannot* form without the concomitant formation of delamination cracks (see Fig. 34c and d). The thickness of the delaminated lamellae, i.e. W, will depend on their radius of curvature, R, which in turn depends on the size of the cavity into which the material can buckle. The smaller the cavity, the higher the stresses needed and the thinner the lamella that are generated. Furthermore, thick lamella form first; as the stress is increased, however, they sequentially delaminate at W/2, W/4, ... etc. One mechanism how this can occur is shown in Fig. 34d. Upon further deformation, the two kink boundaries at C and D, in which the dislocations have the same sign, collapse into one, labeled G-H in Fig. 34d. Their delamination cracks merge and result in the larger delamination shown.

The dislocations density accommodated at any kink boundary, before tensile stresses at the core of these dislocations exceeds the rupture stress of the material, is limited. It is therefore not surprising that delaminations initiate at these boundaries. Hence further bending the original kink boundary splits it into the two shorter kink boundaries labeled G and H (Fig. 34d). The delamination cracks occur at the intersection of the arrays and kink boundaries. (This is why the central dotted line in region W in Fig. 34c is absent in Fig. 34d). The formation of a free surface annihilates the dislocations in that array and eliminates the accompanying strain energy. Here again shear of one lamella relative to the other has to occur via the dislocation arrays that are present in all lamella. It is believed that a repetition of this mechanism results in thinner and thinner lamella with sharper and sharper radii of curvatures such as the ones shown in Fig. 16a to c. Not only are delamination cracks intimately related to the formation of kink bands, but as importantly they are *contained* within these bands. Thus, for example, the small delamination cracks shown in Fig. 34d, are contained between the kink boundaries B and F. This containment occurs regardless of how far the delamination cracks are from the edge of the specimen and thus cannot be attributed to the reduction of the stress intensity at the crack tip due to changing geometry. The main reason is more fundamental: for the delaminations to extend beyond the kink bands requires that the kink boundary, with its very high dislocation density, be moved ahead of the crack tip. This is energetically very costly and leads to localized toughening. The delaminations can easily move in the opposite direction, i.e. into the kink band because there are no dislocations in that direction, which is why the delamination cracks are asymmetric.

In short, the delaminations and associated damage are bound (i.e. localized) by the kink boundaries. The latter can be thought of as "reflectors" of damage. This containment of damage is believed to play a major role in endowing these ternary compounds with their damage tolerant properties.

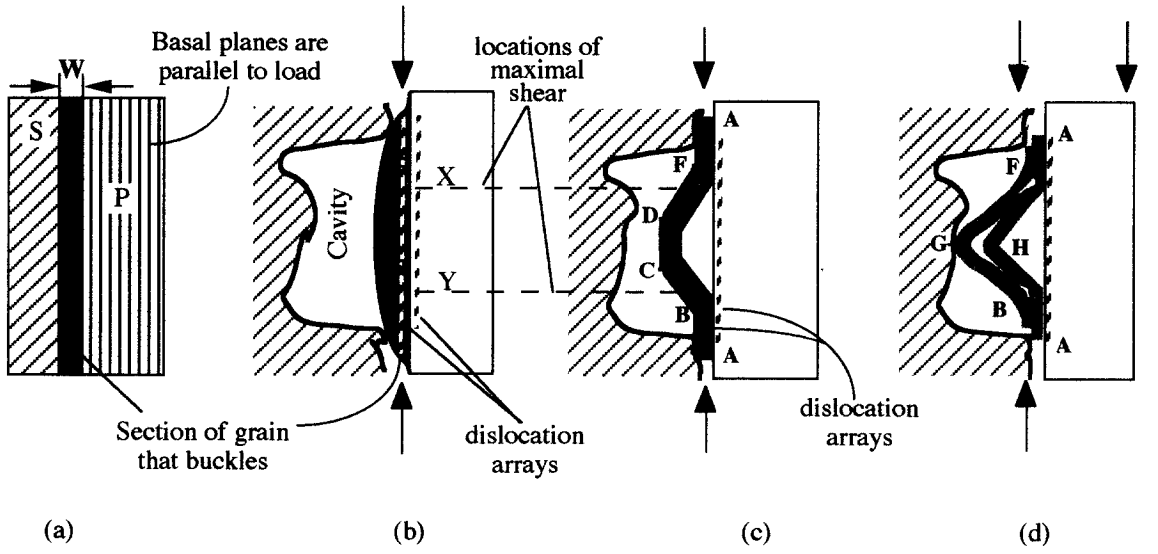

Figure 34: Proposed model. a) Initial state showing two grains S and P subjected to a vertical load. The gray area labeled W, is portion of grain P that ultimately delaminates; b) Initial deformation occurs by the formation of dislocation arrays (dashed vertical lines) and dislocation walls (short horizontal lines). Areas of maximum shear are assumed to be at X and Y. c) The locations of maximum shear become the centers of two oppositely oriented kink bands BC and DF. d) Further deformation forces the kink boundaries C and D to merge into the split into G and H. Note that even if the delamination cracks down the center of the gray area merge, they are still contained within the region bounded by B and F. Note disappearance of dislocation array.

8. CHEMICAL REACTIVITY AND TOPOTAXIALITY

8.1 Oxidative Properties

Binary transition metal carbides and nitrides are not very oxidation resistant in air above ≈ 500 to 800 °C. Prior to our work, that was also the conventional wisdom about Ti_3SiC_2[32,39,40]. Given the importance of oxidation in practical applications, one of the first papers we published on Ti_3SiC_2 was a study of its oxidative properties[67]. The overall oxidation reaction is:

$$Ti_3SiC_2 + 5\,O_2 \Rightarrow 3\,TiO_2 + SiO_2 + 2\,CO^{\ddagger} \qquad (II)$$

The oxidation kinetics are parabolic, with parabolic rate constants, k_p, that increase from $1x10^{-9}$ to $1x10^{-4}$ $kg^2 \bullet m^{-4}s^{-1}$ as the temperature increases from 900 to 1400 °C, respectively. The activation energy for oxidation is 370±20 kJ/mol. The scale that forms is dense, adhesive, resistant to thermal cycling and layered. The outer layer is pure rutile, TiO_2, and the inner layer

‡ The fate of the C is unknown. In order to balance the equation it was assumed that it diffuses through the reaction layer and oxidizes into CO.

consists of a mixture of SiO_2 and TiO_2 (Fig. 35a). The oxidation occurs by the inward diffusion of oxygen and the simultaneous outward diffusion of titanium and carbon.

The presence of small volume fractions ($\approx 2\%$) of TiC_x in Ti_3SiC_2 has a deleterious effect on its oxidation kinetics[67]. This fact is important and is still not fully appreciated in the literature. At least two recent reports on the oxidation of Ti_3SiC_2 claimed that the oxidation kinetics are not parabolic[45]. This, we believe, is more a reflection of the fact that the samples tested were not sufficiently pure, than an intrinsic property of Ti_3SiC_2. This comment notwithstanding, more work on the oxidation of Ti_3SiC_2, especially for longer times on pure samples should be carried Using Wagner's theory of oxidation, it is possible to convert the parabolic rate constants to diffusivities. A comparison of the values of D thusly determined with the values for the diffusion of oxygen and titanium in rutile (Fig. 35b), strongly suggest that the rate-limiting step is either the diffusion of oxygen in or titanium out through that layer.

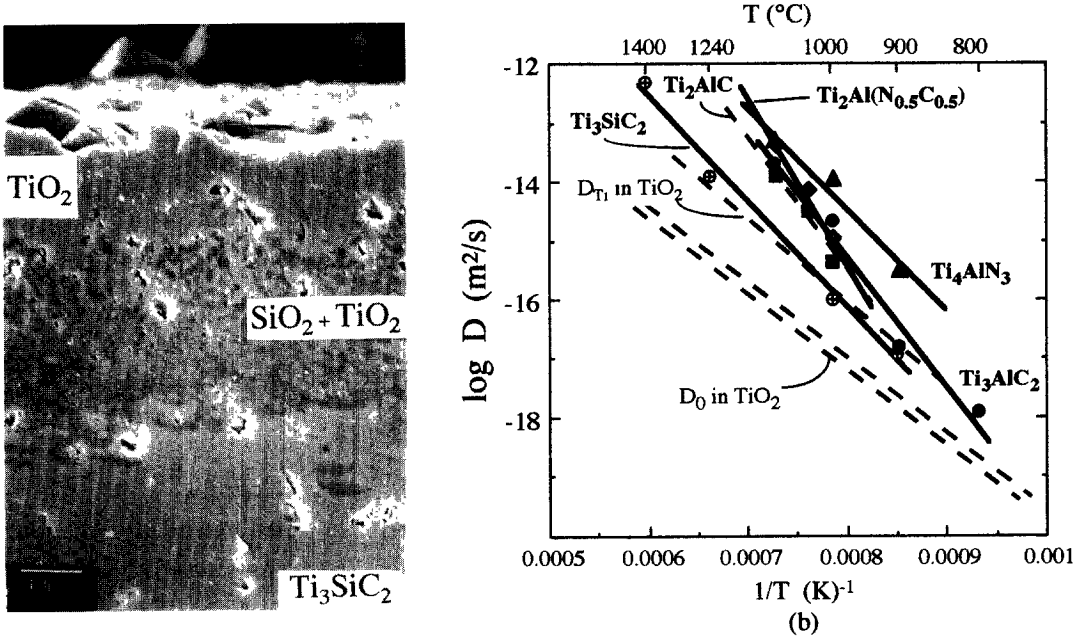

Figure 35: a) Morphology of oxide layer that forms after an cycling a Ti_3SiC_2 sample from 1100 °C to room temperature six times. Total time the sample spent at 1100 °C is 12 hrs. Outside layer is pure TiO_2, the inner layer is a two phase mixture of TiO_2 and SiO_2. b) Arrhenian plot of diffusivity of rate limiting step calculated from parabolic rate constant measurements on ternary carbide indicated. Also shown as dashed lines are the diffusion coefficients of oxygen and Ti in rutile.

The overall oxidation reaction for Ti_2AlN, Ti_2AlC, $Ti_2AlN_{0.5}C_{0.5}$, Ti_3AlC_2 and Ti_4AlN_3 is[108-110] in the 800–1100 °C temperature range is given by:

$$Al + (n+1)\,Ti + [(n+1) - \frac{y-3z}{4}]O_2 \Rightarrow (n+2)[Al_{\frac{y}{n+2}}Ti_{1-\frac{1}{n+2}}]O_{[\frac{2(n+1)}{(n+2)} - \frac{y}{2(n+2)}]} + \frac{z}{2}Al_2O_3 \qquad \text{(III)}$$

The oxidation products are rutile, in which some Al is dissolved, i.e. $(Al_yTi_{1-y})O_{2-y/2}$ with $y < 0.01$ and Al_2O_3. The oxidation occurs by the inward diffusion of oxygen and the outward diffusion of Al and Ti ions through the $(Al_yTi_{1-y})O_{2-y/2}$ layer. The C and N are presumed to diffuse through the reaction layers and oxidize. The subjection of the $(Al_yTi_{1-y})O_{2-y/2}$ layer to the oxygen potential gradient imposed during the oxidation results in its demixing. The Al dissolves into the rutile at the low oxygen partial pressure side and reprecipitates as Al_2O_3 on the high partial pressure side. If extensive, the demixing results in the formation of layers of porosity, through which further Al diffusion cannot occur. The porous layers, however, allow oxygen to diffuse through. The resulting microstructures are highly striated, where three layers, an Al_2O_3-rich layer, an $(Al_yTi_{1-y})O_{2-y/2}$-rich layer and a porous layer, repeat (Fig. 36).

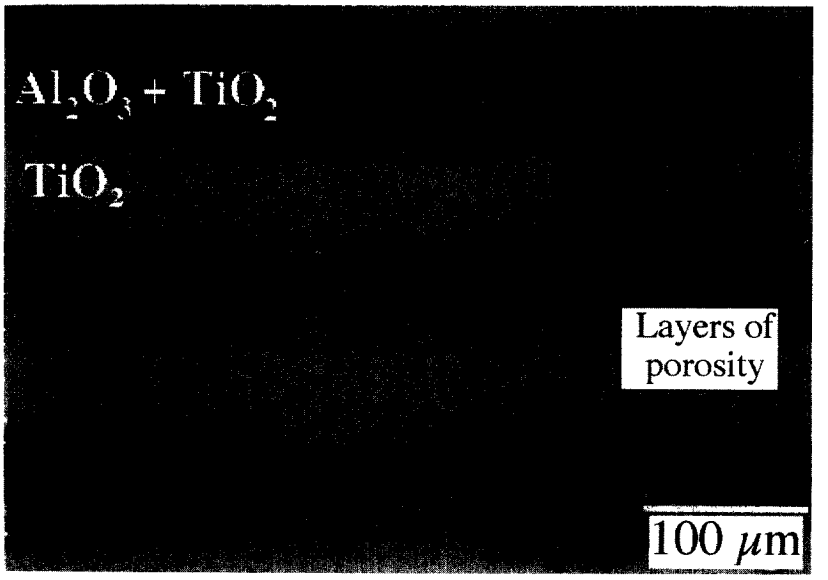

Figure 36: Morphology of oxidation layer that forms on $Ti_3Al_{1.1}C_{1.8}$ after extended oxidation. The oxide layer is striated where three layers repeat: an Al_2O_3-rich layer (gray phase), a TiO_2-rich layer (lightest layer) and a porous layer (black)[110].

Converting the parabolic rate constants to diffusivities and comparing the results with previously published results (Fig. 35b) again supports the conclusion that diffusion of oxygen and/or Ti through the $(Al_yTi_{1-y})O_{2-y/2}$ layer is rate limiting. Because of the dissolution of the Al in the rutile and the concomitant formation of point defects, $[V_O^{\bullet\bullet}]$ and/or $[Al_i^{\bullet\bullet\bullet}]$, the oxidation resistances of the Al-containing ternaries are worse than those of Ti_3SiC_2 (Fig. 35b).

The overall oxidation reactions for Nb_2SnC and Hf_2SnC depend on temperature. At lower temperatures ($\approx 400°C$) the reactions are[203]:

$$Nb_2SnC + 4\,O_2 = Nb_2O_5 + SnO + CO_2 \quad \text{(IV)}$$

$$Hf_2SnC + 3.5\,O_2 = 2\,HfO_2 + SnO + CO_2 \quad \text{(V)}$$

At higher temperatures, ($\approx$700 °C), SnO is not a stable phase, and the oxidation results in formation of SnO_2 instead. The oxidation kinetics are not parabolic but are characterized by an incubation period during which the samples gain little or no weight followed by a region where

the oxidation is linear and quite rapid (Fig. 37). Once in the linear regime the oxidation proceeds until the entire sample is converted to the oxides[203].

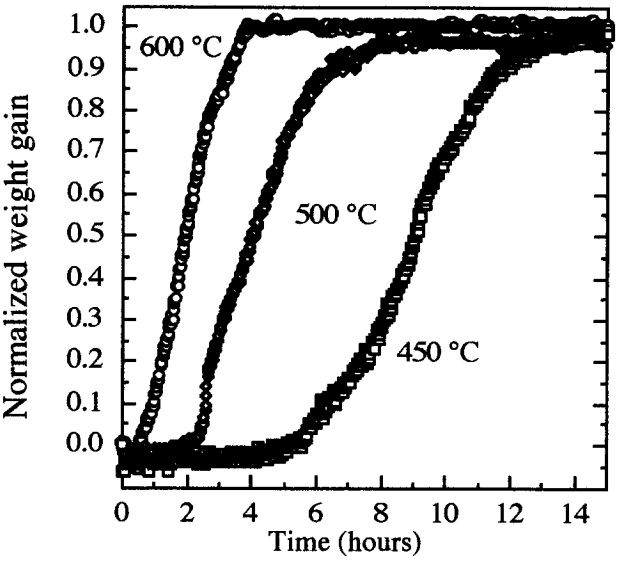

Figure 37: Normalized weight gain versus time curves obtained during the oxidation of Hf_2SnC[203] at temperatures indicated. Note incubation period followed by complete oxidation of samples.

8.2 Chemical Reactivity and Topotaxiality

Based on the Rietveld analysis of the HTND results, and some of the micrographs shown in the previous sections, it is not surprising that one of the preferred modes of reaction of Ti_3SiC_2 is the topotactic loss of Si leaving TiC_x behind. The reaction of Si with molten cryolite[90], graphite[70] and molten Al[100] all take that form.

The reaction of Ti_3SiC_2 with graphite provides an excellent example of the topotactic nature of that reaction[70]. At low magnifications the carburized microstructures (Fig. 38a) are indistinguishable from the original ones (not shown). This has the following important implications. First, the growth of the TiC_x layer must occur by the inward diffusion of C. There is no other plausible mechanism (such as the outward diffusion of Ti for example) by which carburization can proceed while maintaining the topotaxial relationship observed. Second, the TiC_x layer grows by the inward diffusion of C, the conversion of Si planes into C planes and the loss of Si. The overall carburization reaction is thus:

$$Ti_3SiC_2 + (3x\text{-}2)\,C = 3\,TiC_x \;(x > 0.8) + Si \qquad \Delta V = -15.7\,\% \qquad \text{(VI)}$$

In accordance with the negative 15 % volume change for this reaction the TiC_x that forms is not monolithic but forms in a continuos porous TiC_x network (Fig. 38b). According to the phase diagram, this TiC_x is C-rich[48]. Lattice parameter measurements of the TiC_x confirm that the minimum value of x is 0.8[204]. However, on the basis of the hardness measurements and the diffusivity calculations discussed below, x is probably much closer to 1.

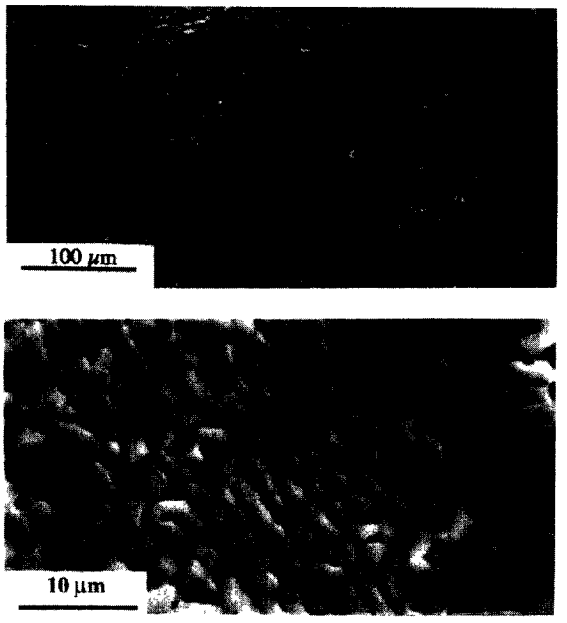

Figure 38: SEM micrographs of: a) top view of carburized layer where original grain structure of Ti_3SiC_2 is clearly preserved confirming topotactic nature of reaction. b) same as a but at a higher magnification showing interconnected porosity[70].

The carburization kinetics are parabolic and thus diffusion controlled. By making a number of plausible assumptions, the parabolic rate constants were converted to diffusivities and compared with the self-diffusion coefficients of C in TiC_x measured using ^{14}C radioactive tracers in the 1450-2280 °C temperature range[205,206]. The agreement of our data (open circles) with the latter set is excellent (Fig. 39) and is compelling evidence that the rate limiting step during the carburization reaction is the inward diffusion of C. The excellent agreement is also evidence that x in TiC_x is > 0.8, since our results agree with those of Sarian[205] who measured the diffusion of C in $TiC_{0.97}$ and $TiC_{0.887}$. Furthermore, since the microhardness of the carburized layer is ≈ 20-25 GPa, its wear resistances should be excellent.

The reaction of Ti_3SiC_2 with molten cryolite follows a similar script, but one in which the exiting Si is not replaced[90]. Immersion of Ti_3SiC_2 samples in molten cryolite at 960 °C results in the preferential diffusion of Si atoms out of their basal planes to form a Si-containing cubic phase with approximate chemistry $Ti(C_{0.67},Si_{0.06})$. The overall reaction is:

$$Ti_3SiC_2 \text{ (hexagonal)} = Ti(C_{0.67},Si_{0.06}) \text{ (cubic)} + \underline{Si} \text{ (in cryolite)} \qquad \text{(VII)}$$

Raman spectroscopy, X-ray diffraction, optical, scanning and transmission electron microscopy all indicate that the Si exits the structure topotactically, in such a way that the C-atoms remain partially in their ordered position in the cubic phase[90]. Furthermore, selected area diffraction, SAD, TEM patterns of the reaction layers showed that they were cubic with a lattice parameter of 2.5 Å. The SAD patterns also unambiguously showed the presence of two sets of (111) planes at an angle of ≈ 39° between them. In other words, the $Ti(C_{0.67},Si_{0.06})$ forms in domains. An idealized schematic of the transformation is shown in Fig. 40. The removal of the

Si atoms in essence allows a de-twinning of the Ti_3C_2 blocks into *domains* in which the orientations of the (111) planes are mirror images of each other. The angle between the (111) planes of the two variants should be 38° 56', a value in excellent agreement with the value measured in the TEM. Not surprisingly, the basal planes in Ti_3SiC_2 become the (111) planes in the cubic phase. The details of this de-twinning are not understood at this time.

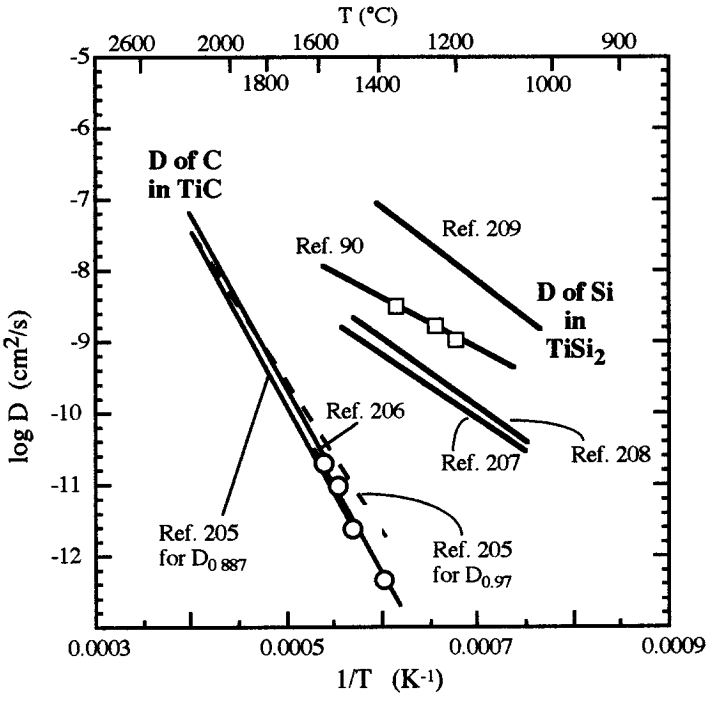

Figure 39: Comparison of Arrhenian plots of diffusion coefficients for C in TiC_x calculated from the parabolic rate constants (open circles) measured from carburization experiments[70], to those previously reported in the literature[205,206]. Also shown are the diffusion coefficients for Si in $TiSi_2$ calculated from silicidation experiments (open squares)[70] and those previously reported[207-209].

Optical micrographs of samples that were immersed in the cryolite Si diffuses along the basal planes within a grain, and then along the grain boundaries to the surface (Fig. 41). As the concentration of Si drops below some critical value, the constraints on the Ti-C layers on either side of the Si-layers are relaxed and the energetic advantages of the hexagonal stacking relative to the cubic one are diminished, rendering the latter more stable. In this context it is important to note that the removal of the Si atoms results in an untenable stacking sequence in which the Ti layers are directly on top of each other (Fig. 40b). The volume change associated with reaction VII is also $\approx$ 15 vol. % shrinkage. Initially when the Si loss is not too pronounced, the shrinkage is probably accommodated by a combination for very fine submicron cracks and possibly strains in the $Ti(C_{0.67},Si_{0.06})$ structure. If held for longer times, however, more Si is lost and the volume change becomes large enough that the reaction layer starts to break off into the molten bath.

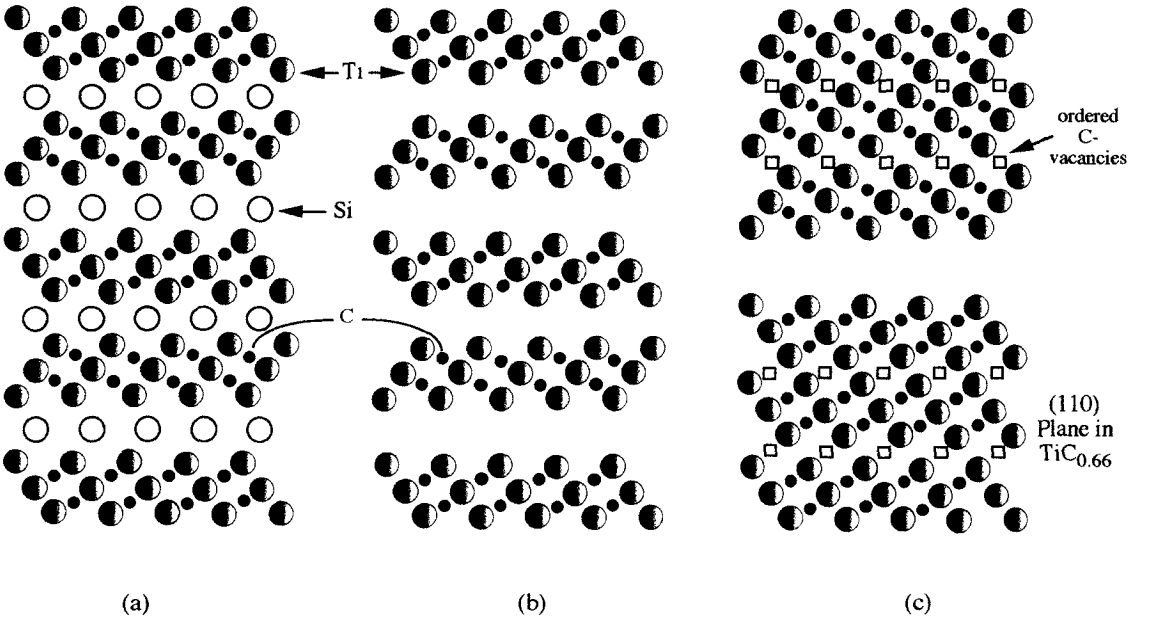

Figure 40: a) $(1\bar{2}10)$ plane in Ti_3SiC_2, where adjacent Ti_3C_2 layers are twins of each other. b) Same as a, but after loss of Si. c) Same as b, but after transformation that results in domains that are twins of each other. This structure is highly idealized in the sense that complete order is assumed.

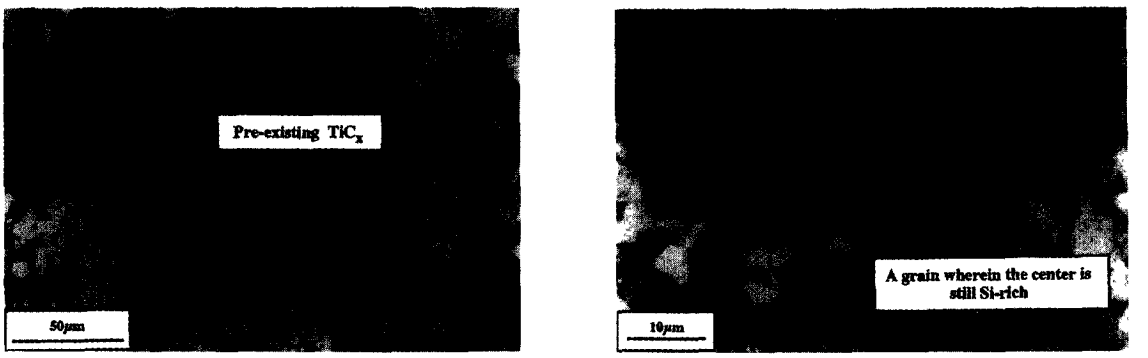

Figure 41: Polished and etched optical micrographs of Ti_3SiC_2 samples after immersion in cryolite at 960 °C. a) Reaction layer showing grain boundary nature of attack. This micrograph also shows the preferential removal of Si surrounding the pre-existing TiC_x particles. b) Higher magnification micrograph of reaction layer showing grains in which the center is Si-rich and the peripheries are Si-poor. Note that the Si diffuses first along basal planes and then along grain boundaries.

Reaction VII is important and of general validity because it explains several hitherto unexplained observations in the literature concerning Ti_3SiC_2. For example, Lis et al.[37] have reported that above 1450 °C, Ti_3SiC_2 transformed into what they termed a "TiC-like" phase for which the XRD patterns are similar to then ones we obtained. A similar reaction sequence has recently been proposed to explain the morphology of the TiC layers that form when SiC and Ti are reacted together[49]. Reaction VII could also explain the controversy concerning the presence or absence of Ti_3SiC_2 when Ti is reacted with SiC. If the temperatures are too high the Ti_3SiC_2 may form and then dissociate, especially in the presence of oxygen, leaving behind a partially ordered TiC_x.

Finally, it is important to note that it would be difficult, if not impossible, to synthesize $Ti(C_{0.67},Si_{0.06})$ by a solid-state reaction mechanism. This phase can only be synthesized by creating the ordered Ti_3SiC_2 structure first and then removing the Si atoms. Obviously, the lower the temperature the A-group element can be induced to diffuse out of the structures, the more ordered the remaining structure would be. These ordered structures may have some interesting and potentially useful properties and their synthesis and characterization should be pursued.

The reaction of Ti_3SiC_2 with molten Al is a further variation on the same theme[100]. The overall reaction is:

$$Ti_3SiC_2 + Al\ (l) \rightarrow 3\ TiC_x + \underline{Si}\ (Al) \qquad (VIII)$$

where $\underline{Si}$ is Si that is dissolved in the molten Al and x is most probably ≈ 0.67. The main evidence for the topotaxiality of the reaction is that the samples preserve their original shape and dimensions after the reaction. The reaction layer consists of two interconnected or interpenetrating networks of $TiC_{0.67}$ and molten Al. Consistent with this microstructure is the fact that the reaction kinetics are linear and given by:

$$K_x\ (m/s) = 7.16 \exp - (207\ kJ/RT) \qquad (22)$$

in the 800-1000 °C temperature range. The rate-limiting step is most probably the diffusion of Si from Ti_3SiC_2 into the liquid Al.

The foregoing discussion notwithstanding, not all reactions of Ti_3SiC_2 are topotactic; the latter are only expected when a chemical driving force exists for the outward diffusion of Si. Reaction of Ti_3SiC_2 with single crystal Si wafers resulted in the formation of a dense surface layer composed of a two-phase mixture of $TiSi_2$ and SiC[100]. The overall reaction is:

$$Ti_3SiC_2 + 7\ Si = 3\ TiSi_2 + 2\ SiC \qquad \Delta V = +\ 120\ \% \qquad (IX)$$

This layer grows in two distinct morphologies; an outer layer with fine (1-5 μm) SiC particles and an inner coarser (10-15 μm) one. The overall growth rates of the layers are parabolic, and significantly faster than the carburization kinetics (Fig. 39). Comparison with previously published results[207,208] supports the conclusion that diffusion of Si through $TiSi_2$ is rate limiting (Fig. 39).

The silicidation reaction is of major technological importance because as discussed above, despite the fact that the oxidation kinetics of Ti_3SiC_2 are parabolic, the activation energy for oxidation is high and at temperatures above $\approx$ 1400 °C, the reaction layers are relatively ($\approx$ 2-3 mm) thick. The silicidation improves the oxidation resistance (i.e. k_p) at 1400 °C by about 4 orders of magnitude[70,114], because now the protective layer that forms is pure silica.

8.3 Corrosion of Ti_3SiC_2 in Common Acids and NaOH

Based on extended (6 months) gravimetric measurements of Ti_3SiC_2 in dilute and concentrated sulfuric, H_2SO_4, nitric, HNO_3, and hydrochloric, HCl, acids the following conclusions were reached[105]:

- In dilute (13.6%) H_2SO_4 the weight loss is negligible, and corresponds to a corrosion rate of < 1 μm/yr. In concentrated (95 %) H_2SO_4 no weight changes were detectable. In other words, Ti_3SiC_2 is stable in H_2SO_4.
- The weight loss in dilute (7.6 %) HCl is also negligible and corresponds to a rate of < 2 μm/yr. In concentrated (38%) HCl, after an initial small weight loss, no further weight losses are detectable.
- The dissolution rates in dilute (6.4% and 11.6%) and concentrated (69.6%) HNO_3 are linear and orders of magnitude higher than in those in the other acids. Post-immersion SEM examination indicated that a porous SiO_2-based layer forms on the surface of the samples. This implies that the Ti atoms are leached out into the HNO_3 solution, leaving behind a Si-rich layer that is oxidized to SiO_2.
- At 5.5 μm/yr, the corrosion rate in dilute HF is also relatively low.
- No detectable weight losses were measurable after immersion in NaOH for up to 6 months.

Cyclic polarization scans established that Ti_3SiC_2 exhibits a resistance to pitting in H_2SO_4 and HCl at ambient conditions. The electrochemical results also strongly suggest that a very thin electrically insulating layer forms when the samples are immersed in HCl and H_2SO_4 acids. The presence of such a layer would explain the corrosion resistance of Ti_3SiC_2 in these acids.

9. POTENTIAL APPLICATIONS

Up to this point, the price one had to pay for high stiffness materials in general, and high specific stiffness in particular, and/or good mechanical properties at high temperatures, has been difficulty of machinability. With Ti_3SiC_2 and the other ternaries, this is no longer the case. It is worth noting here that if compounds with N > 3 exist, their stiffness could approach, or even exceed, those of the corresponding stoichiometric MX binaries, while maintaining the very important attribute of machinability. The machinability of metals is inextricably linked to their performance at higher temperature. The same mechanisms that render them useful at higher temperatures (i.e. obstacles in the way of the dislocations) are the ones that make them difficult to machine. The Ni-based superalloys are a case in point; they are difficult and expensive to machine. In Ti_3SiC_2, and the other $M_{N+1}AX_N$ phases, the machinability is de-coupled from the mechanical properties.

The ease of machinability is of great technological importance for three reasons. First, it allows for the fabrication of relatively cheap prototypes, which in turn, allows these materials to be tested for a variety of applications rapidly and cheaply. The second has to do with tolerances.

In many applications, such as engines, the tolerances required are more stringent than can be fabricated by a press and sinter process; a post-fabrication machining step is typically required. The advantages of the $M_{N+1}AX_N$ phases over other machinable ceramics, is that they are machinable *after* sintering - the latter have to be fired after machining which leads to a small shrinkage. The third has to do with joining. Joining ceramics to other materials is a non-trivial endeavor that is fraught with pitfalls. Machinability allows for alternate solutions. For example, tubes used by the petrochemical and chemical industries, can be quite long ($\approx$ 12 m) and would pose a veritable processing challenge for any traditional ceramic material that currently exists. Machinability greatly simplifies the problem: One or 2 m lengths of tubes would be extruded, their ends threaded and simply screwed together, end to end, to any desired length.

To date, very few, if any, ceramics, can withstand a thermal shock of greater than $\approx$ 1000 °C. The vast majority, including SiC and Si_3N_4, will, at best, survive thermal shocks of $\approx$ 500 °C. Here again the fact that Ti_3SiC_2 and the others are quite thermal shock resistant (Fig. 22), especially, if the grains are large is important.

The potential applications of Ti_3SiC_2 are myriad and far-reaching. Instead of listing or spelling out specific application we believe that Ti_3SiC_2, and possibly some of the other ternaries, could penetrate the following markets, or substitute for the following materials, amongst them are:

- Structural material for high temperature applications. The density of Ti_3SiC_2 is roughly half the density of currently Ni-based superalloys, roughly double their stiffness and most important possess very decent mechanical properties at temperatures that would render the best superalloys on the market today unusable. They are also much more readily machinable.
- Substitute for machinable ceramics. The advantages of using Ti_3SiC_2 over conventional machinable ceramics are several. The first is that the machinability is possible in the *final* i.e. fired state. Machinable ceramics require a sintering step after machining which results in a $\approx$ 2 % shrinkage.
- Kiln furniture. The attractive characteristics that make this application possible are: oxidation resistance, ease of machinability, relatively low cost of raw materials and, last but not least, excellent thermal shock and chemical resistances.
- Wear and corrosion protection. As noted above it is possible to carburize or silicide Ti_3SiC_2[70]. The former increases the surface hardness to 25 GPa; the latter to 12 GPa. These treated surfaces should in principle be quite wear and corrosion resistant. It follows that that parts can be readily and economically machined to close tolerances and only then surface treated to enhance the properties.
- Heat exchangers. Ti_3SiC_2 is an excellent thermal conductor with a conductivity that does not decrease much with increasing temperature. Taken together with its chemical stability, ease of machinability and resistance to thermal shock this application is obvious.
- Applications where rotating parts are used. The combination of high stiffness, low density and ease of machinability renders Ti_3SiC_2 excellent candidate materials for applications where dimensional stability while rotating is important, e.g. disk drives.

- If highly oriented samples of large enough single crystals could be grown, it may then be possible to exploit the very low friction coefficients of the basal planes where lubricity is important.

Finally in comparing this material with others, it is important to realize that these compounds are only "four" years old and that the properties reported herein are for the "pure" compounds. Very few materials indeed if any, are used in their "pure" state and as deeper understanding of these materials is gained it is not unreasonable to assume that major improvements, especially in the mechanical properties, are possible. That said, it is fair to say that when compared to other technologically important *materials at comparable* stages of development, there is little doubt that the prospects of these materials are quite promising. We are thus convinced that Ti_3SiC_2 and some of the other related compounds will be of immense technological importance in the years to come.

10. Outstanding Issues

There is little doubt that significant progress has been made in a relatively short time in understanding these layered ternary compounds. This does not mean that all the issues have been resolved. There are several issues that have either been glossed over or ignored in this review. The most intriguing are the HRTEM micrographs (Fig. 30f) that clearly show that, on average, the distance between dislocations in the walls is < 8 Å, the distance between the Si-planes. Hence all dislocations do not terminate at Si-planes, but some must terminate in the Ti-C layers. This observation is consistent with the observation that the Si concentration of fractured surfaces, as measured by XPS is less than the stoichiometric concentration, indicating that maybe the fracture occurs between the Ti and C planes rather than along the Ti-Si planes[73]. It is difficult to reconcile these observations with all other indications that clearly indicate that the Ti-C bonds are stronger than the Ti-Si bonds.

Another related question, whose answer may provide the clue to explaining the aforementioned observations, is why the dislocations are not pure edge, but contain a screw component[82].

The nature of the PBTT is also not totally understood. At this time, it is believed to be due to a recovery process in which dislocations are annihilated. What determines the recovery temperature is not clear. This is an important question because it would indicate the direction one need to follow to enhance the high temperature mechanical properties.

The fact that Ti_3SiC_2 and the others posses less that the requisite 5 independent slip systems required for ductility is important and has some far reaching ramifications. For example, these solids do not posses a yield point, and their behavior gradually transitions from brittle at lower temperatures and high strain rate, to plastic behavior at higher temperatures and lower strain rates.

11. Summary and Conclusions

The $M_{N+1}AX_N$ phases are a new class of solids that behave as true laminates at the nanolevel. They are machinable and thermodynamically stable to high temperatures; some as high as 2300 °C. The combination of metallic bonding, propensity for delaminations, and dislocation motion endows them with a unique and an unusual combination of properties, the most important and pervasive of which is damage tolerance. This damage tolerance is manifest in the creep, fatigue and tensile and compressive response. Thermally, elastically, chemically and electrically they share many of the advantageous attributes of their respective *stoichiometric* binary metal carbides or nitrides: they are elastically stiff, electrically and thermally conductive. Mechanically, however, they cannot be more different: they are readily machinable, relatively soft, resistant to thermal shock and unusually damage tolerant. They are the only polycrystalline solids that deform by a combination of kink and shear band formation, together with the delaminations of individual grains. Dislocations multiply and are mobile at room temperature glide exclusively on the basal planes and are overwhelmingly arranged either in arrays or kink boundaries. They combine ease of machinability with very decent mechanical properties, especially at $T > 1000$ °C. Furthermore, some of them, especially the ones with $N > 1$ couple thermal isotropy with mechanical anisotropy.

12. Acknowledgments

This paper and the remarkable advances we made over a relatively short time on both the scientific and technical fronts are due mostly to the talent, hard work and dedication of my colleague at Drexel University, Dr. T. El-Raghy and this paper would not have been possible without him. I would also like to acknowledge the excellent work and stimulating discussions I had will all my collaborators, especially, Dr. L. Faber, A. Zavaliangos, R. Doherty and S. Kalidindi. The support of Dr. L. Schioler of the Division of Materials Research of the National Science Foundation at critical junctures during the years is also gratefully acknowledged. I would also like to thank the Kanthal Corp. for their generous financial support.

13. References

1) H. Nowotny, "Struktuchemie Einiger Verbindungen der Ubergangsmetalle mit den elementen C, Si, Ge, Sn", Prog. Solid State Chem., H. Reiss, Ed., **2,** 27, (1970).
2) W. Jeitschko, H. Nowotny and F. Benesovsky, "Kohlenstoffhaltige ternare Verbindungen (H-Phase)", Monatsh. Chem., **94**, 672 (1963).
3) W. Jeitschko, H. Nowotny and F. Benesovsky, "Kohlenstoffhaltige ternare Verbindungen (V-Ge-C, Nb-Ga-C, Ta-Ga-C, Ta-Ge-C, Cr-Ga-C und Cr-Ge-C) ", Monatsh. Chem., **94**, 844 (1963).
4) W. Jeitschko, H. Nowotny and F. Benesovsky, "Ti_2AlN, eine Stickstoffhaltige H-Phase", Monatsh. Chem., **94**, 1198 (1963).
5) W. Jeitschko, H. Nowotny and F. Benesovsky, "Die H-Phasen: Ti_2CdC, Ti_2GaC, Ti_2GaN, Ti_2InN, Zr_2InN and Nb_2GaC, Monatsh. Chem., **95**, 178 (1964).
6) W. Jeitschko, H. Holleck, H. Nowotny and F. Benesovsky, "Phasen mit Aufgefulltem Ti_2Ni-Typ", Monatsh. Chem., **95**, 1004 (1964).
7) W. Jeitschko, H. Nowotny and F. Benesovsky, "Die H-phasen Ti_2TlC, Ti_2PbC, Nb_2InC, Nb_2SnC und Ta_2GaC", Monatsh. Chem., **95**, 431 (1964).
8) W. Jeitschko, H. Nowotny and F. Benesovsky, "Die H-phasen Ti_2InC, Hf_2InC und Ti_2GeC", Monatsh. Chem., **94**, 1201 (1963).
9) H. Boller and H. Nowotny, "Ronthenographische Untersuchungen in System: V-As-C", Monatsh. Chem., **97**, 1053 (1966).
10) E. Reiffenstein, H. Nowotny and F. Benesovsky, "Strukturchemische und magnetochemische Untersuchungen an Komplecarbiden", Monatsh. Chem., **97**, 1428 (1966).
11) W. Jeitschko and H. Nowotny, "Die Kristallstructur von Ti_3SiC_2 - Ein Neuer Komplxcarbid-Typ", Monatsh. fur Chem., **98**, 329-37 (1967).
12) H. Wolfsgruber, H. Nowotny and F. Benesovsky, "Die Kristallstuktur von Ti_3GeC_2", Monatsh. Chem., **98**, 2401 (1967).
13) O. Beckmann, H. Boller and H. Nowotny, "Neue H-Phasen", Monatsh. Chem., **99**, 1581 (1968).
14) H. Boller and H. Nowotny, "Die Kristallstruktur von V_2PC und V_5P_3N", Monatsh. Chem., **99**, 672 (1968).
15) . Beckmann, H. Boller, H. Nowotny and F. Benesovsky, "Einige Komplexcarbide und –nitride in den Systemen Ti-{Zn,Cd,Hg}-{C,N} und Cr-Ga-N", Monatsh. Chem. **100**, 1465 (1969).
16) O. Beckmann, H. Boller, H. Nowotny and F. Benesovsky, Monatsh. Chem., **100**, 1465 (1969).
17) H. Nowotny and S. Windisch, Annual Review of Materials Science, Eds. R. Huggins, R. Bube and R. Roberts. Annual Review Inc., Palo Alto, CA. **3**, 171 (1973).
18) J. C. Schuster, H. Nowotny and C. Vaccaro, "The Ternary Systems: Cr-Al-C, V-Al-C and Ti-Al-C and the Behavior of the H-phases (M_2AlC)", J. of Solid State Chem., **32**, 213 (1980).

19) M. A. Pietzka and J. C. Schuster, "Summary of Constitution Data of the System Al-C-Ti," J. Phase Equilibria, **15**, 392 (1994).

20) M. A. Pietzka and J. C. Schuster, "The Ternary Boundary Phases of the Quaternary System Ti-Al-C-N"; in *Concerted Action on Materials Science,* Leuven Proceedings, Part A, Commission of the European Communities, Brussels, Belgium, 1992.

21) V. I. Ivchenko, M. I. Lesnaya and V. F. Nemchenko and T. Y. Kosolapova, "Prepararion and Some Properties of the Ternary Compound Ti_2AlN", Porosh. Metall., **160**, 60 (1976).

22) V. I. Ivchenko and T. Y. Kosolapova, "Conditions of Preparation of Ternary Ti-C-Al alloy Powders", Porosh. Met., **150**, 1 (1975).

23) V. I. Ivchenko, M. I. Lesnaya and V. F. Nemchenko and T. Y. Kosolapova, "Some Physical Properties of Ternary Compounds in the System Ti-Al-C", Porosh. Metall., **161**, 45 (1976).

24) V. I. Ivchenko and T. Y. Kosolapova, "Abrasive Properties of the Ternary Compounds in the System Ti-Al-C and Ti-Al-N", Porosh. Met., **164**, 56 (1976).

25) J. J. Nickl, K. K. Schweitzer and P. Luxenberg, "Gasphasenabscheidung im Systeme Ti-C-Si" J. Less Common Metals, **26**, 283 (1972).

26) T. Goto and T. Hirai, "Chemically Vapor Deposited Ti_3SiC_2", Mat. Res. Bull., **22**, 1195 (1987).

27) C. Racault, F. Langlais, R. Naslain and Y. Kihn, "Chemically Vapor Deposition of Ti_3SiC_2 from $TiCl_4$-$SiCl_4$-CH_4-H_2 Gas Mixtures", J. Mater. Sci., **29,** 3941 (1994).

28) C. Racault, F. Langlais and C. Bernard, "On the Chemical Vapor Deposition of Ti_3SiC_2 from $TiCl_4$-$SiCl_4$-CH_4-H_2 Gas Mixtures: Part II an experimental approach", J. Mater. Sci., **29**, 5023 (1994).

29) E. Pickering, W. J. Lackey and S. Crain, "Microstructure of Ti_3SiC_2 Coatings Synthesized by CVD", Ceram. Trans. **96**, Advances in Ceramic Matrix Composites IV, Eds. J. P. Singh and N. Bansal, 1999.

30) C. E. Bruckl, "Ternary Phase Equilibria in Transition Metal-B-C-Si Systems", AFML-TR-65-2-Part II, Vol. VII, Air Force Materials Laboratory, Wright-Patterson Air Force Base, Ohio, 1966.

31) S. Arunajatesan, A. Carim, "Synthesis of Ti_3SiC_2", J. Amer. Cer. Soc., **78**, 667 (1995).

32) C. Racault, F. Langlais and R. Naslain, "Solid State Synthesis and Characterization of the Ternary Phase Ti_3SiC_2, J. Mater. Sci., **29**, 3384 (1994).

33) R. Pampuch, J. Lis, L. Stobierski and M. Tymkiewicz, "Solid Combustion Synthesis of Ti_3SiC_2", J. Eur. Ceram. Soc., **5**, 283 (1989).

34) J. Lis, P. Pampuch and L. Stobieski, "Reactions During SHS in a Ti-Si-C System", Int. J. of Self-Propagating High-Temp. Synth., **1**, 401 (1992).

35) R. Pampuch, J. Lis, J. Piekarczyk and L. Stobierski, "Ti_3SiC_2-Based Materials Produced by Self-Propagating High Temperature Synthesis and Ceramic Processing", J. Mater. Synth. Process., **1**, 93 (1993).

36) J. Lis, R. Pampuch, J. Piekarczyk and L. Stobierski, "New Ceramics Based on Ti_3SiC_2", Ceramics Inter., **19**, 219 (1993).

37) J. Lis, Y. Miyamoto, R. Pampuch and K. Tanihata, "Ti_3SiC_2-Based Materials Prepared by HIP-SHS Techniques", Mater. Lett., **22**, 163-68 (1995).

38) J. Morgiel, J. Lis and R. Pampuch, "Microstructure of Ti_3SiC_2-based Ceramics", Mater. Lettrs., **27**, 85 (1996).

39) T. Okano, T. Yano and T. Iseki, "Synthesis and Mechanical Properties of Ti_3SiC_2 Ceramic", Trans. Met. Soc. Jpn., **14A,** 597 (1993).

40) X. Tong, T. Okano, T. Iseki and T. Yano, "Synthesis and High Temperature Mechanical Properties of Ti_3SiC_2/SiC Composites", J. Mater. Sci., **30,** 3087 (1995).

41) J. Panczyk, T. Niemyski, L. N. Vniogradov and V. S. Sinel'nikova," Production of Ti_3SiC_2 from the Gas Phase and Some Chemical and Physical Properties," (in polish), Szklo Ceram., **23**, 144 (1972): Chem. Abs. **77**, (1972) 64084c.

42) T. Iseki, T. Yano, Y-S. Chung, "Wetting and Properties of Reaction Products in Active Metal Brazing of SiC", J. Cer. Soc. Jap. (Inter. Ed.), **97**, 47 (1990).

43) M. W. Barsoum and T. El-Raghy, "Synthesis and Characterization of a Remarkable Ceramic: Ti_3SiC_2 ", J. Amer. Cer. Soc., **79**, 1953 (1996).

44) M. W. Barsoum and T. El-Raghy, "A Progress Report on Ti_3SiC_2, Ti_3GeC_2 and the H-Phases, M_2BX", J. Mater. Synth. Process., **5**, 197-216 (1997).

45) R. Radhahrishnan, J. J. Williams and M. Akinc, "Synthesis and Stability of Ti_3SiC_2", J. Alloy. Compounds, **285**, 85 (1999).

46) Y. Du, J. C. Schuster, H. Seifert and F. Aldinger, "Experimental Investigation and Thermodynamic Calculation of the Titanium-Silicon-Carbon System", J. Amer. Cer. Soc., **83**, 197-203 (2000).

47) S. Morozumi, M. Endo, M. Kikuchi and K. Hamajima, "Bonding Mechanism Between SiC and Thin Foils of Reactive Metals", J. Mater. Sci., **20**, 3976 (1985).

48) W. J. J. Wakelkamp, F. J. van Loo and R. Metselaar, "Phase Relations in the Titanium-Silicon-Carbon System," J. Europ. Cer. Soc., **8**, 135 (1991).

49) M. W. Barsoum, "Comment on 'Reaction Layers Around SiC Particles in Ti: an Electron Microscopy Study'", Scripta Mater., **43**,285-86 (2000).

50) B. J. Kool, M. Kabel, A. B. Kloosteerman and J. Th. M. DeHosson, "Reaction Layers around SiC Particles in Ti: An Electron Microscope Study", Acta Mater., **47**, 3105 (1999).

51) P. Martineau, P. Pailler, M. Lahaye and R. Naslain, "SiC Filament/titanium matrix Composites Regarded as Model Composites. Part 2. Fiber/matrix chemical interactions at high temperatures", J. Mater. Sci., **19**, 2749-70 (1984).

52) J. L. Ratliff and G. W. Powell, "Research on Diffusion in Multiphase Ternary Systems", AFML-TR-70-42, U.S. Department of Commerce, Alexandria,VA, (1970).

53) B. Gottselig, E. Gyarmati, A. Naoumidis, & H. Nickel, J. Europ. Ceram. Soc., **6**, 153 (1990).

54) T. N. Baker, H. Xin, C. Hu and S. Mridha, Mater. Sci Technol., **10**, 536 (1994).

55) M. Backhaus-Ricoult, Ber. Bunsenges. Phys. Chem., **93**, 1277 (1989).

56) S. Mridha and T. N. Baker, Mater. Sci Technol., **12**, 595 (1996).
57) S. K. Choi, M. Chandraasekan and M. J. Brabers, J. Mater. Sci., **25**, 1975 (1990).
58) J. H. Abboud and D. R. F. West, Mater. Sci. Technol., **5**, 725 (1989).
59) F. Goesmann, R. Wenzel and R. Schmid-Fetzer, J. Mater. Sci.: Mater. in Electronics, **9**, 109 (1998).
60) M. W. Barsoum, L. Farber, I. Levin, A. Procopio, T. El-Raghy and A. Berner, "HRTEM of Ti_4AlN_3; or $Ti_3Al_2N_2$ Revisited", J. Amer. Cer. Soc., **82**, 2545-2547 (1999).
61) A. T. Procopio, T. El-Raghy and M. W. Barsoum, "Synthesis of Ti_4AlN_3 and Phase Equilibria in the Ti-Al-N System", Met. Mater. Trans. **31A**, 373 (2000).
62) A. T. Procopio, M. W. Barsoum and T. El-Raghy, "Characterization of Ti_4AlN_3", Met. Mater. Trans. **31A,** 333 (2000).
63) C. J. Rawn, M. W. Barsoum, T. El-Raghy, A. Procopio, C. M. Hoffmann and C. Hubbard, "Structure of Ti_4AlN_{3-x}- a Layered $M_{n+1}AX_n$ Nitride", Mater. Res. Bull. in press.
64) T. El-Raghy and M. W. Barsoum, "Processing and Mechanical Properties of Ti_3SiC_2: Part I: Reaction Path and Microstructure Evolution", J. Amer. Cer. Soc., **82,** 2849-54 (1999).
65) M. W. Barsoum, D. Brodkin and T. El-Raghy, "Layered Machinable Ceramics For High Temperature Applications", Scrip. Met. et. Mater., **36**, 535 (1997).
66) T. El-Raghy, A. Zavaliangos, M. W. Barsoum and S. Kalidinidi, "Damage Mechanisms Around Hardness Indentations in Ti_3SiC_2", J. Amer. Cer. Soc., **80,** 513-516, (1997).
67) M. W. Barsoum, T. El-Raghy and L. Ogbuji, "Oxidation of Ti_3SiC_2 in Air", J. Electrochem. Soc.,**144**, 2508 (1997).
68) M. W. Barsoum and J. C. Schuster, "Comment on "New Ternary Nitride in the Ti-Al-N System", J. Amer. Cer. Soc. **81**, 785 (1998).
69) M. W. Barsoum, G. Yaroschuck and S. Tyagi, "Fabrication and Characterization of M_2SnC (M = Ti, Zr, Hf and Nb)", Scrip. Mater., **37**, 1583 (1997).
70) T. El-Raghy and M. W. Barsoum, "Diffusion Kinetics of the Carburization and Silicidation of Ti_3SiC_2 ", J. Appl. Phys., **83**, 112-119 (1998).
71) I. M. Low, S. K. Lee, B. Lawn and M. W. Barsoum, "Contact Damage Accumulation in Ti_3SiC_2", J. Amer. Cer. Soc., **81**, 225-28 (1998).
72) L. Farber, M. W. Barsoum, A. Zavaliangos, T. El-Raghy and I. Levin, "Dislocations and Stacking Faults in Ti_3SiC_2", J. Amer. Cer. Soc., **81**, 1677-81 (1998).
73) E. H. Kisi, J. A. A. Crossley, S. Myhra and M. W. Barsoum, "Structure and Crystal-Chemistry of Ti_3SiC_2", J. Phys. Chem. Sol., **59**, 1437-1443 (1998).
74) S. Myhra, J. A. A. Crossley and M. W. Barsoum, "Crystal-chemistry of the Ti_3AlC_2 and Ti_4AlN_3 Layered Carbide/Nitride Phases-Characterization by XPS", ibid; in press.
75) M. Amer, M. W. Barsoum, T. El-Raghy, I. Wiess, S. LeClair and D. Liptak, "Raman Spectrum of Ti_3SiC_2", J. Appl. Phys., **84**, 5817-5819 (1998).
76) M. W. Barsoum and T. El-Raghy, "Room Temperature Ductile Carbides", Met. Mater. Trans., **30A,** 363-369 (1999).

77) M. W. Barsoum, T. El-Raghy, C. J. Rawn, W. D. Porter, H. Wang, A. Payzant and C. Hubbard, "Thermal Properties of Ti_3SiC_2", J. Phys. Chem. Solids, **60**, 429-439, (1999).

78) M. Gamarnik and M. W. Barsoum, "Bond Lengths in the Ternary Compounds Ti_3SiC_2, Ti_3GeC_2 and Ti_2GeC", J. Mater. Science, **34**, 169-174 (1999).

79) S. M. El-Raghy, A. F. Waheed, T. S. El-Raghy and M. W. Barsoum, "Preliminary Report on the Electrochemical Behavior of Ti_3SiC_2", J. Mat. Sci. Lett., **18**, 519-520, (1999).

80) M. W. Barsoum, L. Farber, "Room Temperature De-Intercalation and Self-Extrusion of Ga from Cr_2GaN", Science, **284,** 937-939 (1999).

81) T. El-Raghy and M. W. Barsoum, "Growing Metallic Whiskers: An Alternative Interpretation", Science, **285**, 1355, (1999).

82) L. Farber, I. Levin and M. W. Barsoum, "HRTEM Study of a Low-Angle Boundary in Plastically Deformed Ti_3SiC_2", Phil. Mag. Letters., **79**, 163 (1999).

83) P. Finkel, M. W. Barsoum and T. El-Raghy, "Low Temperature Dependence of Elastic Properties of Ti_3SiC_2", J. Appl. Phys., **85**, 7123-7126 (1999).

84) M. W. Barsoum, L. Farber and T. El-Raghy, "Dislocations, Kink Banks and Room Temperature Plasticity of Ti_3SiC_2", Met. Mat. Trans., **30A,** 1727-1738 (1999).

85) L. Farber and M. W. Barsoum, "Isothermal Sections in the Cr-Ga-N System in the 650-1000 °C Temperature Range", J. Mater. Res., **14**, 2560-2566 (1999).

86) T. El-Raghy, M. W. Barsoum, A. Zavaliangos and S. Kalidindi, "Processing and Mechanical Properties of Ti_3SiC_2, Part II: Effect of Grain Size and Deformation Temperature", J. Amer. Cer. Soc., **82**, 2855-2859 (1999).

87) J. C. Ho, H. H. Hamdeh, M. W. Barsoum and T. El-Raghy, "Low Temperature Heat Capacity of Ti_3SiC_2", J. Appl. Phys., **85**, 7970-7971 (1999).

88) J. C. Ho, H. H. Hamdeh, M. W. Barsoum and T. El-Raghy, "Low Temperature Heat Capacities of $Ti_3Al_{1.1}C_{1.8}$, Ti_4AlN_3 and Ti_3SiC_2", J. Appl. Phys., **86,** 3609-3611 (1999).

89) L. Farber, I. Levin, M. W. Barsoum, T. El-Raghy and N. Tzenov, "HRTEM of Some $Ti_{n+1}AX_n$ Compounds (n = 1,2; A = Al or Si; X = C or N)", J. Appl. Phys., **86**, 2543-2540 (1999).

90) M. W. Barsoum, T. El-Raghy, L. Farber, M. Amer, R. Christini and A. Adams, "The Topotaxial Transformation of Ti_3SiC_2 To Form a Partially Ordered Cubic $TiC_{0.67}$ Phase by the Diffusion of Si into Molten Cryolite", J. Electrochem. Soc., **146**, 3919-3923 (1999).

91) P. Finkel, M. W. Barsoum and T. El-Raghy, "Low Temperature Dependencies of the Elastic Properties of $Ti_3Al_{1.1}C_{1.8}$, Ti_4AlN_3 and Ti_3SiC_2", J. Appl. Phys., **87**, 1701-3 (2000)

92) T. El-Raghy, P. Blau and M. W. Barsoum, "Effect of Grain Size on Friction and Wear Behavior of Ti_3SiC_2", Wear, **238**, 125-130 (2000).

93) N. Tzenov, M. W. Barsoum and T. El-Raghy, "Influence of Small Amounts of Fe, and V on the Synthesis and Stability of Ti_3SiC_2", J. Europ. Cer. Soc. **20**, 801-806 (2000).

94) M. Radovic, M. W. Barsoum, T. El-Raghy, J. Seidensticker and S. Wiederhorn, "Tensile Properties of Ti_3SiC_2 in the 25-1300 °C Temperature Range", Acta Mater. 48, 453-459 (2000).

95) C. J. Gilbert, D. R. Bloyer, M. W. Barsoum, T. El-Raghy, A. P. Tomsia and R. O. Ritchie, "Fatigue-Crack Growth and Fracture Properties of Coarse and Fine-Grained Ti_3SiC_2", Scripta Mater., **42**, 761-767 (2000).

96) N. Tzenov and M. W. Barsoum, "Synthesis and Characterization of $Ti_3AlC_{1.8}$", J. Amer. Cer. Soc., **83**, 825 (2000).

97) M. W. Barsoum, M. Ali and T. El-Raghy, "Processing and Characterization of Ti_2AlC, Ti_2AlN and $Ti_2AlC_{0.5}N_{0.5}$", Met. Mater. Trans., **31A**, 1857-65 (2000).

98) M. W. Barsoum, C. J. Rawn, T. El-Raghy, A. Procopio, W. D. Porter, H. Wang and C. R. Hubbard, "Thermal Properties of Ti_4AlN_3", J. Appl. Phys. **87**, 8407-14 (2000).

99) T. El-Raghy, S. Chakraborty and M. W. Barsoum, "Synthesis and Characterization of Hf_2PbC, Zr_2PbC and M_2SnC (M = Ti, Hf, Nb or Zr)", J. Europ. Cer. Soc. in press.

100) T. El-Raghy, M. W. Barsoum and M. Sika, "Reaction of Al with Ti_3SiC_2 in the 800–1000 °C Temperature range", Mater Sci. Eng. A, in press.

101) H-I. Yoo, M. W. Barsoum and T. El-Raghy, "Ti_3SiC_2 Has Negligible Thermopower", Nature, **407**, 581-82 (2000).

102) M. W. Barsoum, H.-I. Yoo, I. K. Polushina, V. Yu. Rud', Yu. V. Rud' and T. El-Raghy, "Electrical Conductivity, Thermopower and Hall Effect of Ti_3AlC_2, Ti_4AlN_3 and Ti_3SiC_2", Phys. Rev. B, in press.

103) M. W. Barsoum, T. El-Raghy, W. D. Porter, H. Wang, J. C. Ho and S. Chakraborty, "Thermal Properties of Nb_2SnC", J. Appl. Phys., in press.

104) M. W. Barsoum, T. El-Raghy, C. Rawn, W. D. Porter and H. Wang, "Electrical and Thermal Properties of Ti_2AlC", Submitted for publication.

105) J. Travaglini, MSc. Theses, Drexel University, June 2000.

106) M. Radovic, M. W. Barsoum, T. El-Raghy and S. Wiederhorn, "Tensile Creep of Fine-Grained Ti_3SiC_2 in the 25-1200 °C Temperature Range", Submitted for publication.

107) M. Radovic, M. W. Barsoum, T. El-Raghy and S. Wiederhorn, "Tensile Properties of Coarse-Grained Ti_3SiC_2 in the 25-1200 °C Temperature Range", Submitted for publication.

108) M. W. Barsoum, "Oxidation of $Ti_{n+1}AlX_n$ where n = 1-3 and X is C, N, Part I: Model", Submitted for publication.

109) M. W. Barsoum, M. Ali and T. El-Raghy, "Oxidation of $Ti_{N+1}AlX_N$ where n = 1-3 and X is C, N, Part II: Oxidation of Ti_2AlC, Ti_2AlN and $Ti_2AlC_{0.5}N_{0.5}$", Submitted for publication.

110) N. Tzenov, A. Procopio, T. El-Raghy and M. W. Barsoum, "Oxidation of $Ti_{N+1}AlX_N$ where n = 1-3 and X is C, N, Part III: Oxidation of Ti_3AlC_2 and Ti_4AlC_3". Submitted for publication.

111) M. Amer, T. El-Raghy, M. W. Barsoum, "Raman Spectra of Ti_2AlN and Ti_4AlN_3", Unpublished results.

112) M. W. Barsoum and T. El-Raghy, "Process for Making a Dense Ceramic Work-Piece." Patent # 5,882,561.

113) M. W. Barsoum, T. El-Raghy, D. Brodkin, A. Zavaliangos and S. Kalidindi, "Synthesis of 312 Compounds and Composites Thereof", Patent # 5,942,455.

114) M. W. Barsoum and T. El-Raghy, "Surface Modification of 312 and Related Materials", Patent # 6,013,322.

115) J. C. Schuster and J. Bauer, "The Ternary System Ti-Al-N", J. Solid. St. Chem., **53**, 260 (1984).

116) K. Cenzual, L. M. Gelato, M. Penzo and E. Parthe, Acta Crystallogr. "Inorganic Structure Types with Revised Space Groups", **B47**, 433 (1991).

117) H. D. Lee and W. Petuskey, "New Ternary Nitride in the Ti-Al-N System", J. Amer. Cer. Soc., **80**, 604 (1997).

118) D. Shechtman, D. Van Heerden and D. Josell, "FCC Titanium in Ti-Al Multilayers", Mater. Lett., **20**, 10 (1994).

119) T. Tepper, D. Shechtman, D. Van Heerden and D. Josell, "FCC Titanium in Ti/Ag multilayers", Mater. Lett., **33**, 181 (1997).

120) T. Tepper, D. Shechtman, D. Van Heerden and D. Josell, "Allotropic Phase Formation in Ti/Zr Multilayers", Mater. Lett., **35**, 100 (1998).

121) S. A. Dregia, R. Banerjee and H. L. Fraser, "Polymorphic Phase Stability in Thin Multilayers", Scripta Mater., **39**, 217 (1998).

122) R. Banerjee, R. Ahuja and H. L. Fraser, "Dimensionally-Induced Structural Transformations in Ti-Al multilayers", Phys. Rev. Lett., **76**, 3778 (1996).

123) D. Van Heerden, D. Josell and D. Shechtman, "The Formation of FCC Titanium in Ti-Al Multilayers", Acta Mater., **44**, 297 (1996).

124) A. Cottrell, *Chemical Bonding in Transition Metal Carbides*, Institute of Mater., Cambridge, 1995

125) M. A. Pietzka and J. C. Schuster, "Phase Equilibria in the Quaternary System Ti-Al-C-N", J. Amer. Cer. Soc., 79, 2321 (1996).

126) H. Nowotny, P. Rogl and J. Schuster, "Structural Chemistry of Complex Carbides and Related Compounds", J. Solid. St. Chem., **44**, 126 (1982).

127) O. Beckmann, Thesis, Univ. of Vienna, (1970).

128) J. S. Kephart and A. H. Carim, "Ternary Compounds and Phase Equilibria in Ti-Ge-C and Ti-Ge-B", J. Electrochem. Soc., **145**, 3253 (1998).

129) J. L. Calais, "Band Structure of Transition Metal Compounds", Adv. Phys., **26,** 847 (1977).

130) K. Schwarz, "Band Structure and Chemical Bonding in Transition Metal Carbides and Nitrides", in CRC Critical Reviews in Solid State and Materials Science, **13**, 211 (1987).

131) A. Neckel, "Electronic Structure of Stoichiometric and Non- Stoichiometric TiC and TiN", in *The Physics of Carbides and Nitrides and Borides*, R. Freer Ed., Kluwer Academic Press, Amsterdam, 485 (1990).

132) R. G. Lye and E. M. Logothetis, "Optical Properties and Band Structure of TiC", Phys. Rev., **147**, 622 (1966).

133) N. Medvedeva, D. Novikov, A. Ivanovsky, M. Kuznetsov, and A. Freeman, "Electronic Properties of Ti_3SiC_2–Based Solid Solutions", Phys. Rev. B, **58**, 16042 (1998).

134) N. I. Medvedeva and A. L. Ivanovskii, "Electronic Structure and Chemical Bonding in Hexagonal Ti, Zr and Vanadium Silicocarbides", Russ. J. Inorgan. Chem., **43**, 398 (1998).

135) A. Ivanovskii and N. I. Medvedeva, "Electronic Structure of Hexagonal Ti_3AlC_2 and Ti_3AlN_2", Mendeleev Commun., p.36 (1999).

136) Z. M. Sun and Y. C. Zhou, "Ab initio calculation of Ti_3SiC_2", Phys. Review B, **60** 1441 (1999).

137) Y. C. Zhou and Z. M. Sun, "Electronic Structure and Bonding Properties of Layered Machinable Ti_2AlC and Ti_2AlN ", Phys. Rev. B, **61** 12570 (2000).

138) Y. C. Zhou and Z. M. Sun, "Electronic Structure and Chemical Bonding of Ti_3GeC_2", J. Mater. Chem., **10**, 343 (2000).

139) A. N. Christensen, "Temperature Factor Parameters of Some Transition Metal Carbides and Nitrides by Single Crystal X-ray and Neutron Diffraction", Acta. Chem. Scand., **A32**, 89 (1978).

140) G. V. Samsonov, *High Temperature Materials: Vol. 2, Properties Index*; Plenum Press, NY, 1964.

141) C. H. MacGillavry, G. D. Rieck, K. Lonsdale, *International Tables for X-ray Crystallography*, Kynoch Press, Birmingham, Vol. III. (1962).

142) L. E. Toth, *Transition Metal Carbides and Nitrides*, Academic Press, NY, 1971.

143) E. W. Collings and J. C. Ho, "Magnetic Susceptibility and Low-temperature Specific Heat Studies of Ti, Zr, and Hf", Phys. Rev. B, **4**, 349-56 (1971).

144) Electronic Structures Database, http://cst-www.nrl.navy.mil/esdata/database.html.

145) M.W. Chase, C.A. Davies, J. R. Downey, D.J. Frurip, R. A. McDonald and A. N. Syverud, JANAF Thermodynamic Tables, Third Ed., J. Phys. Chem. Ref. Data, **14**, Supp. 1 (1985).

146) S. Sambasivan, PhD Thesis, (1990), Dept. of Chemistry, Arizona State Univ., Tempe, AZ.

147) F. A. Modine, M. D. Foegelle, C. B. Finch and C. Y. Allison, "Electrical Properties of Transition Carbides of Group IV", Phys. Rev. B, **40**, 9558 (1989).

148) L. Y. L. Shen, N. M. Senozan and N. E. Philips, Phys. Rev. Lett., **14**, 1025 (1965).

149) H. Pierson, *Handbook of Refractory Carbides and Nitrides*, Noyes Publications, Westwood, NJ. 1996.

150) R. E. Taylor, "Thermal Conductivity of TiC at High Temperatures", J. Amer. Cer. Soc., **44**, 525 (1961).

151) W. Lengauer, S. Binder, K. Ainger, P. Ettmayer, A. Gillou, J. Debuigne, G. Groboth, "Solid State Properties of Group IVb Carbonitrides", J. Alloys Compounds, **217**, 137 (1995).

152) R. E. Taylor, "Thermal Conductivity of ZrC at High Temperatures", J. Amer. Cer. Soc., **45**, 345 (1962).

153) W. S. Williams, "Transition-Metal Carbides", Prog. Solid State Chem., Eds. H. Reiss and J. O. McCaldin, **6**, 57, (1971).

154) L. G. Radosevich and W. S. Williams, "Phonon Scattering by Conduction Electrons and by Lattice Vacancies in Carbides of the Transition Metals", Phys. Rev., **188**, 770 (1969).

155) V. Keppens, D. Mandrus, B. C. Sales, B. C. Chakoumakos, P. Dai, R. Coldea, M. B. Maple, D. A. Gajewski, E. J. Freeman and S. Bennington, "Localized vibrational modes in metallic solids", Nature, **395**, 876 (1998).

156) B. C. Sales, B. C. Chakoumakos and D. Mandrus, J. W. Sharp, "Atomic Displacement Parameters and the Lattice Thermal Conductivity of Clatharate Thermoelectric Compounds", J. Solid State Chem., **146**, 528 (1999).

157) J.-F. Li, F. Sato and R. Watanabe, "Synthesis of Ti_3SiC_2 Polycrystals by Hot Isostatic Pressing of Elemental Powders", J. Mater. Sci. Lett., **18**, 1595 (1999).

158) T. Hirano and M. Kaise, "Electrical Resistivites of Single-Crystalline Transition-Metal Disilicides", J. Appl. Phys., **68**, 627 (1990).

159) T. Berlincourt, "Hall Effect, Resistivity and Magnetoresistivity of Th, U, Zr, Ti and Nb", Phys. Rev. **114**, 969 (1959).

160) E. W. Collings, "Anomalous Electrical Resistivity, bcc Phase Stability and Superconductivity in Ti-V Alloys", Phys. Rev. B, **9**, 3989 (1974).

161) G. Scovil, "The Hall Effect in Ti", Phys. Rev., **107**, 1513 (1957).

162) W. S. Willams, Phys. Rev. A, **135**, 505 (1964).

163) H. W. Worner, "Thermoelectric Properties of Ti with Special Reference to the Allotropic Transformation", Australian J. of Scientific Instrum., **4**, 62 (1951).

164) J. Piper, "Hall Effect in Single Crystal TiC", J. Appl. Phys., **33**, 2394 (1962).

165) O. A. Golikova, F. L. Feigel'man, A. I. Avustinik, and G. M. Klimashin, "Hall Effect in TiC at High Temperatures", Soviet Physics-Semiconductors, **1**, 236 (1967).

166) A. Onodera, H. Hirano, T. Yuasa, N. F. Gao and Y. Miyamoto, "Static Compression of Ti_3SiC_2 to 61GPa", Appl. Phys. Letters, **74**, 3782 (1999).

167) A. H. Chokshi, A. K. Mukherjee and T. G. Langdon, Mat. Sci. and Eng., **R10**, 237 (1993).

168) T. G. Langdon in Superplasticity in Aerospace Materials II, Eds. T. R. McNelly and H. C. Heikkenen, The Minerals, Metals and Materials Society, (1990).

169) F. Wakai, Y. Kodoma and T Nagano, Jap. J. Appl. Phys., **2.**, 57 (1989).

170) L. A. Xue and I-W. Chen, "Superplastic Alumina at Temperatures below 1300 °C Using Charge Compensating Dopants", J. Am. Ceram. Soc., **79**, 233 (1996).

171) T. G. Nieh, C. M. McNally and J. Wadsworth, "Superplastic Properties of a Fine-grained Yttria-Stabilized Tetragonal Polycrystal of Zirconia", Script. Met., **22**, 1297 (1988).

172) P. Finkel, M. W. Barsoum and T. El-Raghy, "Acoustic Emission and Damage Tolerance of Ti_3SiC_2 under Compression", Submitted for pub.

173) Y. C. Zhou and Z. M. Sun, "Microstructure and Mechanism of Damage Tolerance for Ti_3SiC_2 Bulk Ceramics", Material Research Innovations, **2**, 360 (1999).

174) I. M. Low, Vickers Contact Damage of Micro-layered Ti_3SiC_2", J. Europ. Cer. Soc., **18**, 709 (1998).

175) T. El-Raghy, PhD Thesis, Drexel University, June 1997.

176) R. F. Cook, B. R. Lawn, and C. J. Fairbanks, "Microstructure-Strength Properties in Ceramics: I Effect of Crack Size on Toughness", J. Amer. Ceram Soc., **68**, 604, (1985).

177) V. Petrenko and R. Whitworth, Physics of Ice, Oxford Univ. Press, 1999. .

178) S. Myhra, J. W. B. Summers and E. H. Kisi, "Ti_3SiC_2–A Layered Ceramic Exhibiting Ultra-Low Friction", Materials Letters, **39**, 6 (1999).

179) A. Crossley, E. Kisi, J. W. B. Summers and S. Myhra, "Ultra-low Friction for a Layered Carbide Derived Ceramic, Ti_3SiC_2, Investigated by Lateral Force Microscopy", J. Phys. D: Appl. Phys., **32**, 632 (1999).

180) G. E. Hollox and R. E. Smallman, "Plastic Behavior of TiC", J. Appl. Phys., **37**, 818 (1966).

181) E. Orowan, Nature, "A Type of Plastic Deformation New In Metals", **149**, 463 (1942).

182) J. B. Hess and C. S. Barrett, "Structure and Nature of Kink Bands in Zinc", Trans. AIME, **185**, 599 (1949).

183) E. G. Tapetado, M. H. Loretto, Phil. Mag., **30**, 515 (1974).

184) M.S. Patterson and L.E. Weiss, Geolg. Soc. Amer. Bull., **77**, 343 (1966).

185) O. Mugge, Neues Jarrb. f. Miner., **1**, 71 (1898).

186) N. C. Gay and L. E. Weiss, Tectonphysics, **21**, 287, (1974).

187) E. Honea and A. M. Johnson, Tectonphysics, **30**, 197 (1976).

188) R. E. Robertson, J. Polymer Sci., **A-27**, 1315 (1980).

189) S. DeTeresa, R. Porter and R. Farris, J. Mater. Sci., **23**, 1886 (1988).

190) D. A. Zaukelies, J. Appl. Phys, **33**, 2797 (1962).

191) G. E. Attenburrow and D. C. Bassett, J. Mater. Sci., **14**, 2679 (1979).

192) A. Keller and J. G. Rider, J. Mater. Sci., **1**, 389 (1966).

193) C. T. Keith and W. A. Cote Jr., Forest Prod. J., **18**, 67 (1968).

194) H. M. Hathorne and E. Teghtsoonian, J. Mater. Sci., **10**, 41 (1975).

195) W. R. Jones and J. W. Johnson, Carbon, **9**, 645 (1971).

196) V. Gupta, K. Anand and M. Kryska, Acta. Mater., **42**, 781 (1994).

197) C. W. Weaver and J. G. Williams, J. Mater. Sci., **10**, 1323 (1975).

198) A. S. Argon, Treatise Mater. Sci. Technol., **1**, 79, (1972).

199) G. R. Edwards, J. Shyne and O. Sherby, "Strain Softening in Powder Metallurgy Zinc", Met. Trans., **2**, 2955 (1971).

200) F. C. Frank and A. N. Stroh, "On the Theory of Kinking", Proc. Phys. Soc., **65**, 811 (1952).

201) A. N. Stroh, Proc. R. Soc. London A, **223**, 404 (1954).

202) H. Suematsu, T. Suzuki, T. Iseki, T. Mori, "Kinking and Cracking Caused by Slip in Single Crystals of SiC", J. Amer. Cer. Soc., **74**, 173-78 (1991)

203) S. Chakraborty, MSc. Thesis, Drexel University, June 1998.

204) E. Rudy, "Ternary Phase Equilibria in Transition Metal-B-C-Si Systems, Part V", Report No.AFML-TR-65-2, Air Force Materials Laboratory, Wright-Patterson AFB, Ohio, 1969.

205) S. Sarian, "Diffusion of C in TiC", J. Appl. Phys., **39**, 3305 (1968).

206) V. S. Eremov and A. S. Panov, Poroshk. Met. Akad. Nauk. SSR., **7**, 65 (1967).

207) B. Cockeram and R. Rapp, Met. Mater. Trans. A, **26A**, 777 (1995).

208) L. S. Hung, J. Gyulai, J. W. Mayer, S. S. Lau and M-A. Nicolet, J. Appl. Phys., **54**, 5076 (1980).

209) P. Revesz, J. Gyimesi , L. Pogany and G. Peto, J. Appl. Phys., **54**, 2114 (1983).